POLITECNICO DI MILANO

DEPARTMENT OF ENERGY

DOCTORAL PROGRAMME IN

ENERGY AND NUCLEAR SCIENCE AND TECHNOLOGY

CFD MODELING AND VALIDATION OF SPRAY EVOLUTION IN GASOLINE DIRECT INJECTION ENGINES

Doctoral Dissertation of:

Davide Paredi

Supervisor:

Prof. Tommaso Lucchini

Tutor:

Prof. Angelo Onorati

The Chair of the Doctoral Program:

Prof. Vincenzo Dossena

2020 - XXXII STEN Cycle

Dedicated to my parents

for their endless encouragement, support and love

Acknowledgements

I would first like to thank my supervisor Prof. Tommaso Lucchini and also Prof. Gianluca D'Errico for the guidance and the support they always put in my research activities.

I would like to express my sincere gratitude to my tutor Prof. Angelo Onorati who allowed me to work in the Internal Combustion Engine (ICE) Group and then believed in my capabilities by offering me the possibility to undertake a PhD programme.

I am also grateful to Prof. Christian Hasse for welcoming me in the Simulation of reactive Thermo-Fluid Systems group of the Technical University of Darmstadt and to Dr. Andrea Pati, both for the working collaboration and friendship developed during my period abroad in Germany.

Finally, a big thanks goes to the whole ICE Group, from the professors to all the colleagues who allowed me to enjoy these years dedicated to my PhD research activity.

Abstract

The present work focuses on the numerical characterization of the gasoline direct injection process performed in modern spark-ignition engines for vehicle applications. A detailed prediction of injection and air–fuel mixing is in fact a mandatory task to guarantee a stable and efficient combustion process with the aim to minimize pollutant formation. Within this context, computational fluid dynamics simulations represent a powerful tool to assess the main physical phenomena related to breakup and evaporation of the liquid jet, leading to mixture formation by means of the interaction between the vaporized fuel and the charge motion. To ensure the accuracy of the computed results, so that they could be a reliable support for industrial design and research activities, it is mandatory to validate the adopted multidimensional spray sub-models against available experimental data under well-defined operating conditions. To this end, the multi-hole gasoline direct injection Spray G injector made available by the Engine Combustion Network community was chosen as the reference geometry for the validation of the proposed numerical setup. Simulations were carried out with the open source OpenFOAM® software coupled with the LibICE framework which consists into a set of libraries and solvers developed by the Internal Combustion Engine Group of Politecnico di Milano and dedicated to the modeling of the most important physical phenomena related to internal combustion engines. In this work, at first a reference numerical spray setup was employed and tested under a wide range of Spray G operating conditions. By validating the results in terms of axial spray penetration, gas velocity, entrainment, spray morphology and Sauter Mean Diameter it was possible to observe strengths and weaknesses of the approach and thus propose specific improvements. An innovative liquid post-processing procedure, developed for the ECN6 Workshop and based on a projected liquid volume Eulerian field, represented the reference validation methodology for the proposed numerical improvements of atomization and secondary breakup which were implemented into the LibICE framework. More in detail, two solutions based on a decoupled approach for the management of primary and secondary atomization under a single spray model were proposed and validated in the present work. Furthermore, a literature-based evolution of a classic secondary breakup model was considered and implemented into the LibICE with the aim to provide a dynamic approach for droplet stripping and catastrophic breakup which could better suit the low-evaporating conditions of early injection events typical of modern gasoline

Abstract

direct injection engines. Two literature-based flash boiling evaporations models were implemented as well and validated on a dedicated Spray G flashing operating condition. The proposed numerical setups were also reproduced under dynamic conditions by performing simulations of a full-cycle of two modern gasoline direct injection optical access engines, one of which was directly coupled to the Spray G injector.

Finally, the physical phenomenon of collision between liquid drops during the injection process has been studied by implementing into the LibICE framework a literature model whose main purpose was to reduce the required computational time compared to other available mechanisms. The validation of the model was carried out by running different Spray G simulations and by comparing computed axial vapor penetration and droplet diameter with those calculated without collision and with other dedicated models already available in OpenFOAM®. On the basis of the observed results a further model modification was then proposed with the aim to achieve a better compromise between numerical accuracy and minimization of the required computational time.

Keywords Atomization, Breakup, CFD, Collision, ECN, Engine, Flash Boiling, Gasoline, GDI, NTC, Optical Access, Spray G

Sommario

Il presente lavoro si concentra sulla caratterizzazione numerica del processo di iniezione diretta di benzina tipico dei moderni motori ad accensione comandata per automobili. Una riproduzione dettagliata delle fasi di iniezione e miscelazione aria-combustibile è infatti un aspetto fondamentale per garantire un processo di combustione stabile, efficiente e con l'obiettivo di ridurre al minimo la formazione di inquinanti. In questo contesto, le simulazioni di termofluidodinamica computazionale rappresentano un potente strumento per valutare i principali fenomeni fisici correlati all'atomizzazione e all'evaporazione del getto di liquido che porta alla formazione della miscela mediante l'interazione tra il combustibile vaporizzato e i moti della carica aspirata. Per garantire l'accuratezza dei risultati numerici in modo che possano rappresentare un supporto affidabile per la progettazione industriale e le attività di ricerca, è fondamentale convalidare i sotto-modelli multidimensionali di spray con dati sperimentali disponibili in condizioni operative ben definite. A tal fine l'iniettore Spray G a iniezione diretta multi-foro di benzina, reso disponibile dall'associazione Engine Combustion Network, è stato scelto come geometria di riferimento per la convalida delle configurazioni numeriche proposte. Le simulazioni sono state condotte con il software open source OpenFOAM® accoppiato alla LibICE, la quale rappresenta un insieme di librerie e solutori sviluppato dall'Internal Combustion Engine Group del Politecnico di Milano e dedicato alla riproduzione numerica dei più importanti fenomeni fisici legati ai motori a combustione interna. In questo lavoro una configurazione numerica di riferimento è stata testata su un'ampia gamma di condizioni operative relative allo Spray G, verificando i risultati in termini di penetrazione assiale dello spray, velocità del gas, interazione liquido-gas, morfologia dello spray e Sauter Mean Diameter (diametro medio). In questo contesto è stato possibile osservare i punti di forza e di debolezza dell'approccio e quindi, su tale base, proporre miglioramenti specifici. Un'innovativa metodologia di analisi della fase liquida, svi-

Sommario

luppata per il Workshop ECN6 e basata su un campo Euleriano denominato "projected liquid volume", rappresenta l'approccio di validazione di riferimento utilizzato per valutare i miglioramenti ottenuti dai modelli di atomizzazione primaria e secondaria specificamente implementati nella LibICE nel corso del lavoro. Più in dettaglio, due soluzioni basate su un approccio disaccoppiato per la gestione di atomizzazione primaria e secondaria sotto un unico modello di spray sono state proposte e validate nel presente lavoro. Inoltre, un'evoluzione presente in letteratura di un classico modello di atomizzazione secondaria è stata implementata nella LibICE con l'obiettivo di fornire un approccio dinamico per breakup catastrofici e di stripping così che fosse possibile ottimizzare la riproduzione numerica dei processi di iniezione caratterizzati da condizioni di bassa evaporazione, tipici dei moderni motori a iniezione diretta di benzina. Sono stati inoltre implementati e validati su una specifica condizione operativa dello Spray G anche due modelli di evaporazione di tipo flash boiling disponibili in letteratura. I setup numerici proposti sono stati riprodotti anche in condizioni dinamiche eseguendo simulazioni di un ciclo completo di due moderni motori a iniezione diretta di benzina di tipo ad accesso ottico, uno dei quali direttamente accoppiato all'iniettore Spray G. Infine, il fenomeno fisico della collisione tra gocce liquide durante il processo di iniezione è stato studiato implementando nella LibiCE un modello di letteratura il cui scopo principale consiste in una riduzione del tempo di calcolo richiesto rispetto ad altri approcci disponibili. La convalida del modello è stata effettuata eseguendo diverse simulazioni Spray G e confrontando la penetrazione assiale di vapore e il diametro delle gocce calcolati con quelli resi disponibili senza collisione e da casi eseguiti adottando altri modelli di collisione già disponibili in OpenFOAM®. Sulla base dei risultati ottenuti è stata poi proposta una modifica al modello in modo da poter raggiungere un migliore compromesso tra accuratezza numerica e minimizzazione del tempo di calcolo richiesto.

Parole Chiave Accesso Ottico, Atomizzazione Primaria e Secondaria, Benzina, CFD, Collisione, ECN, Flash Boiling, GDI, Motore, NTC, Spray G

Contents

Acknowledgements I

Abstract III

Sommario V

List of Figures XI

List of Tables XIX

Nomenclature XXI

1 Introduction 1

1.1 An Overview on the State of the Art of Current Gasoline Direct Injection (GDI) Engines 1

1.2 Computational Fluid Dynamics (CFD) Applied to the Design of Internal Combustion Engines 5

1.3 Objective and Structure of the Thesis 7

2 Experimental Setup for Models Validation 9

2.1 The ECN Spray G Injector 9

2.1.1 Injector Geometry and Operating Points 10

2.1.2 Post-Processed Fields 15
2.2 The Optical Access IFPEN Engine 19
2.3 The Optical Access Darmstadt Engine 21

3 Fundamentals of the Numerical Methodology 25
3.1 The Numerical Framework 25
3.1.1 Transport Equations for the Gas Phase 26
3.1.2 Turbulence Modeling 28
3.1.3 Liquid Injection Modeling 30

4 Preliminary Numerical Spray G Investigation 37
4.1 The Numerical Framework 38
4.1.1 Primary Atomization 39
4.1.2 Secondary Breakup 40
4.2 Results 43
4.2.1 Baseline G1 Condition 43
4.2.2 Effects of Decreasing Ambient Temperature 47
4.2.3 Effects of Injection Pressure and Ambient Density 50
4.3 Conclusions and Next Steps 54

5 Improved Spray Numerical Setup: ECN6 Workshop and Engine Validation 57
5.1 The Adachi-Rutland Flash Boiling Evaporation Model 58
5.2 The ECN6 Workshop 61
5.2.1 The Numerical Framework 62
5.2.2 Numerical Results 64
5.3 IFPEN Optical Access GDI Engine Full-Cycle Simulations 83
5.3.1 The Numerical Framework 83
5.3.2 Results 87
5.4 Conclusions 102
5.4.1 ECN6 Workshop Simulations 102
5.4.2 IFPEN Optical Access Engine Simulations 103

6 Updated Prediction and Interaction of Atomization and Secondary Breakup Phenomena **105**

6.1 Numerical Atomization by Means of the Pilch-Erdman Mechanism: Spray G1 Vessel Results . . . 106

6.2 Numerical Atomization by Means of a Decoupled KH Approach . . . 110

6.2.1 Spray G3 Vessel Results . . . 111

6.2.2 Darmstadt Engine Results . . . 119

6.3 The Adachi-Price Flash Boiling Evaporation Model . . . 124

6.4 Implementation of the Nagaoka-Kawamura Dynamic KHRT Secondary Breakup Model . . . 125

6.4.1 Spray G Vessel Results . . . 128

6.5 Conclusions . . . 135

7 Implementation of the NTC Collision Model into the LibICE Framework **139**

7.1 The NTC Collision Model . . . 144

7.2 Validation of the NTC Model on the Spray G1 Operating Point . . . 146

7.3 A Modified Version of the NTC Collision Model . . . 148

7.4 Conclusions . . . 155

8 Conclusions **157**

8.1 Atomization and Secondary Breakup Modeling for GDI Sprays . . . 158

8.2 Droplets Collision Modeling . . . 162

8.3 Future Works . . . 164

Bibliography **165**

Appendices **173**

A ECN Spray G1 Operating Point, Effects Of Turbulence Modeling on Computed Results **175**

List of Figures

2.1 Spray G injector geometry [4, 78, 105] 10
2.2 Scaled mass flow rate profiles [78] 14
2.3 Schematic of the Spray G injector configuration [4, 78] 15
2.4 Numerical methodology for the definition of the PLV Eulerian field [55,79] 16
2.5 Experimental profile of the centerline velocity [107] 18
2.6 Schematics of the IFPEN engine top mounted GDI injector 20
2.7 Schematics of the three tested IFPEN engine intake ports configurations 20
2.8 Geometrical details of the IFPEN GDI engine 21
2.9 Darmstadt engine, "wall-guided" (top) and "spray-guided" (bottom) configurations [8] 22
2.10 Schematics of the Darmstadt engine test bench [8] 23

3.1 Main physical phenomena related to the spray evolution [19] 34

4.1 Reitz-Diwakar breakup model [49] 41
4.2 Case 1, computed liquid and vapor penetrations [76] 44
4.3 Case 1, computed axial velocity at 15 mm from the injector nozzle [76] 45
4.4 Spray morphology validation, 160 μs [76] 46
4.5 Spray morphology validation, 560 μs [76] 47

4.6 Spray morphology validation, 1040 μs [76] 47
4.7 Computed spray penetration, Case 4 (Reitz-KHRT) against Case 5 (Retiz-Diwakar) [76] 48
4.8 Spray penetrations, Case 5, Case 6 and Case 7 [76] 49
4.9 Spray penetrations, Case 8 and Case 9 [76] 50
4.10 Spray penetrations, Case 10, Case 11 and Case 12 [76] 52
4.11 Spray morphology validation, 160 μs [76] 53
4.12 Spray morphology validation, 560 μs [76] 53
4.13 Spray morphology validation, 1040 μs [76] 53
4.14 SMD validation [33, 76] 54

5.1 G1 condition, comparison between Sandia and UoM axial liquid penetrations, low and high thresholds [79] 65
5.2 G1 condition, axial liquid penetration, computed results against UoM experimental data, low and high thresholds [79] 66
5.3 G1 condition, axial liquid penetration, computed results against Sandia experimental data, low and high thresholds [79] 67
5.4 G1 condition, axial vapor penetration, effects of the round-jet correction on the numerical results [79] 68
5.5 G1 condition, centerline gas velocity profile, effects of the round-jet correction on the numerical results [79] 68
5.6 G1 condition, PLV maps comparison between UoM experimental results and computed spray. Range is $0 - 0.01\frac{mm^3}{mm^2}$ [79] 70
5.7 G1 condition, axial PLV profiles, comparison between UoM experimental results and computed spray [79] 71
5.8 Coordinates for PDI data sampling [25, 79] 72
5.9 G1 condition, radial PDI velocity profiles, comparison between GM experimental results and computed data [79] 73
5.10 G1 condition, radial PDI SMD profiles, comparison between GM experimental results and computed data [79] 74

5.11 G1 condition, validation of radial distribution of fuel mass over volume at 0.6 ms and 2 mm axially downstream of the injector nozzle. Experimental data from ANL by means of x-ray investigation [79] 75

5.12 G2 condition, axial liquid penetration, comparison between computed results and experimental data from UoM for both thresholds [79] 75

5.13 G2 condition, axial vapor penetration, UoM experimental data against computed results [79] 76

5.14 G2 condition, PLV maps, comparison between UoM experimental results and computed spray. Range is $0 - 0.01\frac{mm^3}{mm^2}$ [79] 77

5.15 G2 condition, axial PLV profiles, comparison between UoM experimental results and computed spray [79] 77

5.16 G3 condition, axial liquid penetration, comparison between computed results and experimental data from UoM for both thresholds [79] 78

5.17 G3 condition, axial vapor penetration, UoM experimental data against computed results [79] 79

5.18 G3 condition, PLV maps, comparison between UoM experimental results and computed spray. Range is $0 - 0.01\frac{mm^3}{mm^2}$ [79] 79

5.19 G3 condition, axial PLV profiles, comparison between UoM experimental results and computed spray [79] 80

5.20 G4 condition, axial liquid and vapor penetrations, comparison between computed results and experimental data from Sandia (low threshold) [79] 81

5.21 G7 condition, axial vapor penetration, Sandia experimental data against computed results [79] 82

5.22 PLV maps, comparison between computed G1 (left) and computed G7 (right) sprays. Range is $0 - 0.01\frac{mm^3}{mm^2}$ [79] 82

5.23 Full-cycle mesh generation procedure 84

5.24 Schematics representation of film modeling [54] 85

5.25 Schematics representation of possible film separation [54] 86

5.26 High-tumble, SOI 460 CA condition, liquid valve impingement and film stripping 87

5.27 IFPEN engine, comparison of the computed velocity magnitude at the maximum intake valve lift 88
5.28 SOI 460, early injection times 89
5.29 SOI 460, full injection times 90
5.30 SOI 460, post EOI 91
5.31 Wall film, impinged fuel mass on the piston surface, SOI 460 CA, 700 CA 91
5.32 Homogeneity Index (HI), SOI 460 CA, "swumble" and "high-tumble" configurations 92
5.33 SOI 460, λ distribution, 700 CA 92
5.34 3D in-cylinder λ field distribution at 700 CA, SOI 460 CA, "swumble" case (left) and "high-tumble" case (right) 93
5.35 Computed TR trends, SOI 460 CA 94
5.36 Effects of delayed SOI on mixture distribution, "high-tumble" configuration, SOI 540 CA (left) against SOI 460 CA (right) 95
5.37 SOI 540, early injection times 95
5.38 SOI 540, full injection times 96
5.39 SOI 540, post EOI 96
5.40 Wall film, impinged fuel mass on the piston surface, SOI 540 CA, 700 CA 97
5.41 Homogeneity Index (HI), SOI 540 CA, "swumble" and "standard tumble" configurations 97
5.42 SOI 540, λ distribution, 700 CA 98
5.43 3D in-cylinder λ field distribution at 700 CA, SOI 540 CA, "swumble" case (left) and "standard tumble" case (right) 98
5.44 Computed TR trends, SOI 540 CA 99
5.45 GDI combustion and soot modeling methodology for GDI engines [57] 100
5.46 Interaction between flame propagation and charge motion at different times, SOI 460 CA, "swumble" (left) and "high-tumble" (right) cases . 101
5.47 Validation against experimental data of computed cylinder pressure and apparent HRR, SOI 460 CA 101
5.48 Validation against experimental data of computed cylinder pressure and apparent HRR, SOI 540 CA, "high-tumble" case 102

6.1 Primary atomization, Pilch-Erdman (left) and KH (right). Parcels colored on diameter size (maximum 0.165 mm, minimum 1e-5 mm) [77] . 109
6.2 Validation of computed axial spray penetrations and centerline velocity [77] 110
6.3 Axial PLV profiles, comparison between UoM experimental results and computed spray [77] 111
6.4 PLV maps, comparison between UoM experimental results (on the left) and computed spray (on the right). Range is $0 - 0.01\frac{mm^3}{mm^2}$ [77] 112
6.5 Radial PDI for liquid droplets velocity, experiments against simulation [77] 112
6.6 Radial PDI for the SMD, experiments against simulation [77] 113
6.7 G3 simulation, KH atomization approach, 0.1 ms, detail of the spray evolution during the primary breakup phase 113
6.8 G3 simulation, PE atomization approach, 0.1 ms, detail of the spray evolution during the primary breakup phase 114
6.9 G3 vessel simulation, comparison between experimental and numerical axial vapor penetration [83] 115
6.10 G3 vessel simulation, comparison between experimental and numerical axial liquid penetration [83] 116
6.11 G3 vessel simulation, axial PLV profiles, comparison between experimental and computed data [83] 117
6.12 G3 vessel simulation, radial PLV profiles, comparison between experimental and computed data [83] 118
6.13 G3 vessel simulation, comparison between experimental and numerical spray morphologies based on PLV maps. Range is $0 - 0.01\frac{mm^3}{mm^2}$, axes dimensions in mm [83] 118
6.14 Comparison between experimental and numerical cylinder pressure of the Darmstadt engine for the operating point A [83] 119
6.15 Comparison between computed and experimental horizontal velocity profiles, on the tumble plane for the Darmstadt engine, under the operating point A, at $90°aTDC$ [83] 120

6.16 Comparison between computed and experimental vertical velocity profiles, on the tumble plane for the Darmstadt engine, under the operating point A, at $90°aTDC$ [83] 121
6.17 Overview of the interaction between liquid spray and intake flow [83] . 121
6.18 Influence of each operating condition on the air-fuel equivalence ratio distribution in the engine at $20°bTDC$ [83] 123
6.19 Schematic of heat-transfer at droplet temperatures above and below the boiling temperature of the fuel [92] 124
6.20 Droplet total breakup time, correlation of Pilch-Erdman (solid line) against Nagaoka-Kawamura model (symbol) [70] 126
6.21 G1 condition, validation of computed axial spray penetrations and centerline velocity 129
6.22 G1 condition, PLV maps, comparison between experimental results and computed spray. Range is $0 - 0.01\frac{mm^3}{mm^2}$, axes dimensions reported in mm 130
6.23 G7 condition, comparison between computed and experimental axial vapor penetrations 130
6.24 PLV maps, comparison between computed G1 (left) and computed G7 (right) results. Range is $0 - 0.01\frac{mm^3}{mm^2}$, axes dimensions reported in mm 131
6.25 G2 condition, comparison between computed and experimental axial vapor penetrations 131
6.26 G2 condition, axial PLV profiles, comparison between experimental results and computed spray 132
6.27 G2 condition, PLV maps, comparison between experimental results and computed spray. Range is $0 - 0.01\frac{mm^3}{mm^2}$, axes dimensions reported in mm 133
6.28 G3 condition, comparison between computed and experimental axial spray penetrations 133
6.29 G3 condition, axial PLV profiles, comparison between experimental results and computed spray 134
6.30 G3 condition, PLV maps, comparison between experimental results and computed spray. Range is $0 - 0.01\frac{mm^3}{mm^2}$, axes dimensions reported in mm 135

7.1 Schematics of possible droplet collision regimes [19] 140

7.2 Illustration of the impact parameter *X* definition [19] 141
7.3 G1 condition, radial PDI for liquid droplet velocity, experiments against simulations without collision and with the Nordin model 142
7.4 G1 condition, validation of the computed axial vapor penetration profiles 147
7.5 G1 condition, validation of the modified NTC model based on the axial vapor penetration 149
7.6 G1 condition, validation of the modified NTC model based on the computed SMD 150
7.7 G3 condition, validation of the modified NTC model based on the axial vapor penetration 151
7.8 G3 condition, validation of the modified NTC model based on the computed SMD 152
7.9 G3 condition, computed PLV-based spray morphologies at 0.3 ms, standard G3 case (left), Nordin collision simulation (center) and modified NTC calculation (right). Range is $0 - 0.01\frac{mm^3}{mm^2}$, axes dimensions reported in mm 152
7.10 G3 condition, 0.3 ms, axial PLV profiles comparison between experiments and simulations 153
7.11 G3 condition, computed PLV-based spray morphologies at 0.6 ms, standard G3 case (left), Nordin collision simulation (center) and modified NTC calculation (right). Range is $0 - 0.01\frac{mm^3}{mm^2}$, axes dimensions reported in mm 154
7.12 G3 condition, 0.6 ms, axial PLV profiles comparison between experiments and simulations 154

A.1 G1 simulations, effects of the adopted turbulence models on computed axial vapor penetration and centerline velocity 176
A.2 Comparison of computed Lagrangian spray morphologies coloured by the liquid velocity magnitude, 0.3 ms 177
A.3 Comparison of computed Lagrangian spray morphologies coloured by the liquid velocity magnitude, 0.6 ms 177

A.4 Comparison of computed Lagrangian spray morphologies coloured by the liquid velocity magnitude, 0.9 ms 177

List of Tables

2.1 Spray G injector characteristics [78] 11
2.2 Spray G baseline operating condition 11
2.3 ECN reference cases: ambient properties 12
2.4 Bespoke simulated cases, operating properties 13
2.5 Scaled values of injected fuel mass 13
2.6 IFPEN optical access engine specifications 19
2.7 IFPEN GDI injector specifications 19
2.8 Main engine geometric parameters [83] 22
2.9 Valve timing [83] 22
2.10 Operating conditions [83] 23

4.1 Numerical framework 38
4.2 Main Huh-Gosman model constants 44
4.3 Numerical details of cases 1, 2 and 3 44
4.4 Bespoke simulated cases: operating properties 47
4.5 Bespoke simulated cases: operating properties 50
4.6 Main adopted Reitz-Diwakar model constants 52

5.1 Numerical framework 62

5.2 Huh-Gosman model constants 63
5.3 Reitz-KHRT model constants 63
5.4 Simulated Spray G operating conditions 65
5.5 Impact of model parameters on achieved results (+) and on possible improvements (-) 104

6.1 Spray model main parameters 108
6.2 G3 condition, spray model main parameters 111
6.3 Low-density (G2, G3) spray model main parameters 128
6.4 High-density (G1, G7) spray model main parameters 128

7.1 Spray G1, required computational times 146
7.2 Spray G3 condition, required computational times 153

A.1 Adopted numerical spray setup 176

Nomenclature

Abbreviations and Acronyms

$aTDC$	After Top Dead Center
AMR	Adaptive Mesh Refinement
ANL	Argonne National Laboratories
$bTDC$	Before Top Dead Center
B	Collision Dimensionless Impact Parameter
$BSFC$	Brake Specific Fuel Consumption
BTE	Brake Thermal Efficiency
$\frac{B}{S}$	Bore-Ratio
CA	Crank Angle
CFD	Computational Fluid Dynamics
CO_2	Carbon Dioxide
CNR	Consiglio Nazionale delle Ricerche
CR	Compression Ratio
DBI	Diffused Back-Illumination
DNS	Direct Numerical Simulation
DWI	Direct Water Injection

ECN	Engine Combustion Network
EGR	Exhaust Gas Recirculation
EOI	End Of Injection
EVC	Exhaust Valve Closing
EVO	Exhaust Valve Opening
GDI	Gasoline Direct Injection
GM	General Motors
GPF	Gasoline Particulate Filter
HCs	Hydrocarbons
HI	Homogeneity Index
HRR	Heat Release Rate
KH	Kelvin-Helmholtz
$KHRT$	Kelvin-Helmholtz Rayleigh-Taylor
ICE	Internal Combustion Engine
$IFPEN$	IFP Energies Nouvelles
IM	Istituto Motori
$IMEP$	Intake Mean Effective Pressure
$IRES$	Infrared Extinction/Scattering
IVC	Intake Valve Closing
IVO	Intake Valve Opening
La	Laplace Number
LES	Large Eddy Simulation
$LIVC$	Late Intake Valve Closing
LVF	Liquid Volume Fraction
$NIST$	National Institute of Standards and Technology
NO_x	Nitrogen Oxides
N_2O	Nitrous Oxide
NTC	No-Time-Counter
Nu	Nusselt Number
PCA	Plume Cone Angle
PDI	Phase Doppler Interferometry

PE	Pilch-Erdman
PFI	Port Fuel Injection
$PISO$	Pressure Implicit with Splitting of Operator
PIV	Particle Image Velocimetry
PLV	Projected Liquid Volume
PM	Particulate Matter
PN	Particulate Number
PWI	Port Water Injection
rpm	Revolutions Per Minute
$RANS$	Reynolds-Averaged Navier Stokes
RDE	Real Driving Conditions
Re	Reynolds Number
RMS	Root-Mean Square
RNG	Re-Normalisation Group
RT	Rayleigh-Taylor
SCR	Selective Catalytic Reduction
Sh	Sherwood Number
SI	Spark Ignition
SMD	Sauter Mean Diameter
SOI	Start Of Injection
SST	Shear Stress Transport
TR	Tumble Ratio
UoM	University of Melbourne
VOF	Volume Of Fluid
VVT	Variable Valve Timing
We	Weber Number

Greek Symbols

α	Spray Angle; Heat Transfer Coefficient

β	Mass Diffusion Coefficient
Γ	Diffusion Coefficient
ε	Turbulent Dissipation Rate
θ	Angle
λ	Breakup Wavelength
μ	Dynamic Viscosity
ϕ	Generic Conservation Equation Variable
ρ	Density
σ	Surface Tension; Standard Deviation of Fuel Mass Fraction; Drops Collision Cross Section
τ	Optical Thickness; Viscous Stress; Characteristic Time
τ_b	Breakup Time
τ_e	Evaporation Transfer Relaxation Time
τ_h	Heat Transfer Relaxation Time
τ_u	Momentum Relaxation Time
χ	Superheat Degree Parameter
ω	Chemical Reactions Source Term; Angular Engine Speed
Ω	Most Unstable Grow Rate

Latin Symbols

a	Spheroidal Radius
A	Area; Surface; Air Mass
c_d	Discharge Coefficient
c_p	Specific Heat
c_v	Velocity Coefficient
C	Extinction Cross-Section Parameter; General Model Coefficient
$C_{1\varepsilon}$	Standard k-ε Tubulence Model Constant
C_{b1}	Reitz-Diwakar Model Constant
C_{b2}	Reitz-Diwakar Model Constant
C_D	Drag Coefficient

C_{s1}	Reitz-Diwakar Model Constant
C_{s2}	Reitz-Diwakar Model Constant
d	Parcel Diameter
D	Droplet Diameter
D_i	Binary Diffusive Coefficient
f	Mass Transfer Factor
F	Fuel Mass
$\mathbf{F}$	Drag Rate of Momentum Gain/Loss
g	Gravity
G	Vaporization Rate
h	Enthalpy; Thickness
h_v	Droplet Heat of Vaporization
k	Turbulent Kinetic Energy; Thermal Conductivity
L	Characteristic Length; Latent Heat
m	Mass
M	Evaporation Term
M_{coll}	Collision Probability
N	Statistical Number of Droplets
p	Pressure
q	Number of Droplets in a Parcel
Q	Enthalpy Source Term
r	Droplet/Parcel Radius
S	Generic Source Term; Surface
t	Time
T	Temperature
U	Velocity
V	Volume
X	Collision Impact Parameter
y	Integration Direction
Y	Mass Fraction
Y_{ttf}	AMR Volumetric Scalar Field

Subscripts and Superscripts

$*$	Dimensionless
$\dot{}$	Source Term
$\vec{}$	Vector
∞	Far-Field
a	Atomization
amb	Ambient
atm	Atmospheric
b	Saturated
$boiling$	Flash Boiling Condition
$Bern$	Bernoulli
c	Chemical Reactions; Core Length
$coll$	Collision
$crit$	Stable Value
d	Droplet
dyn	Dynamic
ext	Extinction
f	Flashing
F	Film
$fuel$	Fuel
fs	Free Surface
g	Gas
σ	Capillary
h	Hydrostatic
KH	Kelvin-Helmholtz
i	i^th Component; X Direction
inj	Injection
j	Y Direction

l	Liquid
$mean$	Average
n	Normal to Surface
n, h	Completely Inhomogeneous
new	End of the Time-Step
old	Beginning of the Time-Step
p	Parcel
PE	Pilch-Erdman
rel	Liquid-Gas Relative
RT	Rayleigh-Taylor
s	Saturation Conditions
sc	Subcooled Conditions
sh	Superheated Conditions
$strip$	Stripped
S	Source Term
$Stoich$	Stoichiometric Conditions
t	Total
$turb$	Turbulent
v	Vapor
w	Aerodynamic; Wall
0	Initial Value; Value at Drop Surface

CHAPTER 1

Introduction

1.1 An Overview on the State of the Art of Current Gasoline Direct Injection (GDI) Engines

Four-stroke, Otto cycle Internal Combustion Engines (ICE) still represent to this day the most relevant form of propulsion worldwide and are currently subjected to considerably stringent regulations in terms of CO_2 and pollutant formations. In fact, as road transport is held responsible for about 15.9% of the overall CO_2 emissions a great technical effort is being requested to all manufacturers to meet the upcoming regulations which will require a fleet average of 95 grams of CO_2 per kilometer to all new cars [43,124] in Europe by 2021, fact which translates to an average fuel consumption of $4.1L/100km$ for gasoline engines. Moreover, by 2025 and 2030 targets will be set to values respectively lower of 15% and 37.5% compared to 2021 standards [10,43]. HC, NO_x and PM emissions [17, 60] are continuously subjected to stricter controls as well, with Euro-6d TEMP regulations now based on real life driving conditions (RDE) and upcoming 2025

Tier3 standards in the United States [103]. Discussions on the upcoming Euro-7 standard are also being held with the intention to globally extend the emissions controls on previously non-regulated species (aldheydes, ammonia, isocyanic acid, N_2O) and to measure sub-23 nm particulate matter (PM) [43, 62].

Within this context, the current reference technology in terms of thermal efficiency and reduced emissions is represented by gasoline direct injection (GDI) engines. Such an approach was introduced in the market for the gasoline engines of passenger cars in the second half of the 1990s [44, 71] and consists into the injection of the fuel directly into the cylinder. This methodology differs from the more traditional port-fuel (PFI) system which is characterized by the injection process taking place before the intake valves and inside the intake port. The great advantage of the GDI technology consists into the possibility to adopt different operating conditions ranging from a stratified mode under partial loads to a homogeneous charge under full loads [34]. The stratification of the charge is achieved by performing the fuel injection event during the compression phase, fact which leads to a stable combustion with an overall very lean in-cylinder mixture. As a consequence pumping and heat losses are reduced and fuel consumption is improved [46]. At the same time, ensuring a homogeneous mixture at higher loads thanks to a GDI injection process carried out during the intake phase allows for an overall improved engine efficiency compared to what it would be possible to achieve with a traditional port-fuel approach. In fact, by directly injecting the fuel into the cylinder its evaporation leads to a phenomenon of charge cooling thus riducing knock and improving the volumetric efficiency [46].

To this day, GDI technology allowed the manufacturers to effectively face the different emission regulations, however it appears clear that a further technical step is needed to design more efficient gasoline engines. Within this context, the aim is to shift their actual operating points in zones of the engine performance map [40] characterized by greater efficiency. The current research on GDI engines is thus focused on possible solutions ranging from technical methodologies to the adoption of potentially "green" fuels. Engine downsizing coupled with turbo-charging is today one of the most adopted approaches with recent studies [124] which have shown that a maximum effective efficiency of 36.5% can be achieved for current light-duty GDI engines coupled

with variable valve timing (VVT). Even higher values of thermal efficiency are tageted by increasing the compression ratio (CR) thus leading to a reduced fuel consumption at the potential cost of a higher knock tendency [104]. To prevent this phenomenon to happen, the spark timing could be retarded at the cost of reduced power output and overall fuel economy. Recent evolutions demonstrated a preference for the adoption of an exhaust gas recirculation (EGR) system, much like it has been done in modern diesel engines [45]. In fact, studies carried out on modern turbocharged gasoline engines [112] demonstrated that among the possible EGR loops (low pressure, mixed pressure and high pressure) the low pressure one can have the greatest impact on fuel consumption reducing it by up to 5%. It was demonstrated that an increase of CR coupled with the use of EGR could increase the brake thermal efficiency (BTE) of a current GDI engine up to 3.5% with an EGR of 25% [111]. Other studies reported that under a combination of increased CR and adoption of cooled EGR the BSFC of a GDI engine could be reduced up to by 12% at high load and 5% at low load [50]. Despite this combination of factors being important in the path towards emissions reduction EGR was hown to reduce overall engine performance at high loads. Within this context, port water injection (PWI) was considered as a method to provide high load performances while also reducing knock thanks to the high heat due to water vaporization [23]. Moreover, direct water injection (DWI) was also studied as an effective method to enhance the overall engine BTE. Recent literature references have demonstrated that DWI leads to better efficiency while requiring less water compared to PWI with a global reference value of almost 40% reached under 17 bar IMEP [24]. Finally, with respect to all the possible technical interventions in the context of an optimal compromise between reduced knock tendency and high BTE for GDI engines, effects due to the bore to stroke ratio (B/S) were as well investigated in literature [73].

Another intrinsic characteristic of GDI engines consists into the fact that compared to more conventional PFI units they tend to have a higher emission of PM [109]. This is mainly due to the GDI in-cylinder mixture which forms on average under lower mixing times and less homogeneous conditions compared to traditional PFI engines. Within this context, the injected liquid fuel has less time to completely evaporate with thus a higher probability of wall impingement. Extending the comparison to in-cylinder

diesel injectors, besides the lower liquid evaporating conditions typical of a GDI engine wall impingement can also be promoted by narrower spray angle values (from 60° to 90° compared to the 140°-160° range of diesel units [80]). The impinged spots, being particularly richer in fuel, become a relevant source of soot formation during the combustion phase [27, 123]. A recent investigation based on a wide literature database [26] evaluated different technical solutions which could lead to the reduction of PM and particulate number (PN) emissions from GDI engines. Among the most efficient methodologies proposed in the review there are:

- the optimization of the spray pattern with increased injection pressures (up to 200 bar for second generation GDI engines) and minimization of wall wetting phenomena;
- the potential further increment of the injection pressure up to 400 bar with asymmetric spray jets. Mie-scattering experimental investigations carried out on multihole GDI injectors with operating pressures of 400 bar and 700 bar [68] showed that the spray penetration lengths differ slightly between those two conditions. This fact confirms that a high injection pressure allows to finely atomize the liquid droplets thus potentially helping in preventing wall impingement;
- the in-cylinder injector mounting postition, with top mounted injectors that seem to have lower PM and PN emissions compared to side mounted ones. As this is still a quest open to discussion according to most manufacturers, it was proven that both solutions are subjected to the phenomenon of injector tip wetting [14, 38] which represents as well a considerable potential source of soot formation;
- the combination of both PFI and GDI systems, which have shown an optimum compromise between particulate emissions, fuel economy and engine drivability;
- the adoption of gasoline particulate filters (GPF).

Finally, another important path towards the emissions reduction of internal combustion engines could be represented by the adoption of the so-called liquid biofuels which hold great potential in increasing SI engines BTE while having higher energy density compared to other possible gaseous alternatives [48]. Within this context, a

challenge in their utilization could be related to their intrinsically higher oxygen content compared to the standard gasoline leading to a lower energy density and thus tu an increased fuel consumption [86]. Still, this phenomenon could be mitigated by an accurate coupling between the utilization of renewable fuels and the adoption of the different set of technical solutions [48] previously described in this section.

1.2 Computational Fluid Dynamics (CFD) Applied to the Design of Internal Combustion Engines

To this day, given the available computational power which is constantly increasing Computational Fluid Dynamics (CFD) simulations are becoming more and more a mandatory tool for the support of experimental investigations in the context of thermo-fluid dynamics research activities. Despite the rise of electrification internal combustion engines will still represent a fundamental propulsion system in the automotive field for the upcoming decades [60]. Of course, to ensure continuous efficiency improvements and reduction of fuel consumption and emissions dedicated research must not be stopped. Within this complex context where every small technical detail or parameter can make a difference, CFD represents an invaluable instrument. Recent investigations on the state of the art of the research applied to internal combustion engines [60] demonstrate how CFD is intrinsically adopted in every field, going from injection, air-fuel mixing and combustion prediction to after treatment solutions. Moreover, experimental research evolves along with CFD as well providing a basis for further model development and optimization. As an example, new scattering absorption techniques [61] were recently developed to provide a more accurate measurement of the spray Sauter Mean Diameter (SMD) for a better support to CFD calibration activities. The spray collapse of GDI, multi-hole sprays heavily influences the mixture formation process and recent studies [93] were aimed at a better understanding of the phenomenon by means of CFD simulations investigating physical effects due to hole geometry, ambient pressure and injector operating conditions. CFD is also well exploited as a tool in co-operations between industrial and research/academic organizations, with state of the art activities which recently focused on experimental and numerical evaluation of the impact of multiple fuel injectors on the control of the combustion process with the aim to improve the

overall engine brake thermal efficiency [116, 117]. Moreover, conjugate heat transfer so that heat losses at the engine walls could be evaluated is a topic recently investigated as well by means of a combination between CFD and one-dimensional (1D) simulations [91]. CFD calculations are also employed for modeling the fluid-dynamics and heat transfer process in exchangers dedicated to oil cooling in internal combustustion engines [115], while 1D-CFD couplings have recently been applied in the context of after treatment Selective Catalytic Reduction (SCR) for the optimization of the NO_x reduction process in Diesel engines [114].

Among all the different fields which were discussed the investigation on the physical phenomena characterizing the fuel injection process represents one of the most fundamental paths towards emissions reduction and the main task of the proposed numerical work applied to GDI engines. In fact, liquid breakup, evaporation rate and interaction between intake charge and injected fuel greatly influence combustion efficiency and thus the engine power output both in terms of fuel consumption and pollutant formation. To promote research activities on this fundamental topic, multi-hole GDI injector geometries were made available during the years both for experimental and numerical investigations. Among them, the eight-hole, Delphi-manufactured Engine Combustion Network (ECN) Spray G [4] injector represents one of the most experimentally validated geometries in literature [5, 80, 85, 107] and it was thus selected as the reference benchmark for the CFD research carried out in this thesis. Within this context, the Spray G injector was subjected during the years to a wide set of numerical simulations focused on the in-nozzle jet analysis [99, 100], the evaluation of effects due to the counterbore on the interaction between liquid and vapor fuel [69] and on the near-field spray to consider transient needle motion [16]. Furthermore, the primary atomization phase nearby the injector tip was investigated by means of accurate direct numerical simulations (DNS) [21]. These analysis also proved to be fundamental to comprehend the behavior of the far-field spray as the internal injector flow is intrinsically transient and it thus holds great influence on the actual spray angle at the nozzle. The understanding of the internal flow phenomena is mandatory to provide physical weight to the numerical sub-models which are dedicated to the reproduction of the most relevant parameters related to the injector nozzle. Still, the characteristic times of an Eulerian in-nozzle

simulation are too small to allow for an accurate prediction of the turbulent and physical characteristic scales. This fact makes usually difficult to couple such a methodology to the modeling of the far-field spray and of the subsequent in-cylinder air-fuel mixture formation. Within this context, albeit so-called "one way coupling" approaches were proposed in literature [99], the modeling of the far-field spray by means of dispersed Lagrangian parcels into an Eulerian medium still represents the most feasible approach especially when GDI injection computations are coupled with the simulation of the complete engine cycle.

In literature the Spray G injector was benchmarked with numerical realizations based on both large eddy simulations (LES) and Reynolds-Averaged Navier-Stokes (RANS) approaches. It was observed that the interaction between the liquid plumes and the surrounding gas is a sensitive quantity to be predicted with both the LES and RANS approaches underestimating the negative centerline axial gas velocity before the end of injection (EOI) and showing considerable influence from the spray plume cone angle [105].

1.3 Objective and Structure of the Thesis

Within this context the objective of this thesis is to provide a comprehensive numerical characterization of multi-hole sprays for modern GDI engines applications. The main focus is put on the investigation of the Engine Combustion Network Spray G injector that represents a complex eight-holes geometry for which a wide set of experimental data are available under a range of operating conditions thus taking into account real engine early injection, late injection and flash boiling vaporization events. Moreover, after an in-vessel validation of the spray setup full-cycle engine simulations coupled with direct injection processes were carried out as well on modern GDI optical access engines such as the IFP Energies Nouvelles and the Darmstadt units. Within this context a set of atomization, secondary breakup, evaporation and droplet collision numerical models is proposed, tested, validated and implemented into the OpenFOAM®-LibICE framework. The simulation activity is in fact completely carried out with the open-source, 3D finite volume OpenFOAM® software coupled with the dedicated *LibICE* engine-simulation library which has been developed and validated during the years by

the Internal Combustion Engine Group of Politecnico di Milano. The numerical campaign is mainly based on a Lagrangian description of the dispersed phase representing the liquid spray, coupled with a finite volume Eulerian approach for the gaseous phase. An Unsteady Reynolds Averaged Navier Stokes (URANS) turbulence approach was adopted for all the calculations.

Overall, the proposed work can be summarized in four main key points:

- evaluation of strengths and weaknesses of a current baseline, state of the art numerical setup of the Spray G injector thanks to at-the-time available experimental data;
- discussion on dedicated atomization, secondary breakup and flash boiling evaporation models which could improve the accuracy of the original numerical results in terms of computed axial vapor penetration, axial liquid penetration, Sauter Mean Diameter (SMD), mixture formation, entrainment and liquid spray morphology. Moreover, for a more detailed in-vessel validation of these models an innovative projected liquid volume (PLV)-based post-processing procedure was employed thanks to bespoke experimental contributions specifically provided for the Spray G at the ECN6 Gasoline Workshop by different valuable research institutions;
- execution of multiple operating points full-cycle simulations with the aim to further validate each comprehensive numerical setup on IFP and Darmstadt state of the art, optical access GDI engines coupled with the Spray G injector. The influence of the computed spray on fundamental physical phenomena such as mixture formation, wall impingement, liquid film formation and combustion efficiency was investigated;
- dedicated implementation into the LibICE framework of the literature NTC droplet collision model. Validation in terms of main physical spray parameters and required computational time against other available numerical collision mechanisms on multiple in-vessel Spray G operating conditions. Proposition of a modified version of the original NTC approach so that an optimum compromise between required computational resources and computed spray accuracy could be achieved.

CHAPTER 2

Experimental Setup for Models Validation

In this chapter of the thesis the experimental equipments which were fundamental for the validation of the proposed numerical models are introduced and described in detail. Within this context, the first section is dedicated to the ECN Spray G injector which represents the reference geometry for all of the activities carried out in this work. Afterwards, the main geometrical and operating characteristics of the IFP Energies Nouvelles (IFPEN) [7] and Darmstadt optical access GDI engines are reported.

2.1 The ECN Spray G Injector

The specifications of the Spray G injector are here described along with the introduction of the most relevant operating conditions and experimental contributions. Subsequently an analysis of the reference post-processing procedure will be provided with the introduction of the most important spray-related physical quantities which will stand at the basis of the numerical validation.

2.1.1 Injector Geometry and Operating Points

The purpose of the research activity performed on the Spray G geometry is to reproduce the injection phase during an engine-like compression stroke with a non-reacting mixture condition. As it is shown in Fig.2.1(a), the Spray G is characterized by a 8-hole configuration. Main geometric parameters such as the *drill angle* and the *plume cone angle* (PCA) are displayed in Fig.2.1(b) while nozzle specifications are reported in Tab.2.1. With reference to the injector axis the drill angle is reported in literature to be equal to 37° [105].

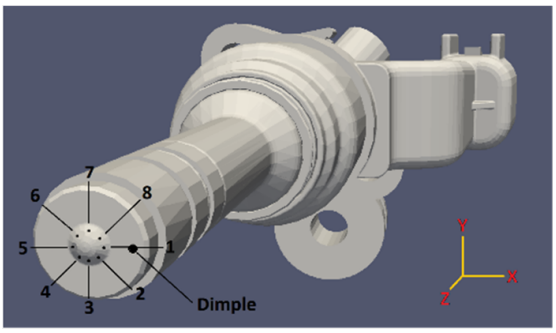

(a) Spray G injector

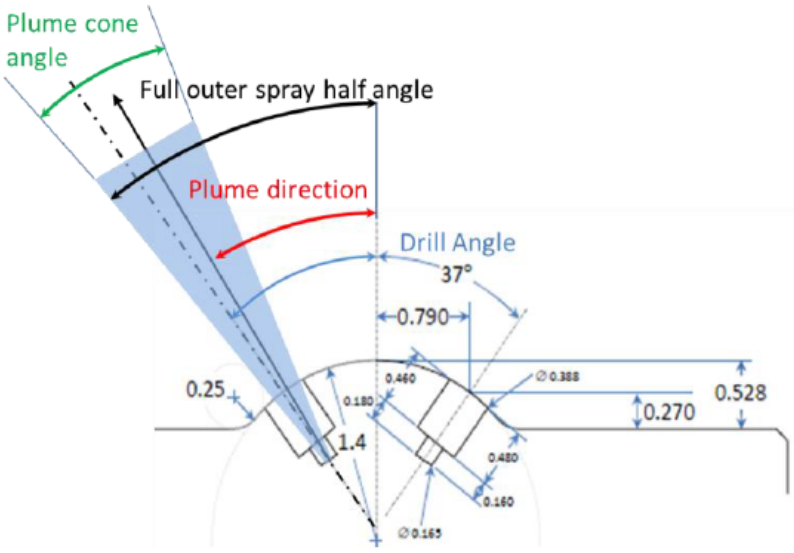

(b) Main geometric specifications

Figure 2.1: *Spray G injector geometry [4, 78, 105]*

Patternation data analysis [59] and experimental X-ray radiography measurements performed at 2 mm from the injector tip [110] demonstrated a deflection of the spray plumes towards the injector axis leading to a definition of the *plume direction* angle,

Table 2.1: *Spray G injector characteristics [78]*

Fuel	Iso-octane
Ambient gas	Pure nitrogen (inert)
Injector type	Delphi solenoid-activated
Nozzle type	Valve-covered orifice (VCO)
Number of holes	8 (equally spaced)
Nozzle shape	Step hole
Orifice diameter (specification)	0.165 mm
Orifice diameter (measured)	0.175 mm
Orifice length	0.16 - 0.18 mm
Step diameter (specification)	0.388 mm
Step diameter (measured)	0.400 mm
Orifice drill angle	37° relative to the nozzle axis
Full outer angle	80°

closer to a value of 33, 34° compared to the nominal 37° drill angle. This phenomenon could be explained by a deviation of the internal flow taking place into the nozzle before the spray leaves the injector. Such a behavior appears to also depend on the specific operating conditions with strong plume to plume interactions typical of injection events such as G2 (flash boiling) and G3 (low evaporating condition) that further enhance the difference [121].

A set of reference operating conditions was defined to ensure consistency between experimental and numerical activities and to create a wide literature dataset. Among them, the so called *G1* operating point represents the baseline benchmark whose specifications are reported in Tab.2.2.

Table 2.2: *Spray G baseline operating condition*

Injection pressure	200 bar
Fuel temperature	363.15 K
Ambient temperature	573.15 K
Ambient density	3.5 $\frac{kg}{m^3}$
Injected mass	10 mg
Electronic injection duration	680 μs
Hydraulic injection duration	780 μs

Among the different data injection pressure, fuel temperature, injected mass and

injection duration are parameters which are equal for all the proposed ECN operating conditions. Only ambient temperature and ambient density are changed, as it is shown in Tab.2.3, with the aim to replicate real GDI engine-like operating points ranging from early injection to late injection events.

Table 2.3: *ECN reference cases: ambient properties*

Condition	**Temperature** $[K]$	**Density** $\left[\frac{kg}{m^3}\right]$
G2	333	0.5
G3	333	1.01
G4	573	7.0
G7	800	9.0

More in detail the main characteristics of each ECN operating condition are summarized as follows:

- G1, baseline operating point defined by the ECN for the Spray G injector.
- G2, injection process taking place under a state of flash-boiling fuel evaporation.
- G3, typically related to GDI engines early injection events with very low ambient density.
- G4 and G7, modern GDI engine late injection events characterized by high ambient density.

The reference mass flow rate profile is shared between all the described cases and it was experimentally measured at General Motors (GM) R&D [5] and at CMT-Motores Termicos [84].

For the sake of this thesis work other bespoke Spray G conditions were considered sa a benchmark for the spray sub-models [78] adopted in preliminary simulations. Experimental investigations were carried out by Istituto Motori (IM) CNR of Napoli by injecting iso-octane [ρ = 690 $\frac{kg}{m^3}$ at 25°C] in a heated constant-volume pressurized vessel. In Tab.2.4 the main operating properties of the bespoke Spray G conditions are reported. The nomenclature of the case is kept consistent with the post-processing activity and the numerical results of the main reference literature work [78].

Case 1, 2 and 3 are coincident with the baseline ECN G1 condition in terms of main operating parameters. Moreover, the injection pressure was considered as well as a

Table 2.4: *Bespoke simulated cases, operating properties*

Case	p_{inj} [bar]	ρ_{amb} $\left[\frac{kg}{m^3}\right]$	T_{amb} [K]
Case 1,2,3	200	3.5	573.15
Case 4	200	3.5	473.15
Case 5	200	3.5	473.15
Case 6	200	3.5	373.15
Case 7	200	3.5	333.15
Case 8	150	3.5	573.15
Case 9	150	3.5	333.15
Case 10	150	1.0	333.15
Case 11	100	1.0	333.15
Case 12	50	1.0	333.15

varying parameter for the bespoke conditions. Within this context, since experimental measurements for the mass flow rate profile at 150 bar, 100 bar and 50 bar of injection pressure were not available in literature the reference profile at 200 bar was used as a starting point to derive them. This result was achieved by assuming a constant *discharge coefficient* c_d defined according to Eq.2.1 [19]:

$$c_d = \frac{u_{mean}}{u_{Bern}} \tag{2.1}$$

The term u_{Bern} is the Bernoulli velocity calculated according to Eq.2.2:

$$u_{Bern} = \sqrt{\frac{2p_{inj}}{\rho_{fuel}}} \tag{2.2}$$

where p_{inj} is the injection pressure and ρ_{fuel} is the density of the liquid fuel under incompressible conditions. By assuming a constant discharge coefficient and by evaluating the u_{Bern} for each injection pressure value it was possible to derive for every case the new u_{mean} term which stands for the average velocity inside the nozzle hole under a slug flow state. The new mass flow rate profiles and the new values of injected mass were consequently evaluated as it is shown in Fig.2.2 and reported in Tab.2.5.

Table 2.5: *Scaled values of injected fuel mass*

Injection pressure [bar]	Injected mass [mg]
200	10
150	8.66
100	7.07
50	5

With reference to the experimental setup employed by Istituto Motori [78], three

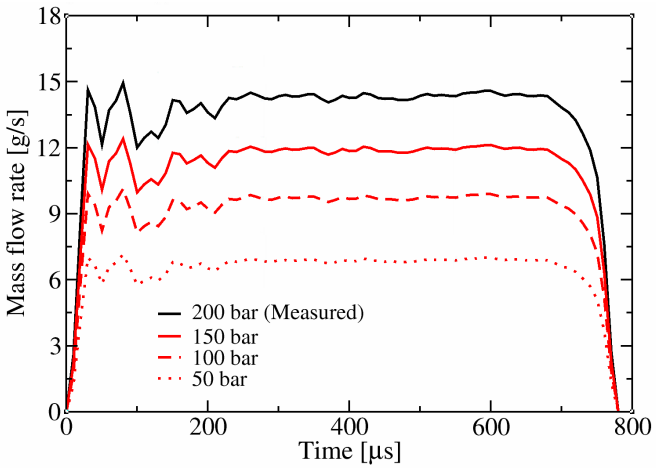

Figure 2.2: *Scaled mass flow rate profiles [78]*

large windows (80 mm in diameter) were placed surrounding the cylindrical test chamber in an orthogonal way with the layout giving full optical access to the internal test section of the combustion chamber. The fuel was injected through a common rail system by varying the injection pressure from 50 bar to 200 bar while the injection timing was set at 680 μs for all the tested conditions. The common rail device was heated by an electrical resistance and controlled in temperature by a J-type thermocouple. A governor managed the temperatures of nozzle and fuel via a remote computer with both of them kept at 363.15 K. The ambient temperature control system was composed by electrical heaters, temperature controller and sensor. Electrical heaters were used to increase the temperature of the gas in the test chamber up to the required value. The inlet gas was heated homogenously because the resistances were twined covering all the internal walls of the test chamber. Finally, the inner part of the test chamber was provided with an insulating layer to reduce heat losses from the gas. This layout ensured a homogenous temperature of the gas in the whole chamber.

Fig.2.3 shows the schematic of the injector with respect to the camera line-of-sight. This configuration represents the ECN "primary view" [4] and it was considered as reference for all the numerical simulations reported in this thesis work.

A high-speed C-Mos camera located into a combined Mie scattering/Schlieren optical configuration acquired pictures of the liquid and vapor phases of the evolving sprays in a quasi-simultaneous fashion and using the same optical path. High-speed Mie scattering imaging was used to visualize the liquid phase while the corresponding Schlieren

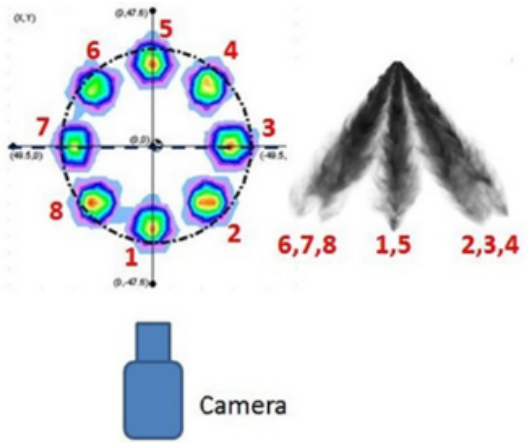

Figure 2.3: *Schematic of the Spray G injector configuration [4, 78]*

was employed to visualize both the liquid and vapor phases. More details of the overall configuration and of the adopted optical setup are reported in literature [12, 67, 78, 80].

The discernment of the liquid core, the more or less finely atomized fluid and the vapor phases were selected applying a customized algorithm of image processing developed under Matlab platform. Schlieren and Mie-scattering images were treated differently due to the diverse luminosity of the spray image. A more detailed description of the adopted procedure is reported in literature [67, 78].

2.1.2 Post-Processed Fields

In this section the main post-processed quantities which will serve as the basis fo the validation of the numerical models are introduced. For each field the definition and the description of its evaluation procedure are provided.

To validate the different numerical spray sub-models in the context of a GDI injection process the following fields were numerically investigated:

- axial vapor penetration [59]. Numerically computed as the maximum axial distance from the injector tip where a mixture fraction of 0.1% is found on the basis of the adopted ECN references. In case of multi-holes configurations such as the Spray G geometry the axial direction is given by the injector axis [4]. Experimental techniques for the evaluation of the axial vapor penetration are based on Schlieren methodologies [78, 79].

- Axial liquid penetration [59]. Its evaluation has been initially based on liquid

mass [78] and it was defined as the maximum axial distance from the injector tip where 99% of the liquid mass is found on the basis of the adopted ECN references. The relative experimental evaluation was coherently carried out by means of a Mie scattering technique [78]. From the ECN6 Workshop onward, both the experimental and numerical approaches have been updated with the aim to provide a more rigorous and accurate method for liquid estimation. To minimize the differences between experiments and simulations an approach based on a projected liquid volume (PLV) method derived from diffuse back-illumination (DBI) measurements was defined for the ECN6 Gasoline Sprays Guidelines [2, 55]. Compared to the Mie scattering technique the advantage of DBI is that there is self-calibration for the intial density as the extinction produced by the spray droplets is used to provide a measure related to the liquid volume fraction along the light path. From the numerical side the estimation based on liquid mass was found not to be accurate enough after the end of injection (EOI) threshold and it was thus discarded. A coherent methodology based on the PLV field was considered instead. Within this context, an Eulerian liquid volume fraction (LVF) field was derived from the Lagrangian spray parcels liquid mass and then integrated along different lines to generate the PLV Eulerian field on a 2D background mesh, as it is shown in Fig.2.4

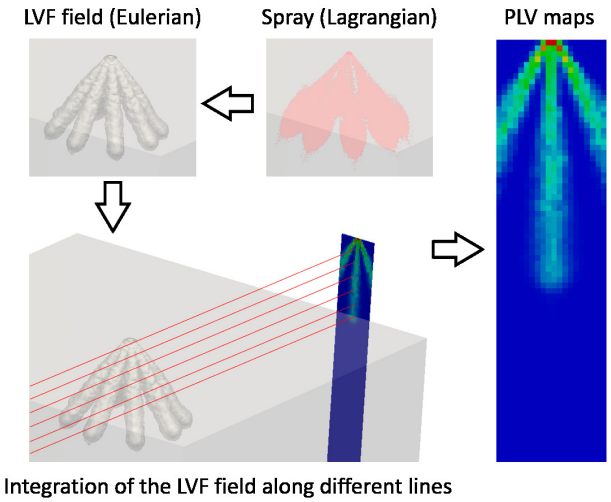

Figure 2.4: *Numerical methodology for the definition of the PLV Eulerian field [55, 79]*

The projected liquid volume is related to the liquid volume fraction by the mathematical definition reported in Eq.2.3

$$\int_{-y_\infty}^{y_\infty} LVFdy \tag{2.3}$$

where y is the cross-stream direction of integration with the LVF field being expressed in mm^3_{liquid}/mm^2. Under the assumption of a monodisperse droplet size distribution the optical thickness τ of the liquid along the experimental beam path was related to the extinction according to Eq.2.4

$$\tau \frac{\pi \frac{d^3}{6}}{{C_{ext}}^*} = \int_{-y_\infty}^{y_\infty} LVFdy \tag{2.4}$$

where d is the droplet diameter (assumed to be equal to 7 μm based on SMD values measured by GM) and ${C_{ext}}^*$ is the extinction cross-section parameter, derived from the Mie theory and chosen equal to $44.6 \cdot 10^{-6} mm^2$ for the Spray G with iso-octane as a reference fuel. The ${C_{ext}}^*$ parameter, depending on droplet size, wavelength and collection angle, is assumed as a finite value equal to 225 mrad at 633 nm [79]. From the ECN6 Workshop onwards two different thresholds were proposed and are currently adopted to account for sensitivities related to liquid penetration in experiments and models. The "high" threshold is defined according to Eq.2.5

$$\int_{-y_\infty}^{y_\infty} LVFdy = 2.0 \cdot 10^{-3} \frac{mm^3 liquid}{mm^2} \tag{2.5}$$

while Eq.2.6 reports the "low" threshold value [79]

$$\int_{-y_\infty}^{y_\infty} LVFdy = 0.2 \cdot 10^{-3} \frac{mm^3 liquid}{mm^2} \tag{2.6}$$

To adopt a double threshold approach allowed to better understand the in-plume liquid evolution both in the core and at the tip.

- Axial PLV profiles [79]. An innovative approach proposed in the latest part of this thesis work, it allows to further validate the in-plume liquid distribution by plotting the inner plume, axial PLV profile over time against comparable experimental data also based on the general PLV field definition.

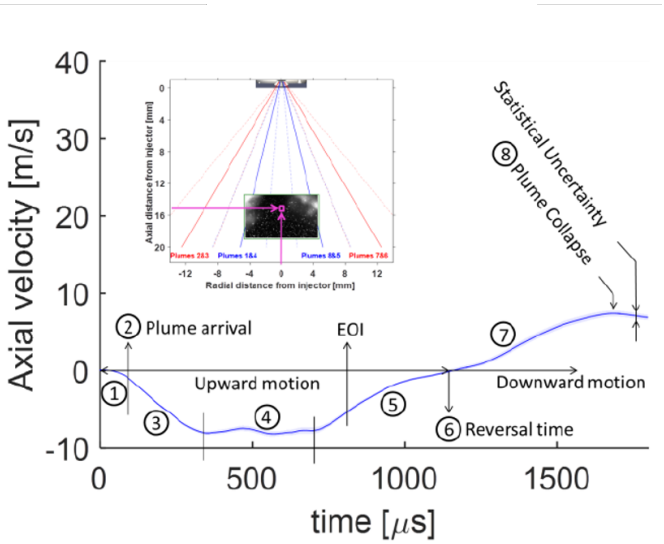

Figure 2.5: *Experimental profile of the centerline velocity [107]*

- PLV maps [79]. A new method as well adopted in this work to investigate the numerical spray morphology and to compare it with the experimental jet. It is based on a bidimensional sampling over time of numerical and experimental PLV data.

- Centerline axial gas velocity [105]. Numerically, it represents the gas velocity sampled over time axially at a position 15 mm downstream of the injector nozzle. Experimentally, it is evaluated 15 mm downstream of the injector by means of a particle image velocimetry (PIV) methodology. The reference experimental velocity profile is reported in Fig.2.5 and it is to this day only available for the baseline G1 condition.

- Spray G liquid droplets velocity and Sauter Mean Diameter (SMD), experimentally evaluated at different times by means of a Phase Doppler interferometry (PDI) approach [81].

- Overall range of validity of SMD data for a modern GDI injector as a function of the injection pressure. Data sampled from experimental literature researches carried out by Hammer et al. [33].

2.2 The Optical Access IFPEN Engine

The IFPEN optical access engine is characterized by a pent-roof, four-valves (two for the intake and two for the exhaust) configuration with centrally mounted fuel injector and spark plug. Its main specifications are reported in Tab.2.6.

Table 2.6: *IFPEN optical access engine specifications*

Bore	77 mm
Stroke	85.8 mm
Con. rod length	144 mm
IVO/IVC	360/573 CA
EVO/EVC	129/361 CA
Speed	1200 rpm
IMEP	4.5 bar

The characteristics of the GDI injector which is coupled with the optical access engine are shown in Tab.2.7. As it is also highlighted in Fig.2.6, such a geometry consists into a top mounted, 6-hole configuration.

Table 2.7: *IFPEN GDI injector specifications*

Position	Top mounted
Holes	6
Injection temperature	358.15 K
Injected mass	12.28 mg
SOI	460/540 CA

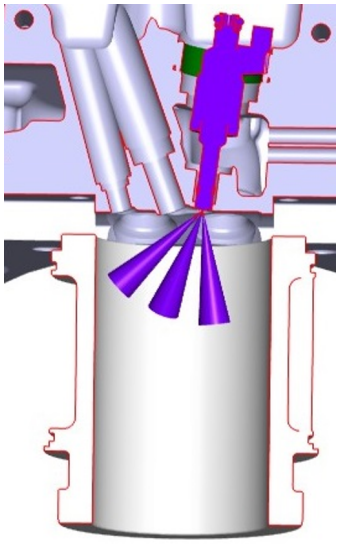

Figure 2.6: *Schematics of the IFPEN engine top mounted GDI injector*

Two different SOI values equal to 460 crank angle degrees (CA) and 540 CA were considered along with three types of intake ducts and intake ports configurations for the optical access engine. In particular, a *standard* pent-roof tumble geometry (Fig.2.7(a)) was compared to a *high-tumble* (Fig.2.7(b)) and to a single valve *swumble* (Fig.2.7(c)) configuration. The aim of the analysis was to investigate the effects of different combinations of start of injection times and intake flow charge motions on the air-fuel mixture formation and the subsequent combustion process.

(a) Standard (b) High-tumble (c) Swumble

Figure 2.7: *Schematics of the three tested IFPEN engine intake ports configurations*

A detail extracted from the generated computational grids (Fig.2.8(a)) allows to observe the distinct presence of engine crevices at the piston while Fig.2.8(b) provides a view of the particular intake seat shape which is typical of the high-tumble ports configuration.

(a) Crevices

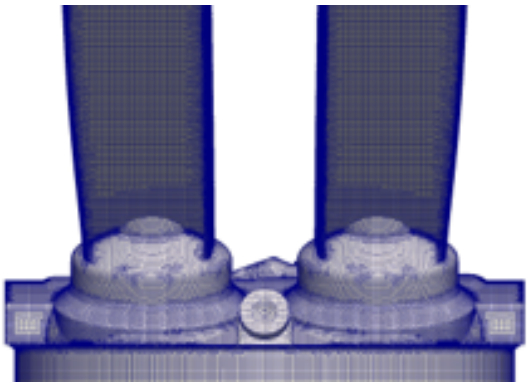

(b) High-tumble intake ports configuration

Figure 2.8: *Geometrical details of the IFPEN GDI engine*

2.3 The Optical Access Darmstadt Engine

The Darmstadt engine consists into an optically accessible single cylinder, direct injection, spark-ignition unit characterized by a twin-cam, overhead-valve, pent-roof setup [8]. As it is shown in Fig.2.9, two different configurations are available for the cylinder-head respectively called "wall-guided" and "spray-guided" [8]. The former is equipped with a side-mounted injector and a centrally located spark plug while the latter is characterized both by a centrally mounted fuel injector and spark plug. In the context of this work, as the subject of the investigation consisted into the coupling between the Spray G injector and the optical access Darmstadt engine the "spray-guided" configuration was considered for the reported simulations.

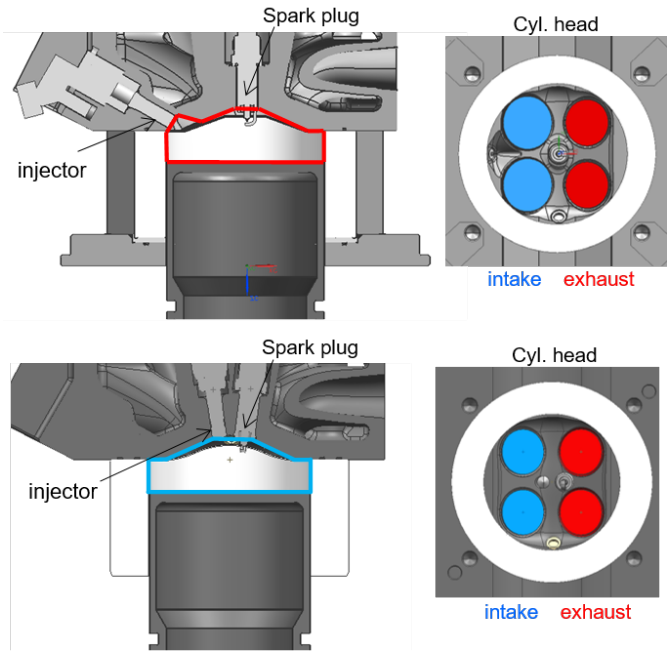

Figure 2.9: *Darmstadt engine, "wall-guided" (top) and "spray-guided" (bottom) configurations [8]*

The most relevant geometric specifications of the adopted engine configuration are reported in Tab.2.8-2.9.

Table 2.8: *Main engine geometric parameters [83]*

Bore	86 mm
Stroke	86 mm
Low regime	800 rpm
High regime	1500 rpm
Mean piston speed (low)	$2.29 \frac{m}{s}$
Mean piston speed (high)	$4.30 \frac{m}{s}$
Cylinder head cooling water temperature	333.15 K

Table 2.9: *Valve timing [83]*

IVO at 0.25 mm	**IVC at 0.25 mm**
347° aTDC	132° bTDC
EVO at 0.25 mm	**EVC at 0.25 mm**
127° aTDC	351° bTDC

Tab.2.10 displays the main engine operating conditions which were considered for

the full-cycle simulations that will be introduced in this work.

Table 2.10: *Operating conditions [83]*

		Regime [rpm]	
		800	1500
Intake pressure	0.95	A	C
[bar]	0.40	B	-

More details on the engine are available in dedicated literature data [18] while the schematics of the experimental test bench are reported in Fig.2.10. In particular, the advantages of such a setup are represented by the capability to reproduce a wide set of engine operating conditions while also taking into account a large range of measured quantities. As a consequence, conditioning of intake gas composition, pressure and temperature are possible as well as the specific control on boundary conditions and the adoption of gaseous port fuel injection [8].

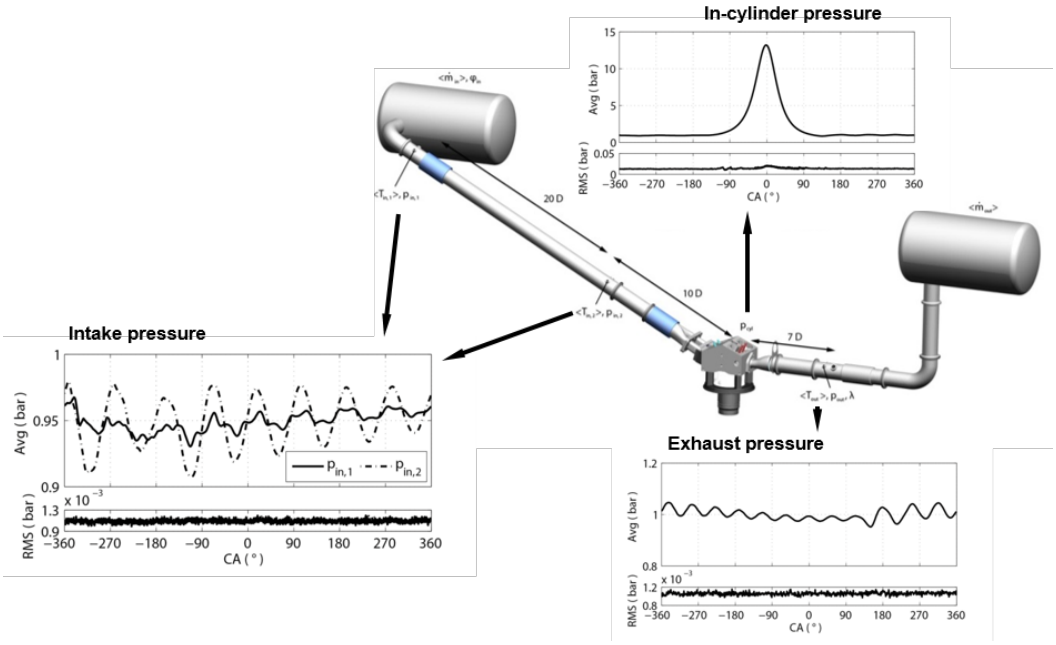

Figure 2.10: *Schematics of the Darmstadt engine test bench [8]*

CHAPTER 3

Fundamentals of the Numerical Methodology

In this chapter the fundamental aspects which stand at the core of the adopted numerical methodology are going to be introduced. The set of implemented sub-models will be described and validated in the upcoming sections of the thesis dedicated to the discussion of the computational results.

More in detail, the general numerical framework is introduced with a description of the main transport equations for the gas phase, the reference liquid injection management methodology and the selected approach for turbulence modeling.

3.1 The Numerical Framework

The open-source and C++ object-oriented OpenFOAM® numerical framework [1] was adopted as the basis of all the carried out CFD simulations and it was coupled with the LibICE code which consists into a set of engine-dedicated libraries, solvers and utilities developed by the Internal Combustion Engine (ICE) Group of Politecnico di

Milano. Overall, it is a numerical approach based on extensive validations performed during past works in the context of in-cylinder flow, fuel injection, mixture formation and combustion modeling for gasoline SI engines. [51, 52, 54, 66].

3.1.1 Transport Equations for the Gas Phase

On global terms, the liquid fuel injection process is governed by the principles of mass, momentum, energy and species conservation which can be described by means of a set of space-time partial differential equations that are numerically integrated.

The discretization and the solution of these equations are handled by means of a finite volume approach [29, 120] with an Eulerian-Lagrangian framework [13] employed to predict the liquid evolution and the gas-liquid interaction.

For a general Eulerian gas phase the differential conservation equations are expressed according to the generic formulation reported by Eq.(3.1)

$$\frac{\partial (\rho \phi)}{\partial t} + \bigtriangledown \cdot (\rho \phi \boldsymbol{U}) = \bigtriangledown \cdot (\Gamma \bigtriangledown \phi) + S_{\phi} \tag{3.1}$$

where the term ϕ represents a generic transport equation variable which is set to be equal to:

- 1, for the mass conservation equation;
- U_i, for the i^{th} component of the momentum conservation equation;
- enthalpy (h), for the energy conservation equation;
- mass fraction Y_i, for the i^{th} specie conservation equation.

Other terms of the transport equation (3.1) are the velocity **U**, the diffusion coefficient Γ and the general source term S_{ϕ} [120].

More in detail, from left to right each component of the equation represents:

- the rate of change of ϕ over time;
- the convective flow rate of ϕ;
- the diffusive increase rate of ϕ;
- the rate of increase of ϕ due to a source term.

The final step of the finite volume method consists into the integration of Eq.(3.1) over a three dimensional volume V leading to the formulation reported by Eq.(3.2) and to the mathematical relation of Eq.(3.3) after the application of the Gauss' divergence theorem to the convective and diffusive terms of Eq.(3.2).

$$\int_V \frac{\partial (\rho\,\phi)}{\partial t}\,dV \,+\, \int_V \bigtriangledown \cdot (\rho\,\phi\,\boldsymbol{U})\;dV \;=\; \int_V \bigtriangledown \cdot (\Gamma \bigtriangledown \phi)\;dV \,+\, \int_V S_\phi\,dV \tag{3.2}$$

$$\frac{\partial}{\partial\, t}\left(\int_V \rho\phi\,dV\right) \,+\, \int_A \boldsymbol{n}\cdot(\rho\phi\boldsymbol{U})\;dA \;=\; \int_A \boldsymbol{n}\cdot(\Gamma \bigtriangledown \phi)\;dA \,+\, \int_V S_\phi\,dV \tag{3.3}$$

The term A stands for the boundary surface of the reference control volume. Such a system is valid for any continuum with the additional Newton's law of viscosity defining the viscous stresses τ_{ij} to take into account the force balance acting on the control volume boundaries. Within this context, the diffusion coefficient Γ of the momentum equation represents the result of the Newtonian assumption applied to the volume of fluid. More in detail, the viscous stresses τ_{ij} are expressed according to Eq.(3.4) and Eq.(3.5)

$$\tau_{ii} \;=\; 2\mu\frac{\partial\, U_i}{\partial\, x_i} \,+\, \lambda \bigtriangledown \cdot \boldsymbol{U} \tag{3.4}$$

$$\tau_{ij} \;=\; \tau_{ji} \;=\; \mu\left(\frac{\partial\, U_i}{\partial\, x_j} \,+\, \frac{\partial\, U_j}{\partial\, x_i}\right) \tag{3.5}$$

For a compressible flow, two specific viscosities acting as constants of proportionality are introduced which are:

- the dynamic viscosity μ, to relate the stresses to the linear deformation;
- the second viscosity λ for the volumetric components of the deformation, equal to $-2/3\,\mu$ for compressible gases.

A volumetric dissipation function acting as a source term can be rearranged from the shear stresses with reference to the energy conservation equation. Moreover, as the

fuel injection process is a transient and thus time-dependent phenomenon the set of equations must be integrated with respect to time t over a user-defined interval Δt.

3.1.2 Turbulence Modeling

The previously introduced set of partial, differential *Navier-Stokes* equations accurately describes the motion of a viscous fluid. More in detail, every physical phenomenon related to internal combustion engines is characterized by a high level of turbulence intensity with phase flows being three-dimensional, unsteady and fluctuating under coherent spatial structures that can be distinguished in:

- larger structures, which are influenced by the domain geometry and carry most of the flow energy leading to mass, momentum and heat exchange;
- smaller structures, which are dissipative and dominated by viscosity. The smallest length scales are around the size of the *Kolmogorov scale*.

Within this context, a comprehensive numerical simulation of a turbulent flow should require space and time discretizations capable to solve the Kolmogorov microscale and its associated characteristic time [29]. In this regard, a direct numerical simulation (DNS) approach would provide an analytical solution of even the smallest scales at the cost of considerably high required computational resources. On the other hand, large eddy simulations (LES) methodologies provide an analytical resolution of the largest scales while modeling the smallest ones, thus resulting in a more computational affordable approach compared to DNS solutions. LES CFD simulations are currently becoming more and more important in research investigations of the far-field liquid spray evolution [105]. This thesis work was instead based on a Reynolds-Averaged Navier-Stokes (RANS) approach with whom the Navier-Stokes equations are treated with a statistical averaging mechanism which models the effects of both large and small turbulence scales. Since every scale of turbulence is modeled rather than analytically solved RANS simulations are considerably less demanding in terms of computational time compared to LES counterparts. As a consequence, even if available computing power should nowadays be more than enough to perform LES CFD simulations of an in-vessel spray, a RANS approach was chosen because the proposed numerical methodology had

to ensure to be coherently and efficiently applicable to complex, full-cycle simulations of modern GDI engines in the context of both research and industrial projects.

By separating the local value of the variable into its mean and the fluctuation around the mean specific equations for the mean properties can be derived. Generally, three different averaging methods can be employed according to the characteristics of the turbulent flow:

- time-averaging in a fixed point of space, in case of stationary turbulence;
- space-averaging for a fixed moment in time, in case of homogeneous turbulence;
- *ensemble average* for a series of identical experiments

Moreover, Reynolds (unweighted) averaging is applied to uncompressible flows while Favre averaging (weighted) is adopted for compressible problems.

In RANS equations, the average of the fluctuating components provides an additional term in Eq.(3.1) coupled with diffusion to give the *effective* diffusion coefficient which is reported in Eq.(3.6)

$$\Gamma^{'} = \Gamma_{dyn} + \Gamma_{turb} \tag{3.6}$$

where Γ_{dyn} is the dynamic component and Γ_{turb} represents the turbulent term which is related to the turbulent viscosity μ_{turb} [41]. Within this context, the purpose of a turbulence model is to close the system of mean flow equations by providing suitable expressions for the modeling of the Reynolds stresses and the scalar transport terms. In this regard, classical literature RANS solutions are:

- the zero equation (mixing-length) model;
- the two-equations models;
- the Reynolds stress equation model;
- the Algebraic stress model.

In this work the two-equations standard $k - \varepsilon$ turbulence model was used as a reference approach for all the performed simulations. The model was chosen to ensure the

maximum level of reliability and numerical consistency between spray investigations carried out under static vessel conditions and full-cycle engine simulations. In fact, the final aim of the activity was to improve the available numerical setup for injection and gas exchange modeling in GDI engines. As such, coherent comparisons and investigations had to be necessarily carried out against previous LibICE-based spray and engine research activities which were proposed with the standard $k-\varepsilon$ as the reference turbulence model. Moreover, previous ECN investigations on Spray A, Spray C and Spray D injectors [3] demonstrated that the most accurate results were achieved with the standard $k-\varepsilon$ turbulence model coupled with the round-jet correction [90]. Major effects were observed on fundamental parameters such as axial vapor penetration and gas velocity for which alternative turbulence models like RNG $k-\varepsilon$ and SST $k-\omega$ did not appear to provide any benefit in terms of accuracy. To further address this argument, in the Appendix of the thesis a comparison was reported for the baseline ECN Spray G1 condition respectively simulated with round-jet correction standard $k-\varepsilon$ and RNG $k-\varepsilon$ turbulence models. Scalable wall functions were also employed to ensure an optimal compromise between wall treatment accuracy and required computational resources for mesh generation and refinement.

More in detail, the standard $k-\varepsilon$ model introduces two transport equations for the turbulent kinetic energy k and the turbulent dissipation rate ε. The turbulent viscosity μ_{turb} is thus expressed as a function of the two new transported variables according to Eq.(3.7)

$$\mu_{turb} = \rho C_{\mu} \frac{k^2}{\varepsilon} \tag{3.7}$$

where ρ is the density and the term C_{μ} represents a general coefficient of the model.

More details about the effects of the adopted turbulence model on the simulated spray will be reported in the following chapters.

3.1.3 Liquid Injection Modeling

In simulations related to in-vessel or in-engine GDI injections two different phases should be modeled being them the liquid fuel emerging from the injector and the surrounding gas which includes both air and evaporated fuel. The evolution of the liquid

spray should account for the different phenomena occurring on the liquid surface and for evaporation, heat transfer and drag which stand at the basis of the physical interaction between the spray and the gas phase.

As it was anticipated in 1.2 the fully Eulerian volume of fluid (VOF) [37] methodology can be chosen for modeling the liquid spray. This approach requires the cell size of the computational domain to be smaller than the smallest liquid droplet. As a consequence, it cannot be considered as a feasible method for cases such as those described in this thesis for which the numerical setup must be applicable without distinctions both under vessel and real engine conditions. On the other hand, it currently represents the preferred approach if the aim is to understand the fundamental phenomena associated to small scales and conditions such as the in-nozzle liquid evolution or the near-nozzle primary atomization [69].

In this work a coupled Eulerian-Lagrangian approach was adopted instead [13] for which the liquid fuel is represented by the Lagrangian component and pockets of droplets are injected into the Eulerian (gas) phase. The spray is represented by a finite number of discrete parcels each one containing a statistical number of droplets N_p all with the same properties. The main characteristics of a Lagrangian approach are that:

- the N_p quantity does not have to be an integer number;
- the parcels are tracked through the gas;
- the spray consists of a number of discrete parcels;
- generally, the higher is the number of parcels the better the spray is modeled;
- the mass of the parcels is determined according to Eq.(3.8)

$$m_p = N_p \cdot m_d = N_p \cdot \rho_l \cdot \frac{\pi D^3}{6} \tag{3.8}$$

  where D is the droplet diameter and ρ_l is the liquid density;

- the gas phase is solved by means of Eulerian Navier-Stokes equations with new source terms introduced to account for the interaction between gas and spray;
- the numerical diffusion is non-existent;

- multi-sized droplets can be fully adopted;
- there is no necessity to solve physical scales;
- coarser grids can be used compared to a fully Eulerian approach thus saving on the overall required computational time. Specifically, this aspect makes the Lagrangian methodology a preferred way to numerically model the far-field spray in both static vessels and GDI engines. Still, a mandatory restriction consists into the fact that the grid cell size must be larger than the largest parcel.

Once injected into the computational domain the parcels are tracked according to an exchange of mass, momentum and energy with the gas phase. Navier-Stokes conservation equations get new source terms to account for the presence of the spray which are:

- the $\dot{\rho}_S$ evaporation source term for the mass conservation equation;
- the $\dot{\rho}_{S,i}$ evaporation source term of a single liquid component for the chemical specie conservation equation;
- the $\dot{\omega}_i$ chemical reaction (combustion model) source term for the chemical specie conservation equation;
- the $\mathbf{F}_S$ spray drag rate of momentum gain/loss per unit volume for the momentum conservation equation;
- the $\dot{Q}^c$ source term for the heat released by chemical reactions in the enthalpy equation;
- the $\dot{Q}^S$ source term for spray evaporation and heat transfer in the enthalpy equation.

The dispersed liquid phase equations for mass, momentum and time variation of the droplet temperature T_d are respectively described in Eq.(3.9), Eq.(3.10) and Eq.(3.11).

$$\frac{dm_d}{dt} = -\frac{m_d}{\tau_e} \tag{3.9}$$

$$\frac{d\vec{U}}{dt} = \frac{\vec{U_d} - \vec{U}}{\tau_u} + \vec{g} \tag{3.10}$$

$$\frac{\delta T_d}{\delta t} = \frac{T - T_d}{\tau_h} f - \frac{1}{c_{l,d}} \frac{h_v(T_d)}{\tau_e} \tag{3.11}$$

The term τ_e in Eq.(3.9) and Eq.(3.11) is the evaporation relaxation time while τ_u in Eq.(3.10) represents the momentum relaxation time which is expressed according to Eq.(3.12) where C_D represents the droplet drag coefficient.

$$\tau_u = \frac{4}{3} \frac{\rho_d D}{\rho C_D |\vec{U_d} - \vec{U}|} \tag{3.12}$$

In Eq.(3.11) $c_{l,d}$ is the liquid specific heat, f is the mass transfer factor, $h_v(T_d)$ represents the droplet heat of vaporization and τ_h is the heat transfer relaxation time.

As a consequence of the Eulerian-Lagrangian approach a set of dedicated sub-models are necessary to reproduce the most important physical phenomena associated to the liquid spray and its interaction with the gas phase. More in detail, by following the spray evolution from the injector nozzle to the far-field (Fig.3.1) sub-models are required to describe the following phases:

- **injection**, to provide the initial droplet diameter, velocity and size;
- **atomization**, to numerically reproduce the primary breakup of the liquid jet into dispersed droplets;
- **breakup**, to describe the secondary breakup which is characterized by droplet diameter reduction and stripping;
- **evaporation**, to take into account the amount of evaporating fuel mass;
- **heat transfer**, to take into account the heat exchanged between liquid and gas;
- **drag**, to compute the drag force acting on the droplets due to aerodynamic resistance;
- **collision**, to consider the possible physical interaction between each droplet;

- **dispersion**, to account for the interaction between the droplets and turbulent eddies;
- **wall impingement**, to consider the interaction between the liquid phase and solid walls, with consequent film formation. It is thus a mandatory model to be employed in engine simulations.

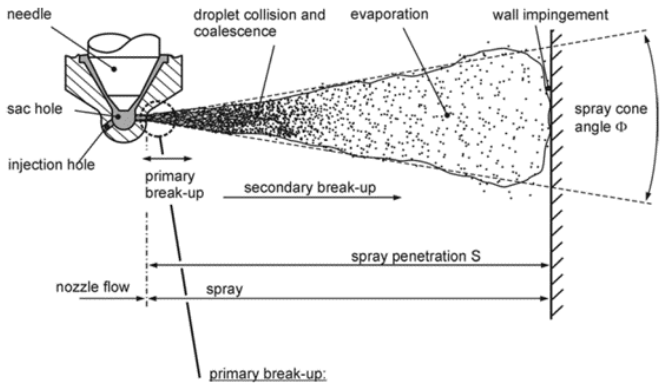

Figure 3.1: *Main physical phenomena related to the spray evolution [19]*

In this thesis work many of the listed sub-models were employed, investigated, validated and if necessary modified or implemented under new forms. A more detailed description will be provided in every chapter along with the respective achieved numerical results. In each case the ambient phase was modeled under the condition of a mixture of perfect gases while National Institute of Standards and Technology (NIST) tables were used to derive the main liquid properties as a function of the liquid temperature. Moreover, all simulations were run with a fully *Pressure Implicit with Splitting of Operator* (PISO) algorithm [29] without fields underrelaxation to ensure the best possible prediction accuracy.

For all the cases not subjected to superheated flash boiling evaporation a mass-based approach [19] was adopted for modeling the liquid evaporation according to Eq.3.13

$$\dot{m}_d = \pi D \beta \rho_v Sh \ln\left(\frac{1 - Y_{v,\infty}}{1 - Y_{v,s}}\right) \tag{3.13}$$

where β is the mass diffusion coefficient, Sh is the Sherwood number, ρ_v the vapor fuel density while $Y_{v,s}$ and $Y_{v,\infty}$ respectively represent the fuel mass fractions under saturation conditions and in the gas phase. For the cases subjected to flash boiling

specific evaporation models were implemented into OpenFOAM and will be described in the upcoming chapters.

Heat transfer between gas and liquid phases was modeled by means of the Ranz-Marshall correlation [94, 95] in all the simulations carried out in this work.

CHAPTER 4

Preliminary Numerical Spray G Investigation

In this chapter a fundamental assessment of a baseline numerical setup for the modeling of the Spray G injection process is reported. The main scope of the activity was to validate a comprehensive numerical set of sub-models under a wide range of operating points. Within this context, the reference ECN G1 condition was simulated and achieved results were validated both against experimental and reference numerical RANS literature data [105]. Furthermore, the analysis was extended to new bespoke Spray G operating points defined in collaboration with Istituto Motori (IM-CNR).

The organization of the chapter is as follows:

- in the first section the adopted numerical framework is introduced with a detailed focus on the most relevant sub-models such as those dedicated to the primary atomization and secondary breakup phases;
- in the second section achieved numerical results are presented and discussed;

- in the third section conclusions are drawn and advantages and negative aspects of the proposed methodology are assessed.

The different cases and the post-processed quantities are defined according to the nomenclature reported in Section 2.1.1 and Section 2.1.2.

4.1 The Numerical Framework

The main characteristics of the numerical setup are shown in Tab.5.1.

Table 4.1: *Numerical framework*

Turbulence model	Standard k-ε
Injection model	Lagrangian Huh
Atomization model	Huh-Gosman
Breakup model	Reitz-KHRT and Reitz-Diwakar
Evaporation model	Mass-based [19]
Heat transfer	Ranz-Marshall [94, 95]
Type of mesh refinement	Adaptive (AMR)
Base mesh cell size	4 mm
Minimum mesh cell size	1 mm or 0.5 mm

In particular, with reference to the computational mesh a fully hexahedral block with a base cell size of 4 mm was used for all the reported cases and coupled with an adaptive mesh refinement (AMR) procedure whose aim is to locally refine the grid where fuel mass is found. The refinement approach was based on the volumetric scalar *Yttf* field which is calculated as the overall fuel mass fraction found in the domain by taking into account both liquid and vapor components. To model the regions of the computational domain characterized by the presence of the spray two minimum mesh cell sizes of 1 mm and 0.5 mm were considered. These values were chosen for the sake of consistency with GDI full-cycle RANS engine simulations as they represent the current reference compromise between accuracy and required computational time.

A standard k-ε was employed as a RANS turbulence model with the reference liter-

ature value of 1.44 for the $C_{1\varepsilon}$ parameter.

4.1.1 Primary Atomization

The primary atomization was performed by means of the Huh-Gosman [39] model which introduces a finite number of primary discrete parcels (*blobs*) into the computational domain with the same diameter of that of the injector nozzle and a velocity which is function of the provided mass flow rate profile. An aerodynamically enhanced primary breakup is carried out by the model thus describing the parcels diameter reduction rate according to Eq.4.1

$$\frac{dD}{dt} = -C_5 \frac{L_a}{\tau_a} \tag{4.1}$$

where L_a and τ_a are the characteristic atomization length scale and the characteristic atomization time scale of the model while C_5 is a main constant. The term L_a is proportional to the turbulent length scale on the liquid jet L_{turb} while τ_a is directly dependent on both the turbulent (τ_{turb}) and aerodynamic (τ_w) time scales according to Eq.4.2. The C_3 and C_4 terms are two main model constants.

$$\tau_a = C_3 \cdot \tau_{turb} + C_4 \cdot \tau_w \tag{4.2}$$

The parameters L_{turb} and τ_{turb} are directly computed from the turbulent kinetic energy and the turbulent dissipation rate on the column jet surface which are in turn initialized by means of a zero-dimensional sub-model. New parcels are thus created from the parent droplet with the overall stripped mass that is calculated according to Eq.4.3

$$m_s = \rho_l \cdot N_p \cdot \frac{\pi}{6} \cdot \left(D_{old}^3 - D_{new}^3\right) \tag{4.3}$$

where ρ_l is the liquid fuel density, N_p is the number of parent droplets in the spray core, D_{old} is the initial parcel diameter and D_{new} is the new one at the end of the time-step. New parcels were created if the stripped mass was higher than 0.1 times the mass of the original parent parcel. According to the Huh-Gosman model the atomization length and time scales influence the initial spray plume cone angle α on the basis of the mathematical relation proposed in Eq.4.4 where U is the velocity of the droplets

leaving the injector nozzle.

$$tan\left(\frac{\alpha}{2}\right) = \frac{\frac{L_a}{\tau_a}}{U} \tag{4.4}$$

Basics assumptions for the *pdf* distribution of the secondary droplets diameter, included the definition of maximum and minimum values of the distribution itself, were kept coherent with those adopted in previous works on Lagrangian spray modeling [54]. As a consequence the size of the secondary droplets was related to that of the eddies generated by the turbulence on the jet surface.

4.1.2 Secondary Breakup

Atomized parcels with a gas Weber number (We_g, Eq.4.5) higher than the stable value (We_{crit}, equal to ~ 6) can undergo secondary breakup.

$$We_g = \frac{\rho_g U_{rel}^2 r}{\sigma_l} \tag{4.5}$$

The term ρ_g represents the gas density, U_{rel} is the liquid-gas relative velocity, r is the radius of the droplets contained in the parcel and σ_l is the liquid surface tension.

Two different secondary breakup models, *Reitz-Diwakar* and *Retiz-KHRT*, were employed for the simulations reported in this chapter with the aim to verify which one could better match the evolution of the spray when subjected to different ambient conditions and while minimizing the parameter recalibration activity.

The Reitz-Diwakar approach combines the effects of both *bag breakup* and *stripping* motion regimes [88]. As it is shown in Fig.4.1 bag breakup is performed if We_g is greater than We_{crit} in value. The term We_{crit} is equal to the model constant C_{b1} in the Reitz-Diwakar code. If also the condition reported in Eq.4.6 is satisfied stripping breakup is carried out instead, where Re_g is the gas Reynolds number defined in Eq.4.7 and C_{s1} is a model constant.

$$We_g > C_{s1} \cdot Re_g^{0.5} \tag{4.6}$$

$$Re_g = \frac{\rho_g mag\left(U_{rel}\right) D}{\mu_g} \tag{4.7}$$

The term D is the diameter of the droplets contained in the parcel and μ_g is the dynamic viscosity of the gas.

The respective breakup times τ_b of the two competing mechanism are reported in Fig.4.1 [42], with ρ, D_d and σ_d terms that are respectively equal to ρ_g, D and σ_l under the current nomenclature. The term ρ_d represents the liquid density of the droplet while C_{b2} and C_{s2} are two main model constants.

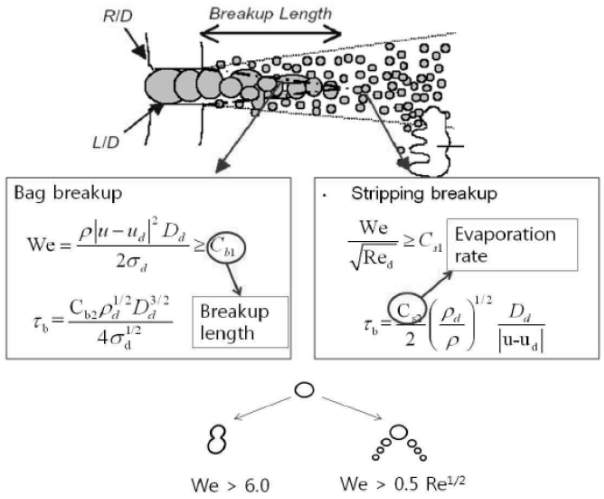

Figure 4.1: *Reitz-Diwakar breakup model [49]*

The Reitz-KHRT model predicts the secondary breakup by employing a combination of both the Kelvin-Helmholtz (KH) and Rayleigh-Taylor (RT) instability theories instead [19,96,108]. Within this context the RT mechanism is activated if the condition reported in Eq.4.8 is satisfied and *catastrophic* breakup is thus performed.

$$(time_p > \tau_{RT}) \,\&\, (\lambda_{RT} < D) \tag{4.8}$$

The term $time_p$ represents how long the RT waves have been growing on the parent liquid parcel surface while τ_{RT} is the characteristic RT breakup time directly related to the inverse of the most unstable RT grow rate Ω_{RT}. The term λ_{RT} is the wavelength of the fastest growing RT frequency computed according to Eq.4.9.

$$\lambda_{RT} = 2\pi C_{RT}\sqrt{\frac{3\sigma_l}{a\,(\rho_l - \rho_g)}} \tag{4.9}$$

The term C_{RT} is a main model constant while a is computed as reported in Eq.4.10 and it is in turn dependent on the liquid and gas densities, the liquid-gas relative velocity and the droplet drag coefficient C_D.

$$a = \frac{3}{4} C_D \frac{\rho_g U_{rel}^2}{\rho_l D} \tag{4.10}$$

The RT breakup mechanism does not perform a strip of secondary child parcels from the parent droplet. Instead, a new diameter is assigned to the same parent droplet by following the theory of the catastrophic breakup event. In particular the Reitz version of the KHRT model assigns the new D_{RT} parcel diameter according to Eq.4.11

$$D_{RT} = \frac{semiMass}{nDrops} \tag{4.11}$$

where $semiMass$ is a term computed as shown in Eq.4.12 with N_p being the number of droplets in the computational parcel.

$$semiMass = N_p \cdot D^3 \tag{4.12}$$

The parameter $nDrops$ is computed by following the mathematical relation of Eq.4.13.

$$nDrops = \frac{N_p D}{\lambda_{RT}} \tag{4.13}$$

As the Reitz-KHRT mechanism is implemented to operate under a full-exclusion condition, if the relation of Eq.4.8 is not satisfied the model checks for the KH (*wave*) breakup approach instead which is based on a stripping procedure with the aim to generate secondary child parcels from the initial parents. The diameter of the child parcels D_{KH} is computed according to Eq.4.14 where B_0 is a main model constant kept equal to 0.61 and λ_{KH} is the characteristic KH breakup wavelength.

$$D_{KH} = 2.0 \cdot B_0 \cdot \lambda_{KH} \tag{4.14}$$

If d_{KH} is verified to be smaller than the original parcel diameter D the KH mechanism starts with the parent parcels that get characterized by the diameter reduction rate expressed in Eq.4.15:

$$\frac{dD}{dt} = -\frac{D - D_{KH}}{\tau_{KH}} \tag{4.15}$$

The term τ_{KH} is the characteristic KH breakup time function of λ_{KH}, $Omega_{KH}$ (which is the most unstable KH grow rate) and the main model constant B_1.

4.2 Results

This part of the work consisted into three different phases which are reported as follows:

1. subsection 1, baseline G1 condition (cases from 1 to 3). Validation of the different combinations of numerical models against the baseline Spray G1 operating point with focus on the spray penetration. Variation of "drill angle" and "plume cone angle" and an analysis of the centerline gas velocity are performed.

2. subsection 2, CNR cases from 4 to 7. The best achieved numerical combinations were tested under the baseline injection pressure and ambient density but with decreasing values of ambient temperature (473.15 K, 373.15 K and 333.15 K) allowing for higher spray penetrations. The purpose of the calculations was to assess which secondary breakup model could better reproduce the spray changes due to the different ambient conditions while minimizing the user parametric re-calibration. The most accurate model was then used for the simulation of all the remaining cases.

3. subsection 3, CNR cases from 8 to 12. The numerical setup was finally validated for a wide range of modern GDI engine-like operating conditions with variations in injection pressure, ambient temperature and ambient density.

The calibration of the Huh-Gosman atomization model was carried out once and then kept constant for all the proposed simulations. The main adopted operating parameters are reported in Tab.4.2. The value We_{Limit} represents the Weber gas minimum threshold value below which the atomization phase is stopped.

4.2.1 Baseline G1 Condition

Case 1, Case 2 and Case 3 allowed to study the effects of secondary breakup, "plume direction" (PD) and "plume cone angle" (PCA) under the baseline ECN Spray G1 con-

Table 4.2: *Main Huh-Gosman model constants*

Constant	Value
C_3	0.95
C_4	0.38
C_5	0.25
We_{Limit}	40

dition. The main numerical details of these three cases are reported in Tab.4.3.

Table 4.3: *Numerical details of cases 1, 2 and 3*

Case	Breakup model	*PD* [deg]	*PCA* [deg]
Case 1	Reitz-KHRT	37	10
Case 2	Reitz-Diwakar	37	10
Case 3	Reitz-KHRT	34	20

As it is shown in Fig.4.2 results accuracy was first assessed in terms of liquid and vapor penetration against the reference ECN experimental data [80] available at the time. Within this context, the cases displayed a very similar spray behavior.

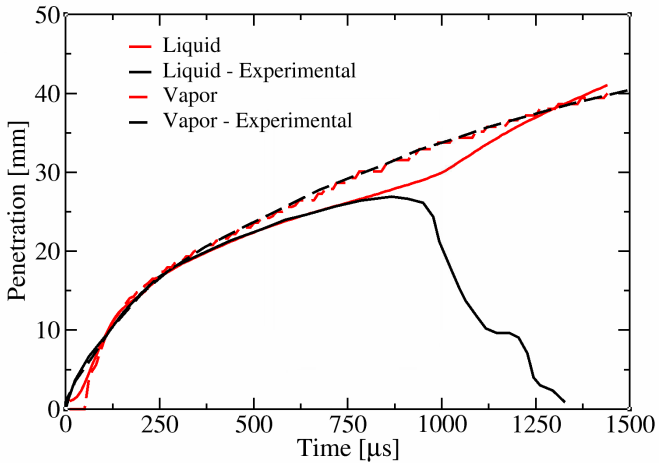

Figure 4.2: *Case 1, computed liquid and vapor penetrations [76]*

Since the approach based on the percentage of liquid mass was adopted in this case to predict the axial liquid penetration, the plotted trend is shown to increase even after the EOI threshold because liquid parcels are still present in the computational domain. While underestimated evaporation between 500 μs and EOI might happen when dealing with the Spray G injector due to complex plume-to-plume interactions, the reported results show a correct trend for both liquid penetration and evaporation.

With reference to the $C_{\varepsilon 1}$ of the standard k-ε turbulence model, previous studies

demonstrated that more accurate results [113] could be achieved by increasing the baseline 1.44 value with thus a reduced overprediction tendency of the round jets spreading rate [32]. On the other hand other literature data [99] reported the possibility to achieve accurate results even with values lower than 1.44 (1.35). Still, a persistent sensibility of the solution to the plume cone angle value was observed irrespective of the adopted $C_{\varepsilon 1}$ parameter. Within this context, a preliminary analysis carried out for the cases reported in this chapter demonstrated that a value of 1.5 increased the vapor penetration, especially when coupled with a mesh cell size of 0.5 mm. However it was also observed a steeper liquid penetration curve not matching the flattening trend of the experimental data in the range between 500 μs and 750 μs. Given all the possible uncertainties in this matter and for the sake of simplicity $C_{\varepsilon 1}$ was kept equal to 1.44 for the preliminary simulations reported in this section, leaving a more detailed investigation for the upcoming chapters.

Fig.4.3 reports an axial velocity comparison between results of Case 1 (computed at a distance of 15 mm from the injector nozzle), literature experimental PIV measurements and results from RANS simulations which were a reference at the time [105].

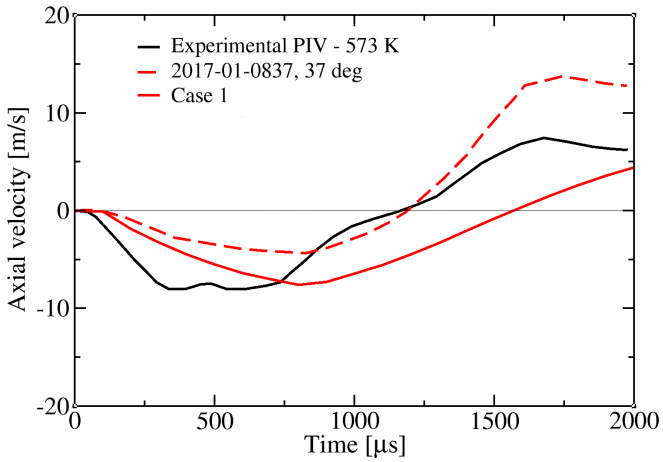

Figure 4.3: *Case 1, computed axial velocity at 15 mm from the injector nozzle [76]*

As it was described in the reference work [76] Case 1 shows a recirculation zone which is both faster in its formation and of greater negative velocity (nearly -9 $\frac{m}{s}$) compared to previous RANS results. With respect to the benchmark literature RANS results [105] it is possible to observe that the computed upward motion zone of the cen-

terline velocity profile is considerably underpredicted compared to experimental data. This means that the diameter of the parcels nearby the injector nozzle is too small, fact which leads to a negligible entrainment with the surrounding gas phase which thus remains closer to its original quiescent condition. Further proof of this phenomenon stands in the overprediction of the computed centerline velocity trend during the downard motion phase which is influenced by the fine secondary droplets being present in the computational domain. Instead, Case 1 behaves almost in an opposite way by better predicting the negative peak, fact which is index of a good parcels diameter distribution prediction. However a considerable delay in reaching the positive centerline velocity values is observed showing an underpredicted secondary breakup activity throughout the spray plumes. Case 2 behaved coherently with Case 1 while the lower PD of Case 3 had the effect to increase the negative peak beyond a value of -10 $\frac{m}{s}$ thus exceeding the experimental threshold as expected from a targenting closer to the injector axis direction. Case 3 was also characterized by a faster increase of the positive axial velocity after the EOI because of its larger PCA value. However this behavior was not enough to compensate the considerably lower negative peak of recirculation velocity.

Fig.4.4(a)-4.4(c), Fig.4.5(a)-4.5(c) and Fig.4.6(a)-4.6(c) report a comparison between experimental (Mie scattering) and computed liquid spray morphology, for Case 1 and Case 3 respectively, under different times after SOI (160 μs, 560 μs and 1040 μs).

(a) Experimental Mie scattering (b) Computed spray, Case 1 (c) Computed spray, Case 3

Figure 4.4: *Spray morphology validation, 160 μs [76]*

It can be observed that the experimental spray PCA is considerably greater than the 10° value numerically adopted for Case 1. Moreover, at each reported time there is a significant difference in shape between the experiments and both simulated cases. The effect is however not particularly visible at 160 μs, fact which may suggest the

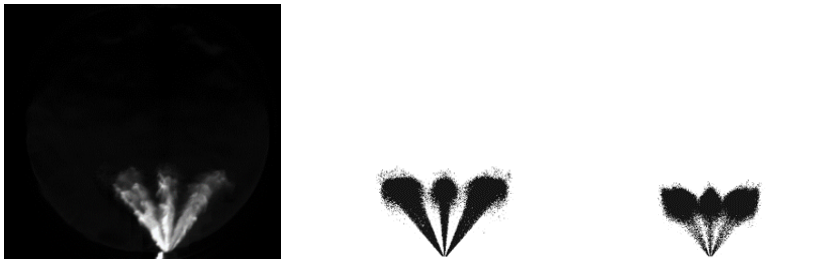

(a) Experimental Mie scattering (b) Computed spray, Case 1 (c) Computed spray, Case 3

Figure 4.5: *Spray morphology validation, 560 μs [76]*

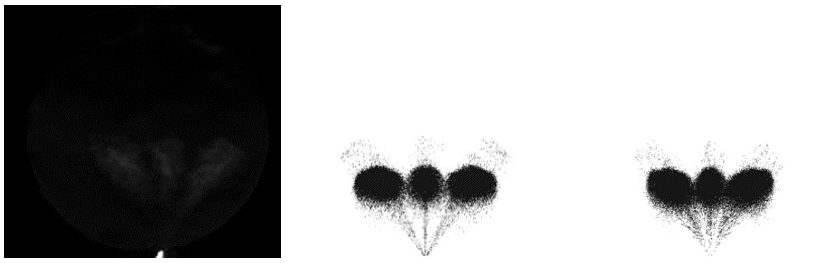

(a) Experimental Mie scattering (b) Computed spray, Case 1 (c) Computed spray, Case 3

Figure 4.6: *Spray morphology validation, 1040 μs [76]*

phenomenon to be strictly related to the secondary breakup phase. More in detail it appears to be a consequence of an overpredicted RT catastrophic breakup from the Reitz-KHRT model. In fact, at 1040 μs KH stripped parcels are visible for both the numerical results at the very tip of the plumes beyond the dense cluster of parcels. On the other hand the evolution of the experimental liquid plume profile over time appears to be much smoother implying that a more accurate numerical integration of the atomization and secondary breakup phenomena must be achieved to better reproduce the injection process.

4.2.2 Effects of Decreasing Ambient Temperature

In this part of the chapter results for the cases reported in Tab.4.4 are discussed by focusing on the effects due to the reduction of the ambient temperature.

Table 4.4: *Bespoke simulated cases: operating properties*

Case	p_{inj} **[bar]**	ρ_{amb} $\left[\frac{kg}{m^3}\right]$	T_{amb} **[K]**
Case 4	200	3.5	473.15
Case 5	200	3.5	473.15
Case 6	200	3.5	373.15
Case 7	200	3.5	333.15

According to multi-hole GDI sprays literature data [80] a reduction of the ambient temperature should increase the spray penetration with however more relevant effects on the liquid rather than the vapor phase. At first, to investigate the behavior of the two adopted secondary breakup models Case 1 (now named Case 4, Reitz-KHRT) and Case 2 (now named Case 5, Reitz-Diwakar) were tested under an ambient temperature of 473.15 K. As Fig.4.7 reports, while both cases displayed the expected increase of liquid and vapor penetrations Reitz-Diwakar appeared to better react to the decrease of ambient temperature showing a more accurate fit of the experimental curves. On the other hand, the Reitz-KHRT computation was characterized by a lower liquid penetration with thus a higher gap between liquid and vapor which appears to be due to an overestimated secondary breakup phase and thus higher evaporation rate. As the main target of this preliminary analysis was to investigate a numerical approach which could minimize the requested recalibration activity from case to case the Reitz-Diwakar model was chosen as reference for the simulations up to Case 12.

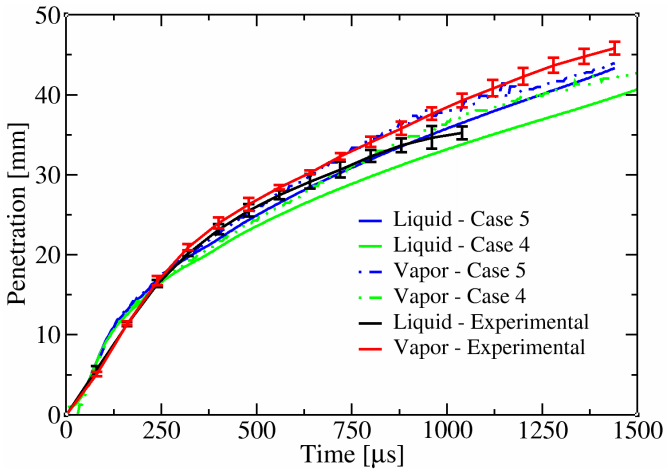

Figure 4.7: *Computed spray penetration, Case 4 (Reitz-KHRT) against Case 5 (Retiz-Diwakar) [76]*

Within this context Fig.4.8(a), Fig.4.8(b) and Fig.4.8(c) show that the combination of Huh-Gosman and Reitz-Diwakar models managed to provide acceptable penetration results with an ambient temperature equal to 373.15 K and 333.15 K.

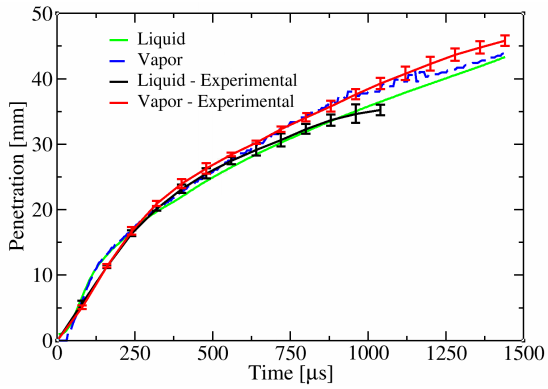

(a) Computed spray penetration, Case 5

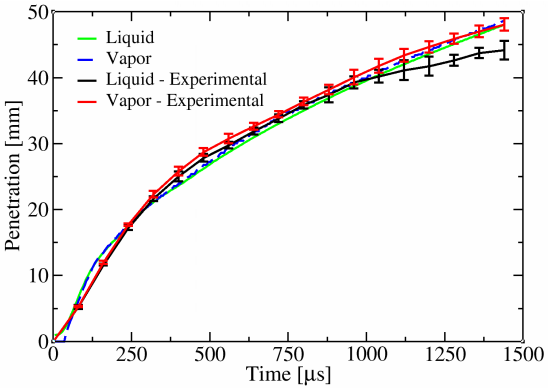

(b) Computed spray penetration, Case 6

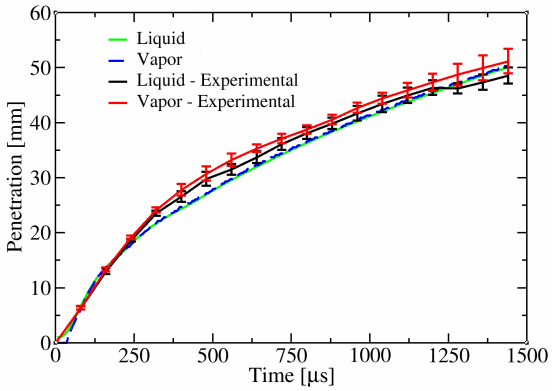

(c) Computed spray penetration, Case 7

Figure 4.8: *Spray penetrations, Case 5, Case 6 and Case 7 [76]*

The adopted computational mesh size for Case 5, Case 6 and Case 7 was equal to 0.5 mm.

4.2.3 Effects of Injection Pressure and Ambient Density

Tab.4.5 reports the details of the operative conditions from 8 to 12.

Table 4.5: *Bespoke simulated cases: operating properties*

Case	p_{inj} [bar]	ρ_{amb} $\left[\frac{kg}{m^3}\right]$	T_{amb} [K]
Case 8	150	3.5	573.15
Case 9	150	3.5	333.15
Case 10	150	1.0	333.15
Case 11	100	1.0	333.15
Case 12	50	1.0	333.15

Fig.4.9(a) and Fig.4.9(b) show the obtained results for Case 8 and Case 9.

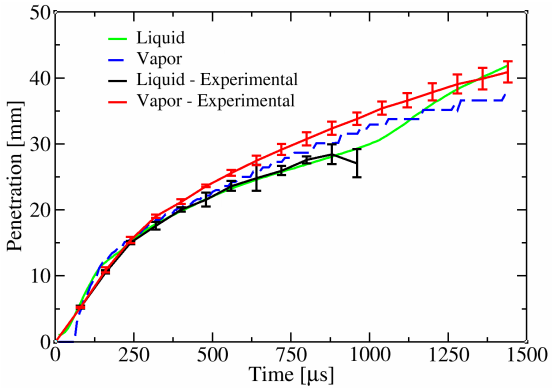

(a) Computed spray penetration, Case 8

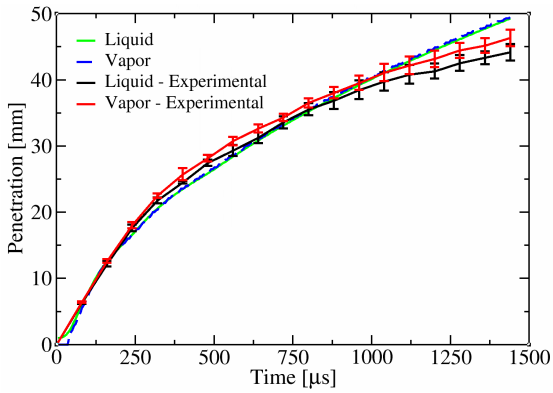

(b) Computed spray penetration, Case 9

Figure 4.9: *Spray penetrations, Case 8 and Case 9 [76]*

The former is characterized by a good prediction of both liquid and vapor curves with the spray that satisfies the mixing limited condition before the EOI threshold. Numerical penetrations of Case 9 fall in the respective experimental ranges of validity

as well but their superimposition across the whole temporal range demonstrates that under an ambient temperature of 333.15 K the spray evaporation rate is considerably reduced. This aspect suggests that this operating condition may represent the upper physical limit for the adopted secondary breakup and that a further reduction of ambient density and/or ambient temperature would require a recalibration of the main submodel constants. Within this context further reductions of both injection pressure and ambient density coupled with the cold conditions required a recalibration of the Reitz-Diwakar secondary breakup model for the cases shown in Fig.4.10(a), Fig.4.10(b) and Fig.4.10(c).

To make computed liquid and vapor penetrations fit the reference experimental range it was thus necessary to decrease the C_{b1} parameter as it is reported in Tab.4.6. While this action apparently yielded good results both in terms of computed spray penetrations and morphology (Fig.4.11(a)-4.11(b), Fig.4.12(a)-4.12(b), Fig.4.13(a)-4.13(b)) it came at the cost of physical soundness. In fact the C_{b1} model constant holds the same weight of the stable Weber gas number of a droplet We_{crit} (~ 6). Its reduction to 0.5 means that the parcels are numerically subjected to secondary breakup even in motion conditions well below the physical Weber gas number regime of droplet stability. This was considered as an unacceptable drawback of the current numerical setup for low evaporating GDI conditions, so further model investigations were carried out and will be proposed in this thesis.

Moreover, the adopted minimum cell size for the latest cases was equal to 1 mm unlike the 0.5 mm value used in previous ones. This is another weak point of the overall setup because grid consistency between the different simulations was not satisfied. On the other hand previous analysis implies that a consistent overprediction of the computed axial liquid penetration would have been achieved with a 0.5 mm grid size with respect to the less evaporating cases.

Table 4.6: *Main adopted Reitz-Diwakar model constants*

Constant	Value
C_{b1} (Cases 5-9)	6
C_{b1} (Cases 10-12)	0.5
C_{s1}	0.5
C_{b2}	1.0
C_{s2}	4.1

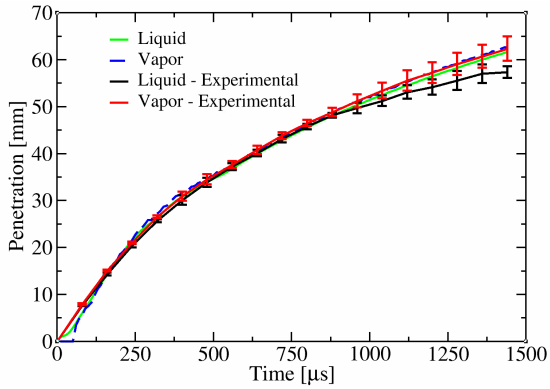

(a) Computed spray penetration, Case 10

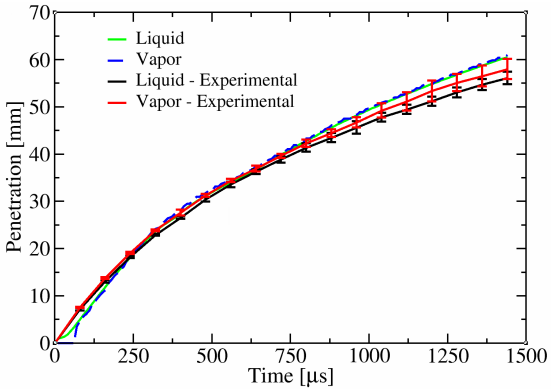

(b) Computed spray penetration, Case 11

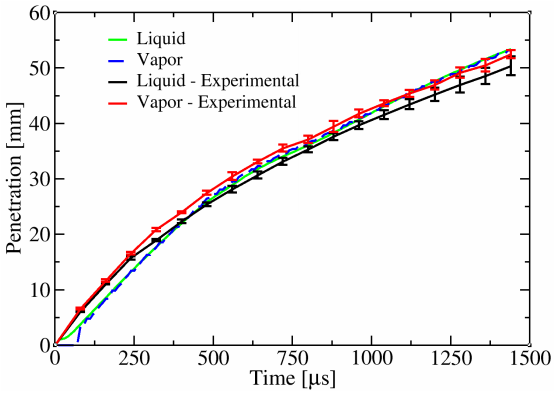

(c) Computed spray penetration, Case 12

Figure 4.10: *Spray penetrations, Case 10, Case 11 and Case 12 [76]*

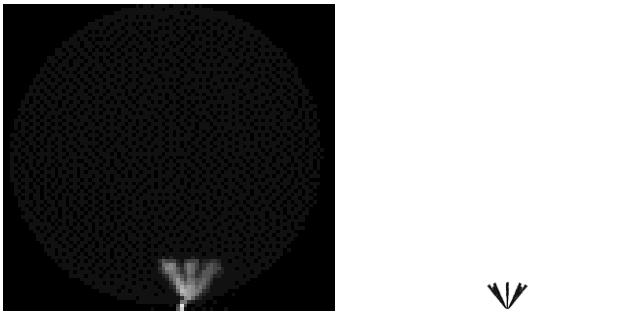

(a) Experimental Mie scattering (b) Computed spray, Case 12

Figure 4.11: *Spray morphology validation, 160 μs [76]*

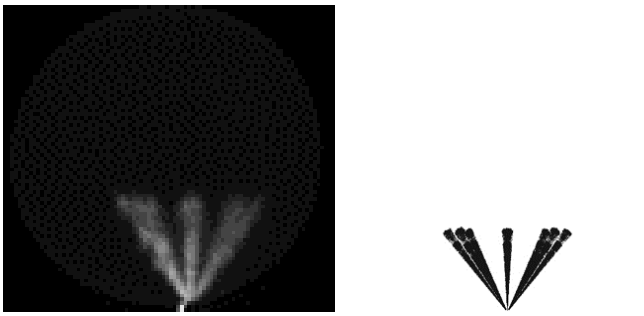

(a) Experimental Mie scattering (b) Computed spray, Case 12

Figure 4.12: *Spray morphology validation, 560 μs [76]*

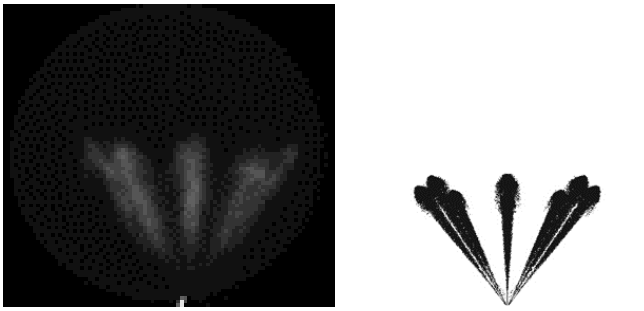

(a) Experimental Mie scattering (b) Computed spray, Case 12

Figure 4.13: *Spray morphology validation, 1040 μs [76]*

Finally Fig.4.14 shows the computed values of SMD for each of the tested cases against experimental data available for a modern GDI injector as a function of the injection pressure [33]. Numerical results are consistent with the experimental range and they reproduce with good accuracy the trend of increasing droplets diameter with the reduction of the injection pressure. This is an important achievement when looking

at the activity of modeling improvement which will be carried out in the upcoming chapters because these results represent a reference target that new numerical spray models will have to meet as well.

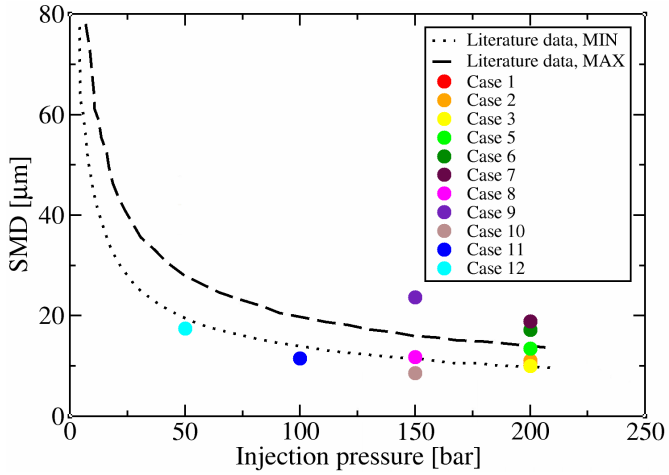

Figure 4.14: *SMD validation [33, 76]*

4.3 Conclusions and Next Steps

The preliminary spray analysis carried out in this chapter allowed to test a baseline GDI numerical setup under a wide range of operating conditions and for the complex ECN Spray G injector geometry. It was an important step which allowed to understand weak points and strengths of the available spray models.

More in detail, the most relevant positive aspects consisted into the fact that the average SMD value matched the available experimental data for each tested case. Moreover, the computed spray penetrations were comparable to the experiments for the different operating points. On the other hand the weak points of the setup can be referred to:

- the prediction of the spray PCA. As it was shown, the experimental plume cone angle value is considerably greater than the value which was adopted for the proposed simulations. Calculations proved to be very sensitive with respect to the PCA value both in terms of spray axial penetration and centerline gas velocity. A further step is thus needed towards an increase of the plume cone angle while still providing good results in terms of penetration and entrainment;
- the dependency between the atomization Huh-Gosman model and the predicted

plume cone angle. The Huh-Gosman model requires the calibration of a wide set of parameters, thus representing an approach which goes against the desired theoretical simplification of the numerical spray setup. Moreover, to increase the computed PCA value of the Spray G a further recalibration of the main model constants would be necessary with values considerably different from those in literature;

- the computed centerline velocity. Compared to the available RANS numerical benchmark a better prediction of the negative recirculation zone of the centerline velocity was achieved at the cost of an underpredicted positive peak. This aspect would lead to think that an increase in secondary breakup intensity is required;

- the mesh cell size. It was in fact not possible to achieve a grid size consistency between the different cases. Low evaporating conditions required a minimum cell size of 1 mm against the 0.5 mm for cases such as the G1 otherwise the numerical liquid penetration would have been considerably overestimated. A reliable setup should provide consistent results under the same mesh specifications. For this reason, from this point of the research onwards only the 0.5 mm cell size grid was considered for in-vessel Spray G investigations;

- the KH stripping activity of the Reitz-KHRT model and its effect on the spray morphology. It was indeed observed that the stripped mass from the parent parcel was numerically computed so that a cluster of parcels would form in each tested case at the tip of the plumes deforming the predicted spray morphology as a consequence;

- the Reitz-Diwakar breakup efficiency under low evaporating conditions. With low value of injection pressure and ambient density it was necessary to reduce the C_{b1} parameter of the model well below the value of 6 which represents the Weber gas number physical threshold for a stable droplet motion regime.

CHAPTER 5

Improved Spray Numerical Setup: ECN6 Workshop and Engine Validation

In this chapter the overall numerical approach has been considerably rethought with the aim to address the weak points which were previously exposed. Moreover, the new static vessel Spray G simulations were carried out within the context of the latest ECN6 Workshop for which novel experimental data and PLV-based post-processing methodologies were considered. These new references will represent the benchmark from this section of the work onwards allowing to better investigate the main spray phenomena and to considerably improve the accuracy of the numerical results. Within this context the flash boiling Spray G2 operating point was considered as well thus requiring a dedicated evaporation model which was specifically implemented into the LibICE numerical framework. Finally, the numerical injection setup was also applied to full-cycle simulations of the Darmstadt optical access engine with results validation carried out in terms liquid impingement, wall-film formation, air-fuel mixing and combustion.

The organization of the chapter is as follows:

- in the first section the new implemented flash boiling evaporation model is introduced and described accordingly;
- in the second sectio, the overall ECN6 numerical approach is presented and the main Spray G results are discussed;
- in the third section the proposed set of spray sub-models is validated under real engine conditions by means of full-cycle simulations of the IFP Energies Nouvelles (IFPEN) optical-access GDI engine.

The set of post-processed quantities and fields are defined according to Section 2.1.2.

5.1 The Adachi-Rutland Flash Boiling Evaporation Model

It is known [79] that in internal combustion engines flash boiling is a phenomenon which occurs when the liquid fuel is characterized by a saturation pressure greater than that of the surrounding ambient gas [65]. Under this condition the liquid fuel enters a metastable state with a high degree of superheat thermal energy [11, 125]. On this basis it is clear that in SI engines flash boiling can occur under low loads operating conditions when the liquid fuel is injected during the intake phase (when the in-cylinder pressure is at its minimum value) with the aim to promote a homogeneous air-fuel mixing process. Flash boiling is also associated with fast timescales and has great influence on spray formation and evolution because of bubble nucleation and intense atomization [20] leading to strong spray collapse. It was also verified in literature that the spray PCA value is considerably influenced by flash boiling especially near the nozzle where the rapid vapor expansion increases the gas entrainment thus widening the liquid plume [92] and promoting spray collapse [82].

It was thus necessary to implement an evaporation model capable to correctly predict the phenomena associated with flash boiling. As such, the specific literature-based Adachi-Rutland approach [125] was considered [79] for this task providing a global drop vaporization rate characterized both by a flash term and by the effects due to external heat transfer. When a droplet separates from a liquid jet sheet in an internal combustion engine it may be characterized by an initial temperature greater than the

corresponding boiling one, leading to fast flash evaporation nearby the droplet surface which is kept at the boiling temperature [125]. This phenomenon generally happens in an engine because of the limited residence time available for the fuel in the initial liquid column which breaks immediately in several droplets after the primary breakup. Furthermore, when the surrounding gas temperature is greater than that of the boiling fuel, energy transferred both from the external gas and the interior of the droplet contributes to surface evaporation [125]. Under high superheat conditions vapor cavitation may be the most dominant contribution, otherwise conduction and convection are the physical phenomena controlling the energy being transferred from the interior of the droplet to its surface.

The flash boiled vaporization rate covering the transfer of energy from the interior of the drop to its surface is the G_f parameter ($\left[\frac{kg}{s}\right]$), which is based on the experimental correlation proposed by Adachi [11] and reported in Eq.5.1. The term A is the droplet surface area, T_p is the droplet temperature, T_b the saturated boiling temperature and $L\left(T_b\right)$ represents the latent heat under boiling conditions.

$$G_f = \frac{\alpha_s \left(T_p - T_b\right) A}{L\left(T_b\right)} \tag{5.1}$$

The term α_s represents the overall heat transfer coefficient from the droplet interior to its surface (unit of measure in $\left[\frac{kJ}{sm^2K}\right]$) which depends on the drop superheat degree and thus on the temperature difference between interior and surface. Different expressions (Eq.5.2-5.4) for this coefficient were experimentally derived by Adachi [11] as a function of the $(T_l - T_b)$ quantity by means of Infrared Extinction/Scattering (IRES) temporal and spatial distribution of the fuel vapor concentration.

$$\alpha_s = 0.76 \left(T_l - T_b\right)^{0.26}, \quad \left(0 \leq \left(T_l - T_b\right) \leq 5\right) \tag{5.2}$$

$$\alpha_s = 0.027 \left(T_l - T_b\right)^{2.33}, \quad \left(5 \leq \left(T_l - T_b\right) \leq 25\right) \tag{5.3}$$

$$\alpha_s = 13.8 \left(T_l - T_b\right)^{0.39}, \quad \left(\left(T_l - T_b\right) \geq 25\right) \tag{5.4}$$

The term T_l stands for the droplet liquid temperature expressed in $[K]$. In GDI engines the characteristic drop vaporization time due to external heat transfer from the

surrounding gas is usually on the same order of magnitude of the flash vaporization time [125]. As such, both processes should be taken into account simultaneously. Wihin this context, the model acts so that first the droplet surface temperature remains equal to the liquid boiling temperature at superheated conditions [125]. As such, the surface mass fraction approaches unity, a condition which under classic Spalding modeling would lead to an infinite value of the mass transfer number and thus to the assumption of immediate evaporation. Then, at superheated conditions the heat transfer from the surrounding gas is used to evaporate the liquid fuel nearby the droplet surface without energy transfer to its interior. Under this assumption the droplet temperature change is decoupled from the gas-liquid heat exchange [125]. Finally, the vapor flow generated from the flash boiling vaporization can counterbalance the heat transfer from the surrounding to the drop thus reducing the amount of transferred energy [125].

Within this context, at the core of the model stand the two following hypothesis:

- the droplet is perfectly spherical;
- the heat transfer process is assumed as static.

The overall mass continuity equation for a single droplet is then derived according to Eq.5.5

$$4\pi r^2 \rho U = G + G_f \tag{5.5}$$

The term U is the fluid velocity, r is the droplet radius while G is the vapor flow rate due to heat transfer, expressed in $\left[\frac{kg}{s}\right]$.

The momentum equation reduces to Eq.5.6 if high order viscous terms are neglected [125] where the term p represents the pressure.

$$p = constant \tag{5.6}$$

As previously mentioned, under the conventional mass-based evaporation approach [19] the vapor mass diffusion rate controls the droplet evaporation. On the other hand, under superheated conditions the vapor mass fraction at the droplet surface is close to unity with the heat transfer process between the droplet and the surrounding gas becoming

the driving force [125]. Only the energy equation Eq.5.7 ([125]) is thus considered with the boundary conditions at the drop surface (r_0) and at the far-field (r_∞) respectively expressed by Eq.5.8 and Eq.5.9.

$$\rho U c_p \frac{dT}{dr} = \frac{1}{r^2}\frac{d}{dr}\left(r^2 k \frac{dT}{dr}\right) \tag{5.7}$$

$$k\frac{dT}{dr} = \frac{GL\left(T_b\right)}{4\pi r_0^2}, \quad T = T_b \tag{5.8}$$

$$k\frac{dT}{dr} = 0, \quad T = T_\infty \tag{5.9}$$

At the drop surface the temperature is kept equal to the boiling temperature because of flash vaporization and then the conducted heat from the surrounding gas is fully employed for the evaporation of the liquid fuel [125]. The terms k and c_p are the gaseous thermal conductivity and specific heat calculated according to the $\frac{1}{3}$ *rule*.

Under these assumptions Eq.5.7 is integrated twice together with the boundary conditions reported by Eq.5.8-5.9 and the continuity equation (Eq.5.5) [125] so that the global vaporization rate due to heat transfer ($\left[\frac{kg}{s}\right]$) is derived and defined according to Eq.5.10.

$$G = 2\pi\frac{k}{c_p}r_0\frac{Nu}{1+\frac{G_f}{G}}\ln\left[1+\left(1+\frac{G_f}{G}\right)\frac{h_\infty - h_b}{L\left(T_b\right)}\right] \tag{5.10}$$

The Nusselt number Nu is introduced to take into account the condition of non-zero relative velocity between liquid drop and surrounding gas which is typical of GDI fuel injection processes.

5.2 The ECN6 Workshop

In this section, the main Spray G results provided for the Gasoline Session of the ECN6 Workshop [55] are introduced and discussed. As the latest main congress of the Engine Combustion Network at the time, the ECN6 Workshop allowed to carry out new investigations on the Spray G injector, allowing for a significant step forward both in the field of experimental comprehension/reproduction of a GDI spray and the capabil-

ity of the numerical sub-models to provide more accurate results. Within this context, the implemented Adachi-Rutland evaporation model and the new PLV-based numerical post-processing methodologies were employed on the Spray G.

At first, an introduction of the overall adopted numerical framework is given, then the main spray results are discussed. Finally, observed weak points and strengths of the approach will be assessed.

5.2.1 The Numerical Framework

In Tab.5.1 are summarized all the main characteristics of the adopted numerical setup. The parcels were injected into the domain with a velocity value function of the *velocity coefficient* C_v, which was set equal to 0.73 according to previous experimental findings [6]. The adopted injection rate profile is the baseline ECN at 200 bar, introduced in Chapter 4 and derived from experimental measurements with a tube method performed at General Motors (GM) [5].

Table 5.1: *Numerical framework*

Mesh	structured 3D with AMR
Minimum cell size	0.5 mm
Turbulence model	Standard k-ε, $C_{1\varepsilon} = 1.5$
Injection model	Lagrangian Huh
Atomization model	Huh-Gosman
Breakup model	Reitz-KHRT
Evaporation model	Mass-based [19]
Flash boiling evaporation model	Adachi-Rutland
Heat transfer	Ranz-Marshall [94, 95]

Concerning the computational grid, the AMR approach was again employed, with a starting cell size of 4 mm. This time, however, the target reference for the spray region was set equal to 0.5 mm for all the simulated cases. This choice allowed for numerical consistency between all conditions and is coherent with the cell size adopted for GDI engines full-cycle simulations. The standard k-ε turbulence model was employed in each case. Moreover, the Pope correction [90] for turbulence was investigated, with a direct comparison under the baseline G1 condition between values equal to 1.44 (reference) and 1.5 for the $C_{1\varepsilon}$ parameter, which affects the transport equation of the turbulence dissipation rate ε. The Huh-Gosman atomization model [39] was kept as a reference mechanism for the primary breakup, with its main parameters reported

in Tab.5.2.

Table 5.2: *Huh-Gosman model constants*

C_3	1.2
C_4	0.5
C_5	1.0

After what was observed in Chapter 4, for these new simulations the atomization process was decoupled from the prediction of the spray plume cone angle. More specifically, the Huh-Gosman model was tasked just to carry out the primary breakup while the PCA was imposed separately. This change allowed to overcome the plume cone angle underestimation typical of existing correlations without stressing on the tuning activity of the atomization model parameters. In fact, as shown in Tab.5.2 significantly different values for the main Huh-Gosman model constants could be adopted, now closer to reference literature data. As a consequence, the numerical prediction of the liquid evolution nearby the injector nozzle improved, leading overall to a better reproduced spray. Moreover, considering the sensitivity of the plume cone angle to different operating conditions and injector geometries, the proposed decoupling strategy could ensure an accurate PCA prediction even in case of adoption of multiple atomization/secondary breakup models configurations. As a result of a sensitivity analys performed on the baseline G1 condition, the plume cone angle was set equal to $16.5°$ and then kept constant for all the other operating points with the exception of the flash boiling G2 case. The value considerably increased if compared to that of the cases of Chapter 4, becoming closer to the suggested experimental evidence [87].

For the secondary breakup phase, the Reitz-KHRT model [19, 96, 108] introduced in Chapter 4 was chosen to ensure the stochastic contribution to the spray due to the child parcels which are stripped under the KH mechanism. The main model parameters are reported in Tab.5.3, were calibrated on the G1 condition and then kept constant for all the other reported operating points.

Table 5.3: *Reitz-KHRT model constants*

B_0	0.61
B_1	28
C_{RT}	0.08

A Ranz-Marshall approach [94, 95] was employed for heat transfer modeling, while a mass-based mechanism [19] was used as an evaporation model for non-flashing conditions. Under flash boling evaporation, the new implemented Adachi-Rutland model was automatically employed instead.

Moreover, in case of flash vaporization the drop diameter can be considerably reduced because of bubble growth and possible cavitation in the liquid sheet [97, 118, 119]. A correlation proposed by Rutland [125] and reported in Eq.5.11 was thus coupled both with the injector and the secondary breakup models so that such physical phenomenon could be taken into account both for the primary liquid core droplets leaving the orifice and the child parcels which are stripped during the KH breakup activity.

$$d_{boiling} = d\left(\frac{p}{p_{atm}}\right)^{c_{boil1}}\left[1-\chi\left(\frac{p_{atm}}{p}\right)^{c_{boil2}}\right] \tag{5.11}$$

The term d is the droplet diameter after the secondary breakup process has taken place, while c_{boil1} and c_{boil2} are model constants respectively equal to 0.27 and 0.135. The term p represents the pressure in the computational cell, p_{atm} is the atmospheric pressure and χ is a superheat degree parameter defined according to Eq.5.12, where I is the internal energy of the liquid parcel, while T_p and $T_{boiling}$ respectively are the parcel temperature and the local boiling temperature.

$$\chi = \frac{I\left(T_p\right) - I\left(T_{boiling}\right)}{L\left(T_{boiling}\right)} \tag{5.12}$$

5.2.2 Numerical Results

In this part of the work the achieved numerical results [55, 79] are described and validated against the latest experimental data from Sandia and University of Melbourne (UoM) and with the latest PLV-based post-processing methodologies introduced in Chapter 2. The list of the investigated ECN cases is reported in Tab.5.4.

Fig.5.1 reports experimental values of axial liquid penetration provided by Sandia and UoM for both PLV thresholds. As it is possible to observe the same experimental technique yields slightly different results between the two institutions probably due to minor differences in the injector temperature setup. In particular, at equal time values

Table 5.4: *Simulated Spray G operating conditions*

Condition	Temperature $[K]$	Density $\left[\frac{kg}{m^3}\right]$
G1	573	3.5
G2	333	0.5
G3	333	1.01
G4	573	7.0
G7	800	9.0

the UoM low threshold axial penetration is comparable to the high threshold from Sandia. UoM results also provide a shorter liquid residence time which is a quantity defined as the temporal value for which the liquid penetration falls back to zero. These aspects show that UoM data seem to describe a slightly more evaporating spray compared to Sandia experiments. This analysis demonstrates the differences which can arise from the application of an experimental DBI technique on equivalent sprays. For this reason it is mandatory to have the support from a numerical investigation in order to further comprehend these aspects.

Experimental results are reported with root-mean-square (RMS) deviations to provide the spread around the average of the measured quantities for each time-step. RMS ranges will be shown in all the reported axial penetration graphs when available.

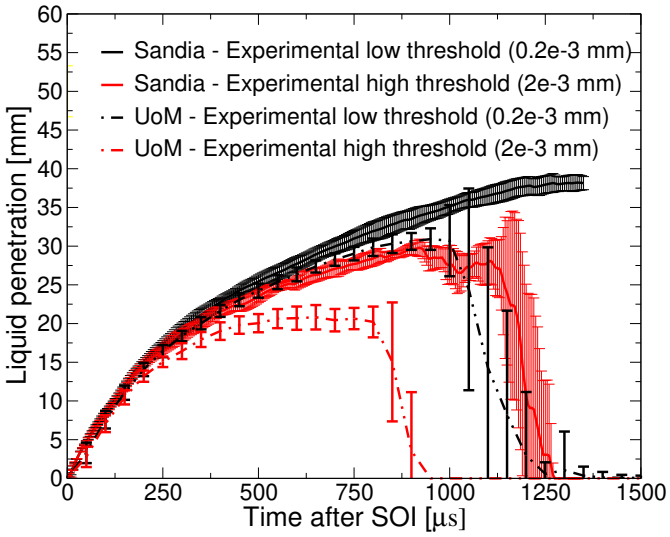

Figure 5.1: *G1 condition, comparison between Sandia and UoM axial liquid penetrations, low and high thresholds [79]*

Fig.5.2 shows the computed liquid penetration against UoM data. For the low

threshold the numerical result matches the experiments up to the EOI which occurs between 750 μs and 800 μs. Afterwards UoM data are characterized by the extinction of the liquid profile, fact which is index of a complete evaporation, while numerical results show that there is still presence of liquid in the computational domain. It can thus be inferred that the computed spray is less evaporating than the experiment. This conclusion is further confirmed by the comparison between the high thresholds profiles which shows how the computed axial liquid penetration is overpredicted for the whole simulation duration.

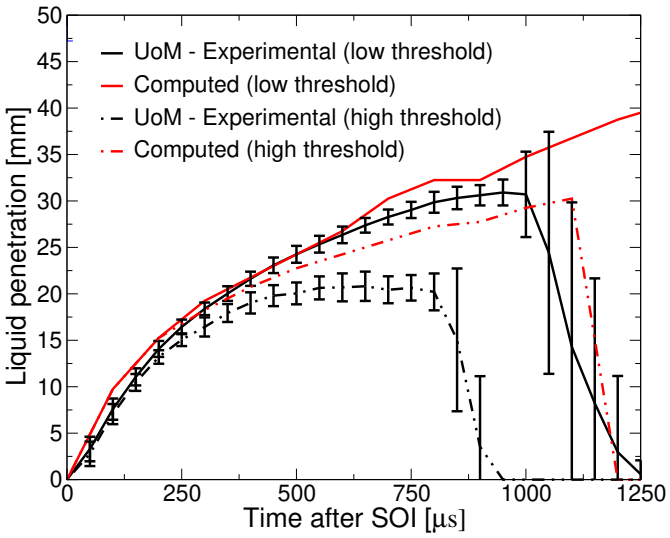

Figure 5.2: *G1 condition, axial liquid penetration, computed results against UoM experimental data, low and high thresholds [79]*

Computed axial liquid penetration was also investigated against experimental data provided by Sandia as it is shown in Fig.5.3, demonstrating a better match and that numerical values always fall within the range of validity of experimental data for each simulation phase (early injection, late injection, post-EOI). Moreover, for the high threshold the predicted liquid residence time of about 1250 μs resulted well in agreement with the experimental findings.

Concerning the axial vapor penetration results are reported in Fig.5.4 against both experimental data of Sandia and UoM. A slightly higher axial vapor penetration was measured by UoM during the injection phase compared to Sandia. This fact, coupled with the great difference between low and high threshold axial liquid penetration values, confirms that the UoM spray seems to evaporate more if compared to the Sandia

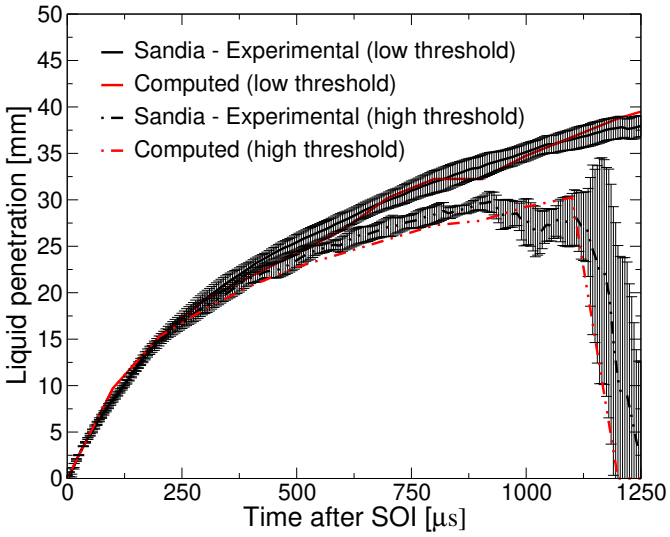

Figure 5.3: *G1 condition, axial liquid penetration, computed results against Sandia experimental data, low and high thresholds [79]*

counterpart. On the other hand, Sandia results exhibit a much smaller gap between low and high threshold axial liquid penetrations with the former almost being superimposed by the vapor curve during the injection phase. Such a behavior seems tp be more coherent with previous experimental and numerical findings and it is closer to the simulated output as well. Turbulence modeling was shown to considerably affect the accuracy of the computed results as it is demonstrated by the comparison of the axial vapor penetration profiles carried out with two different values of the C_1 parameter respectively equal to 1.44 (baseline) and 1.5. The C_1 constant influences the production rate of ε and it thus has an impact on the turbulent viscosity field. In turn, a correct estimation of the turbulent viscosity is fundamental to accurately predict the air-fuel mixing process. The increase of the C_1 parameter was first proposed by Pope [90] and it was proven to improve results accuracy not only for gas jets simulations but also for Lagrangian spray modeling applications both with gasoline and diesel [58] fuels. In the reported case, under the latest spray numerical setup the standard 1.44 value led to a higher liquid evaporation rate both during and after the injection event if compared to what was achieved with C_1 set equal to 1.5. As a consequence, the axial penetration of the spray appeared to be smaller as it is shown in Fig.5.4.

The positive effects due to the application of the Pope correction can also be inferred by the analysis of the centerline axial gas velocity. The comparison between the

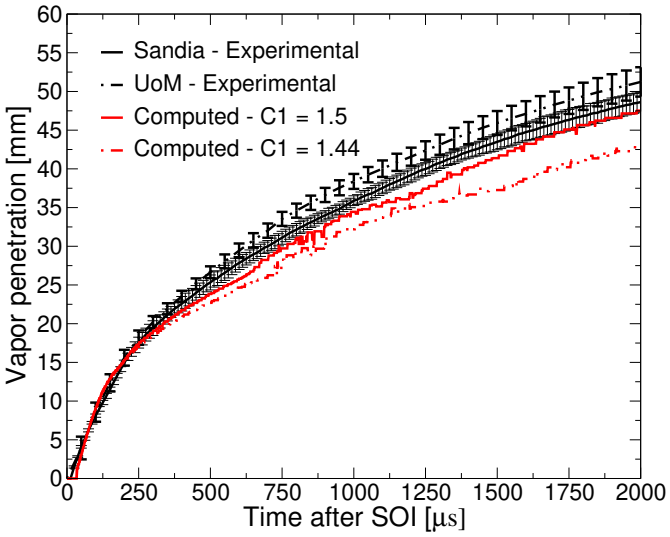

Figure 5.4: *G1 condition, axial vapor penetration, effects of the round-jet correction on the numerical results [79]*

computed profiles and the available experimental data is reported in Fig.5.5.

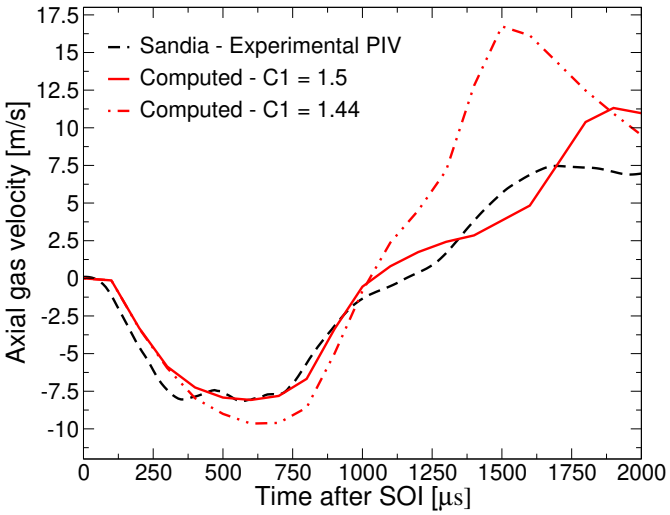

Figure 5.5: *G1 condition, centerline gas velocity profile, effects of the round-jet correction on the numerical results [79]*

Secondary breakup activity and turbulence modeling greatly affect the spray evaporation rate and thus air entrainment. With smaller and more disperse liquid child droplets the evaporation rate is greater and a higher peak of positive velocity is observed after the end of injection. However, the initial negative phase is underpredicted because the drops are too small to provide a good entrainment with air. On the contrary,

by reducing the secondary breakup intensity and by allowing for bigger parcels to be present in the spray plumes a good reproduction of the air entrainment at early time values and nearby the nozzle was achieved. At the same time, the positive peak after the EOI decreases because of a lower spray vaporization rate. It is thus mandatory to keep the numerical setup unchanged to fully evaluate the effects on the gas velocity strictly related to the turbulence modeling. Within this context, the standard C_1 1.44 value allowed for higher liquid evaporation and for a consequent overpediction of the positive velocity peak after the EOI. The observed negative peak of velocity during the upward motion phase (between 500 and 750 μs) was slightly overestimated as well. Instead, with a value of 1.5 a better agreement with experimental data was achieved for the downard motion phase after the the end of injection with the upward motion negative peak of velocity being better predicted as well. Overall, a better matching is achieved between experimental data and numerical results with a C_1 value of 1.5. As a consequence, the Pope turbulence correction was thus applied for all the other simulations reported in this work.

To better investigate the characteristics of the spray morphology an analysis based on experimental PLV maps and axial PLV profiles was carried out for the first time on the Spray G injector. As experimental PLV data from Sandia were not available at the time the analysis was carried out with the set of experimental results provided by UoM. Fig.5.6(a)-5.6(c) report experimental and numerical spray morphologies at time values of 0.3 ms, 0.6 ms and 0.9 ms respectively. The lowest time value stands for an early phase of the injection process and it allows to assess the liquid core morphology near the injector nozzle. At 0.6 ms the latest phase of the injection event is shown with the aim to evaluate the behavior of the secondary breakup model by investigating the droplets distribution at the tip of the spray plumes. Finaly, the 0.9 ms time stands for a condition beyond the EOI and it allows to observe how much liquid mass is left in the computational domain.

Numerical results seem to slightly underpredict the liquid evaporation rate if compared to UoM experiments. In this regard, the analysis of the PLV maps further confirms what was previously observed for the axial liquid penetration thresholds. Indeed, Fig.5.6(a) shows how the UoM spray is characterized by a considerably lower level of

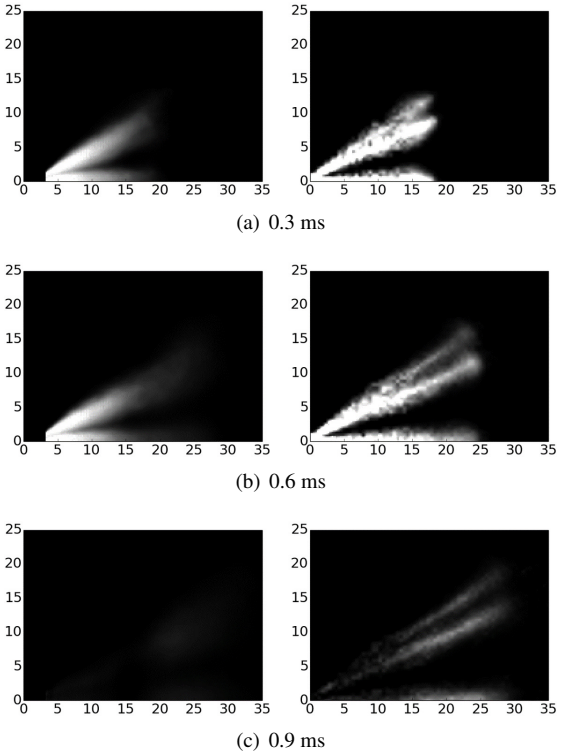

(a) 0.3 ms

(b) 0.6 ms

(c) 0.9 ms

Figure 5.6: *G1 condition, PLV maps comparison between UoM experimental results and computed spray. Range is* $0 - 0.01 \frac{mm^3}{mm^2}$ *[79]*

liquid mass at the plumes tip while Fig.5.6(b) demonstrates that the liquid at the tip almost completely evaporates even before the EOI is reached. Then, Fig.5.6(c) shows that the experimental spray is completely vaporized while the computational result is still characterized by an albeit small presence of liquid in the domain.

Axial PLV profiles evaluated at 0.3 ms (Fig.5.7(a)), 0.6 ms (Fig.5.7(b)) and 1.2 ms (Fig.5.7(c)) demonstrate once more that the computed spray is slightly richer in liquid mass compared to UoM experiments.

Both the 0.3 ms and 0.6 ms times show that the computed profile decreases to zero at an axial position close to that of the experimental data thus demonstrating a comparable extinction length. Still, there is presence of more liquid in the computed spray for the whole plume length. At 1.2 ms the spray almost completely evaporated and the computed profile matches the experiments.

In general, the PLV-based analysis allowed to understand that despite the clear improvements in the prediction of axial spray penetration and air entrainment the proposed

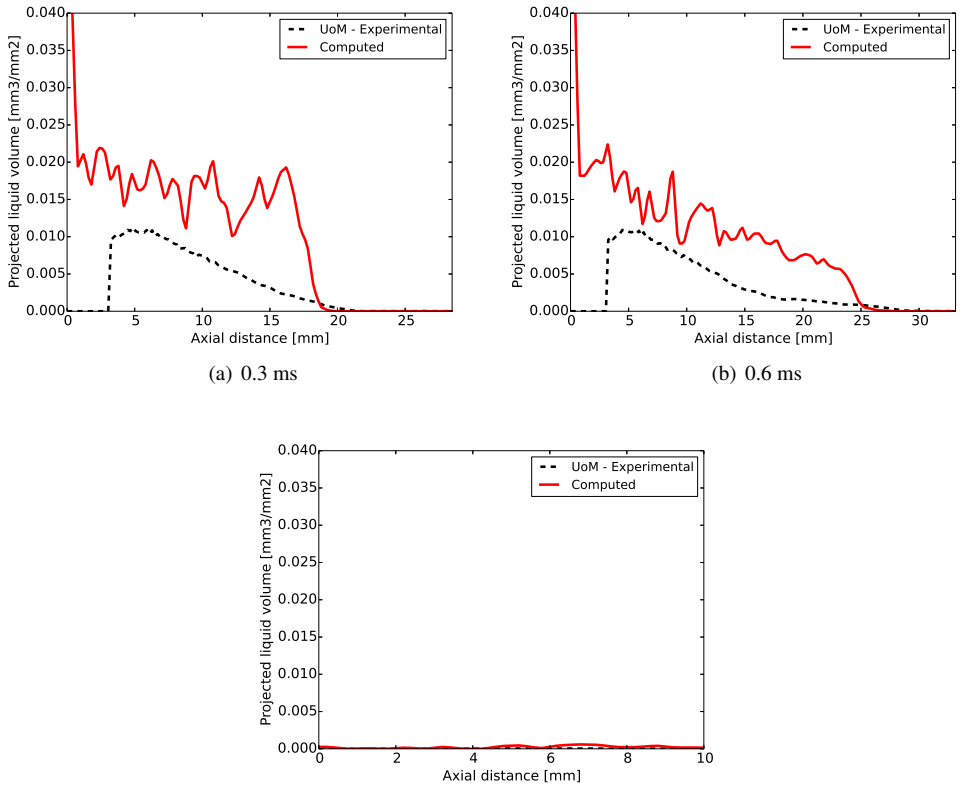

(a) 0.3 ms

(b) 0.6 ms

(c) 1.2 ms

Figure 5.7: *G1 condition, axial PLV profiles, comparison between UoM experimental results and computed spray [79]*

numerical setup still needs further optimization to ensure a more accurate reproduction of the jet morphology. In particular, the tendency of the Reitz-KHRT breakup model to generate a dense "cluster" of liquid parcel during the execution of the KH mechanism was observed at first for the cases of Chapter 4 and was confirmed as well by these simulations. However, the novel investigation based on the projected liquid value Eulerian field helped in better studying the interaction mechanisms taking place between numerical atomization and secondary breakup thus providing fundamental hints towards the modifications which will be introduced in the upcoming chapters.

To further investigate the effects of the spray sub-models in terms of breakup and evaporation numerical liquid and vapor velocities were compared to PDI data provided by GM for the liquid phase [25]. Results were sampled at an axial distance of 15 mm from the injector nozzle and on a radial length of 10 mm by crossing one of the spray plumes as it is shown in Fig.5.8.

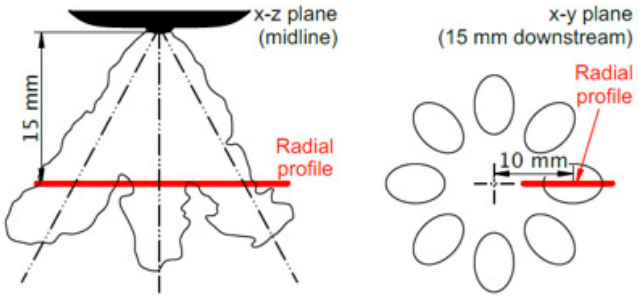

Figure 5.8: *Coordinates for PDI data sampling [25, 79]*

Three reference time values of 0.3 ms (Fig.5.9(a)), 0.6 ms (Fig.5.9(b)) and 1.2 ms (Fig.5.9(c)) were considered for the investigation.

At 0.3 ms the numerical trend is similar to the experimental profile with the computed peak being however slghtly overpredicted. No liquid velocity seems also to be found at a radial distance smaller than 7 mm, fact which might be due to the smaller computed spray plume cone angle. Moreover, simulations were performed with a drill angle of 34 degrees which corresponds to a plume center of around 10 mm for this analysis. On the other hand, the experimental plume center seems to be shifted more towards the 11 mm mark with thus a drill angle which appears to be closer to the 37 degrees nominal value [4]. At 0.6 ms the overestimation of liquid droplets velocity further increases with both computed and experimental spray plumes having their centers at around 10 mm. The experimental plume center thus shifted during the injection phase reducing the spray drill angle and moving the plume closer to the injector axis. This fact does not happen for the computed spray for which the plume center position remains constant up to 0.6 ms probably because of the longer computed liquid core, where the droplets are less influenced by the interacting aerodynamic forces because of their higher diameter and mass. At 1.2 ms a slight underestimation of the computed liquid velocity can be observed. However, the decrease of the relative liquid-gas velocity is captured in the 0.6-1.2 ms time interval by the model.

Experimental PDI data also allowed to validate the SMD at time values of 0.6 ms and 1.2 ms as it is shown in Fig.5.10(a)-5.10(b). At 0.6 ms a good agreement is reached with the experimental profile while underestimated numerical values are observed afterwards due to an overprediction of the KH secondary breakup stripping activity of

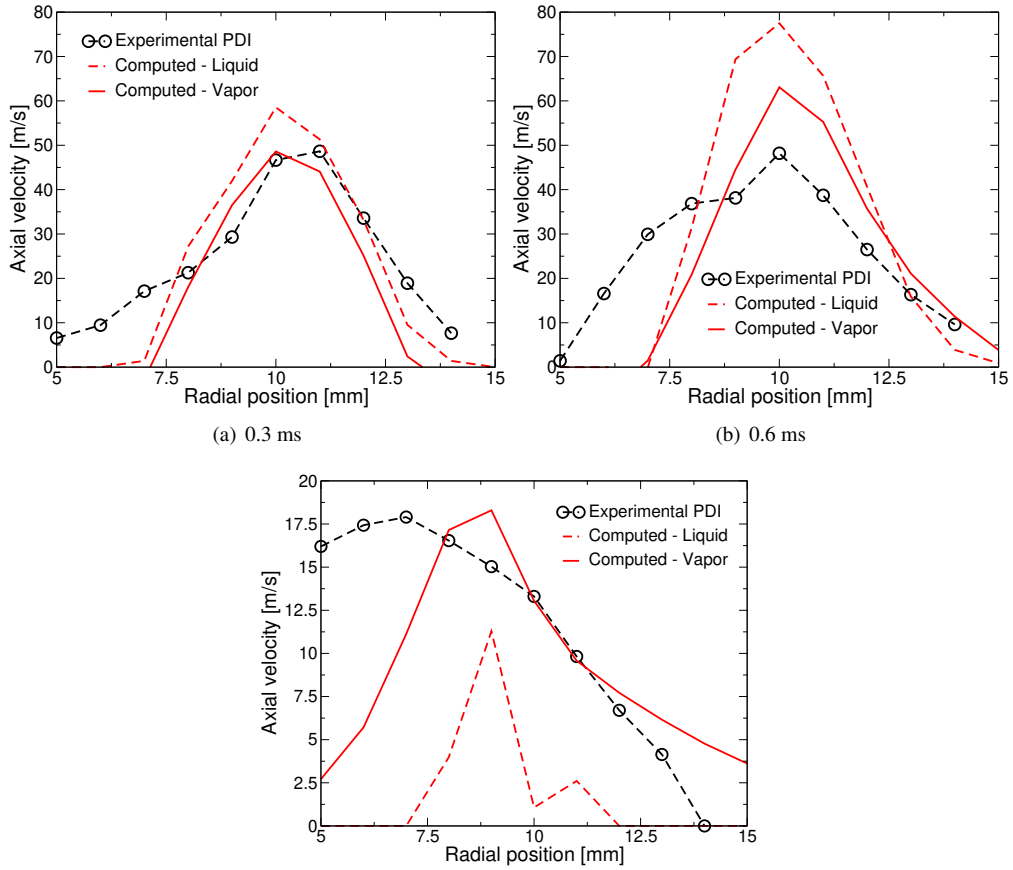

(a) 0.3 ms

(b) 0.6 ms

(c) 1.2 ms

Figure 5.9: *G1 condition, radial PDI velocity profiles, comparison between GM experimental results and computed data [79]*

the child parcels at the plumes tip. Finally, Fig.5.11 reports a validation based on radial distribution of fuel mass over volume at 0.6 ms and at an axial distance of 2 mm from the injector nozzle. This investigation allows to evaluate the effects due to atomization nearby the injector nozzle. The computed trend is consistent with the experimental data and the peak of fuel density is correctly predicted by the adopted spray sub-models. Its location however slightly differs from the experiments because of the smaller drill angle.

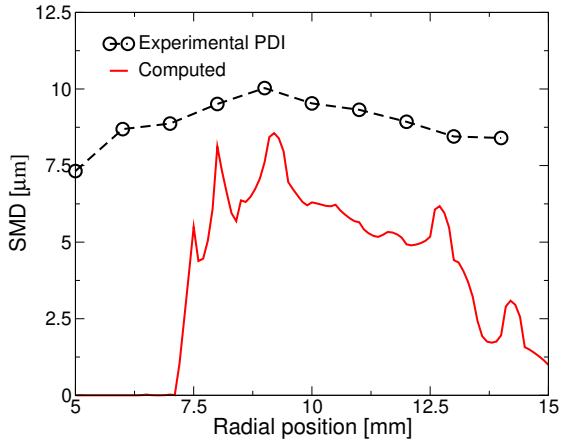

(a) 0.6 ms

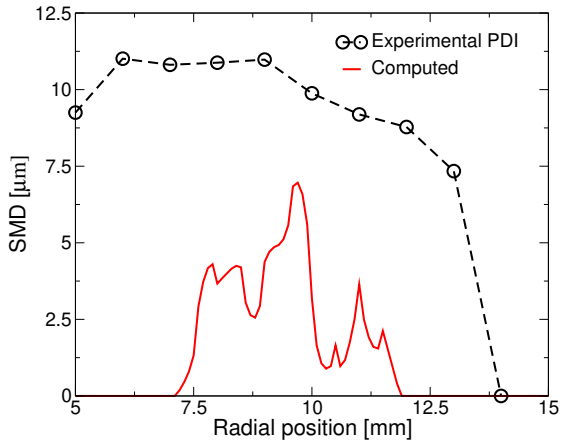

(b) 1.2 ms

Figure 5.10: *G1 condition, radial PDI SMD profiles, comparison between GM experimental results and computed data [79]*

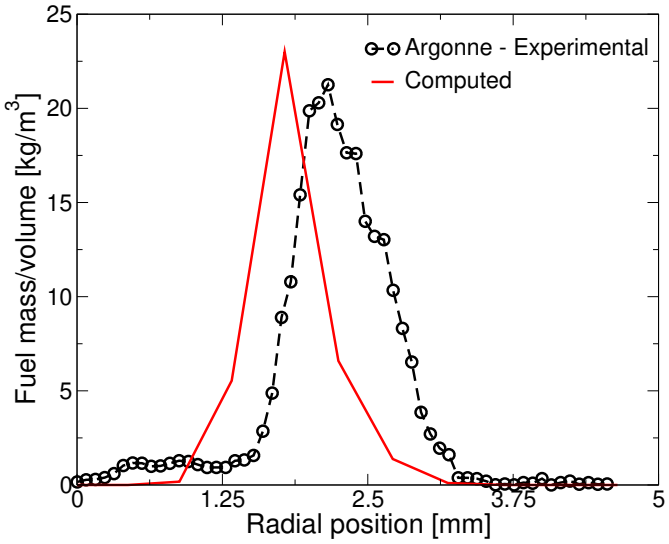

Figure 5.11: *G1 condition, validation of radial distribution of fuel mass over volume at 0.6 ms and 2 mm axially downstream of the injector nozzle. Experimental data from ANL by means of x-ray investigation [79]*

Concerning the Spray G2 flash boiling operating condition the numerical spray PCA was increased to 27 degrees to take into account the effects due to flash vaporization [92] on the basis of a sensitivity analysis. Achieved results were once more validated in terms of axial liquid and vapor penetrations, PLV maps and axial PLV profiles evolution over time against UoM experiments. Fig.5.12 shows the analysis of the axial liquid penetration both for low and high liquid thresholds.

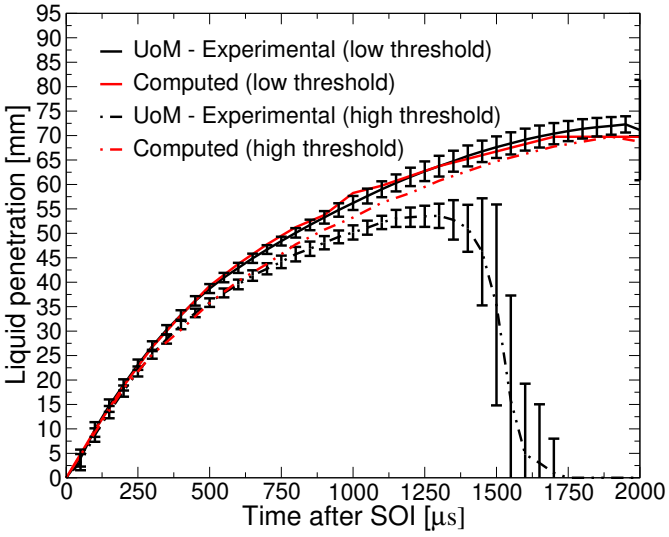

Figure 5.12: *G2 condition, axial liquid penetration, comparison between computed results and experimental data from UoM for both thresholds [79]*

Concerning the former, the computed trend matches the experimental data both during the injection phase and after the EOI. On the other hand the high threshold result slightly overpredicts the experimental range beyond 750 μs, fact which is index of the presence of more residual liquid in the computational domain. Globally, the adopted breakup approach coupled with the Adachi-Rutland evaporation model and the Rutland flashing diameter reduction rate provided an adequate prediction of the spray behavior under flash vaporization. Still, the slightly underpredicted axial vapor penetration reported in Fig.5.13 suggest that there is room for further improvements in terms of secondary breakup and PCA prediction.

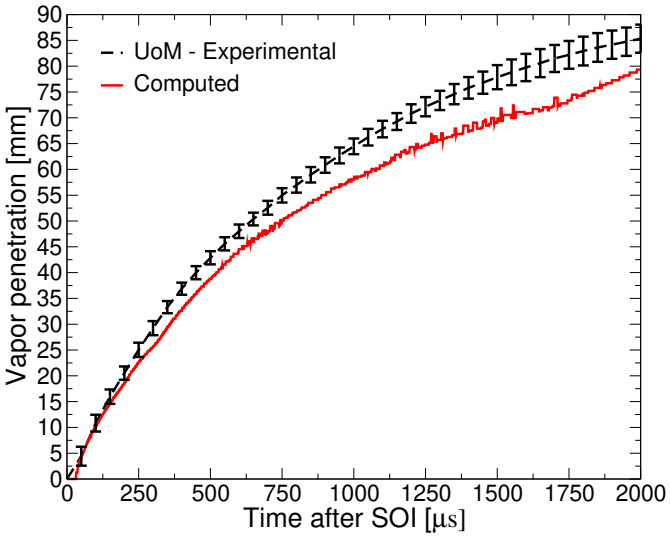

Figure 5.13: *G2 condition, axial vapor penetration, UoM experimental data against computed results [79]*

Fig.5.14(a)-5.14(c) report the PLV maps comparison at time values of 0.3 ms, 0.6 ms and 0.9 ms. At 0.3 ms the liquid core length of the computed spray matches the experimental result with consistent liquid evaporation at the plume tip. At 0.6 ms the evidence of flash boiling evaporation is highlighted by the strong interaction between the experimental spray plumes which is also well reproduced by the simulation. After the EOI a small residual liquid fuel quantity is visible at the tip of the computed spray plumes. The phenomenon is however of negligible intensity compared to what was shown for the baseline G1 condition. Fig.5.15(a), Fig.5.15(b) and Fig.5.15(c) display the axial in-plume liquid mass evolution and demonstrate as well that a good prediction over time is provided by the model.

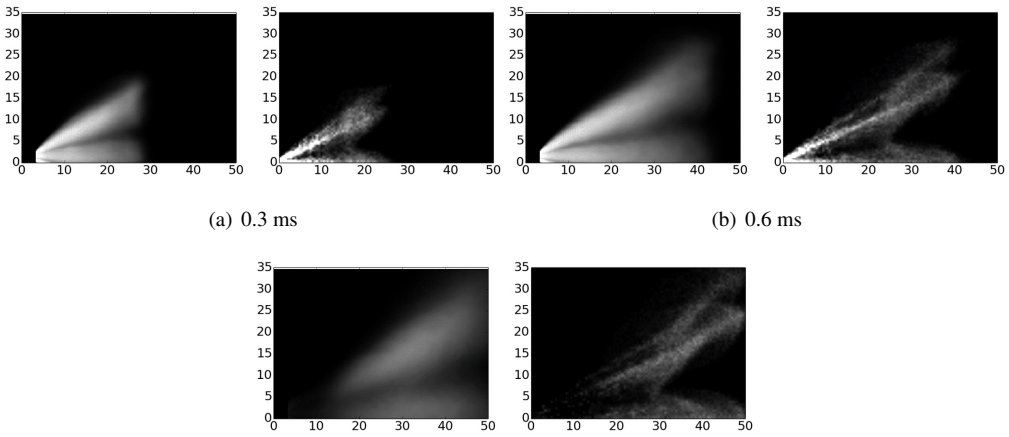

(a) 0.3 ms (b) 0.6 ms

(c) 0.9 ms

Figure 5.14: *G2 condition, PLV maps, comparison between UoM experimental results and computed spray. Range is* $0 - 0.01 \frac{mm^3}{mm^2}$ *[79]*

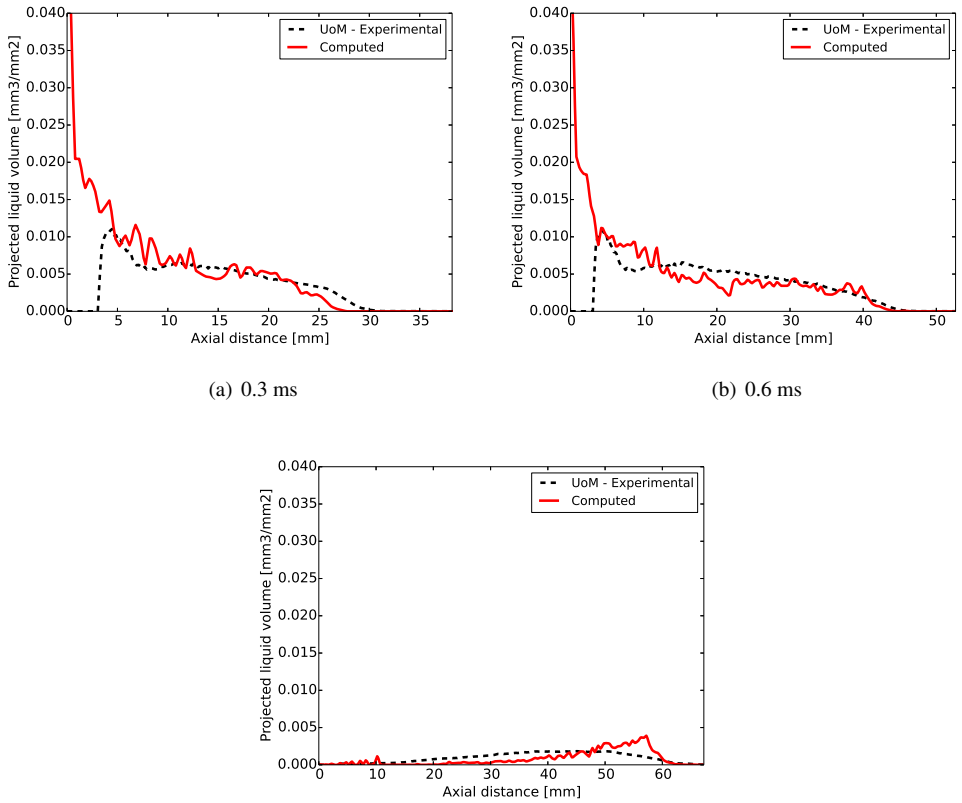

(a) 0.3 ms (b) 0.6 ms

(c) 1.2 ms

Figure 5.15: *G2 condition, axial PLV profiles, comparison between UoM experimental results and computed spray [79]*

The Spray G3 case is typical of a homogeneous GDI engine operating point. Given the low ambient temperature and the lack of flash vaporization the Spray G3 is expected to be the less evaporating case among those discussed in this chapter. Fig.5.16 reports the analysis of the axial liquid penetration both for low and high threshold values. Results show a slight overestimation compared to available experimental data, however the evolution of the trend over time is correctly predicted and the same happen as well for the axial vapor penetration as shown in Fig.5.17. The discrepancy between experimental and computed values may be considered negligible when taking into account that the numerical setup was that of the far more evaporating baseline G1 condition. In fact, when facing a reduction of more than three times of the ambient density a recalibration of the secondary breakup model parameters is usually considered as a necessary action for providing good results. Within this context, the reported computations further demonstrate the capability of the proposed numerical setup to predict with satisfactory accuracy the spray penetration of considerably different GDI operating conditions without the need of main model constants recalibration.

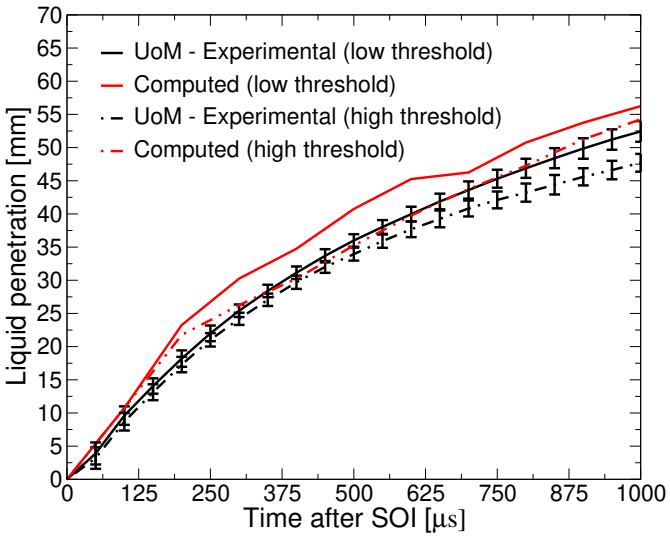

Figure 5.16: *G3 condition, axial liquid penetration, comparison between computed results and experimental data from UoM for both thresholds [79]*

In literature experimentally derived correlations are available for the plume cone angle estimation which allow it to be a function of liquid fuel and ambient gas properties [19, 108]. It was however verified by the most recent ECN numerical spray contributions [55] that these correlations provide angle values which are actually underesti-

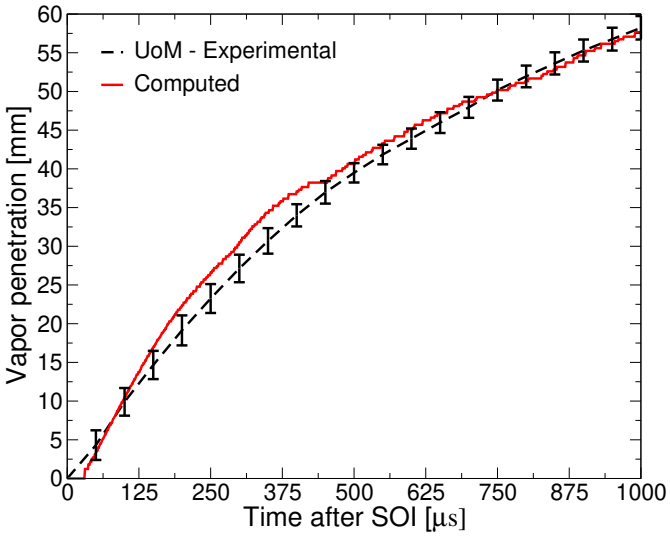

Figure 5.17: *G3 condition, axial vapor penetration, UoM experimental data against computed results [79]*

mated compared to the experimental evidence. In fact, with reference to the current G3 condition a plume cone angle equal to around $9°$ would have been obtained using such correlations. On the other hand the spray morphology investigation based on the PLV maps which is shown in Fig.5.18(a)-5.18(c) demonstrates that the adopted $16.5°$ value is considerably closer to the real PCA displayed by the spray.

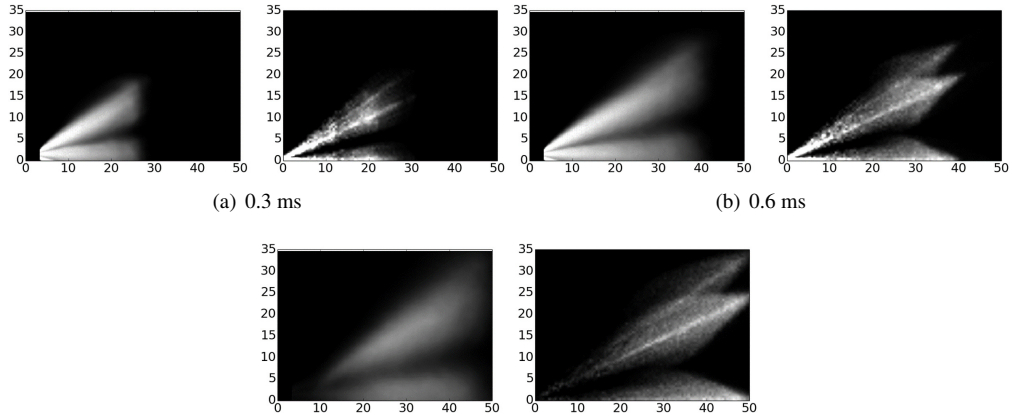

(a) 0.3 ms (b) 0.6 ms

(c) 0.9 ms

Figure 5.18: *G3 condition, PLV maps, comparison between UoM experimental results and computed spray. Range is* $0 - 0.01 \frac{mm^3}{mm^2}$ *[79]*

It will still be mandatory for future research activities to derive correlations which could better predict the interaction between the cone angle value of a multi-hole GDI

spray and its main motion characteristics so that an accurate evolution over time of the PCA could be modeled. This is in fact an important physical aspect which should be taken into account for real engine late injection GDI sprays which may be subjected to a considerable change in ambient conditions while the injection event is taking place. In-nozzle flow field modeling of modern GDI injectors will thus have to be matter of further attention in future works thanks to the support of state of the art experimental data [22, 25, 110].

Fig.5.18(a)-5.18(c)) show that the G3 experimental liquid core further extends throughout each plume length compared to the G1 condition. This is a phenomenon which is due to the lower evaporation rate of the spray.

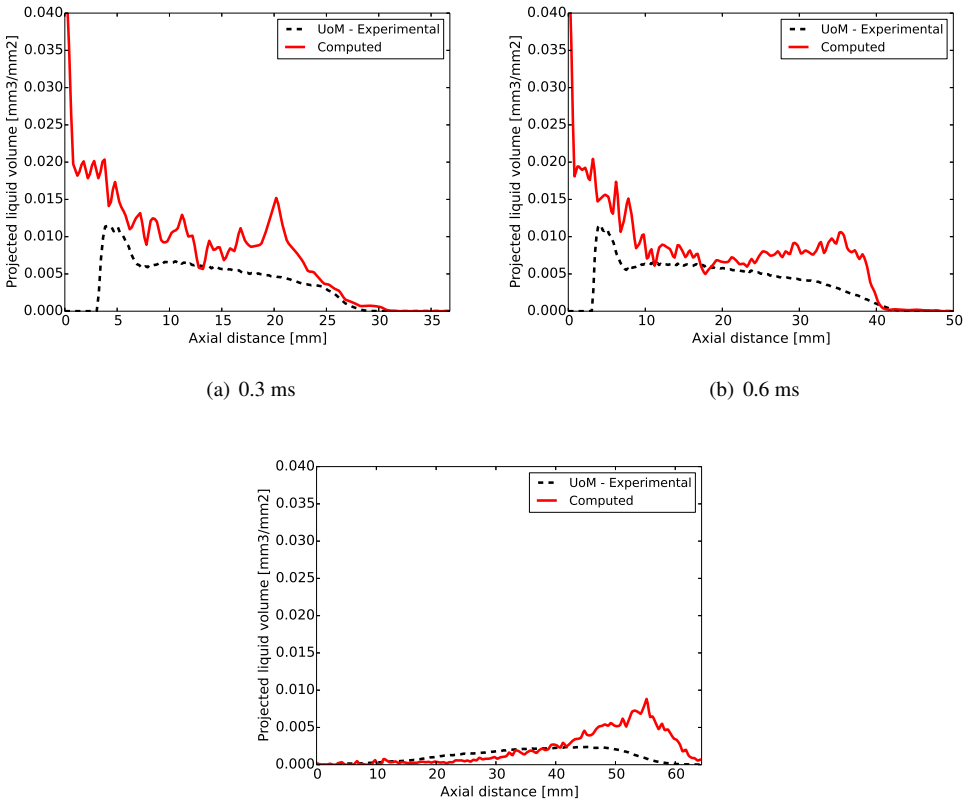

(a) 0.3 ms

(b) 0.6 ms

(c) 1.2 ms

Figure 5.19: *G3 condition, axial PLV profiles, comparison between UoM experimental results and computed spray [79]*

The computed jet morphology is accurate but it is still characterized by a slight overestimation of liquid mass at the tip as it is also demonstrated by Fig.5.19(a)-5.19(c)).

Computed and experimental spray angle values at the injector nozzle were proven to be independent from the differences in ambient pressure, confirming previous literature observations [64].

The G4 condition is subjected to increased drag forces acting on the liquid droplets and to an enhanced vaporization because of a doubled ambient gas density if compared to the baseline G1 operating point. Regarding the G7 case, evaporation is further promoted by an even more increased ambient gas temperature. As a consequence reduced axial liquid penetration values are expected for both cases [80, 85] along with a strong collapse of the spray jets [93, 106].

The low ECN6 threshold axial liquid penetration provided by Sandia was the only relevant experimental measurement available for the validation of the G4 condition. Still, it was suggested that such data could also be used as a reference for investigating the axial vapor penetration given the high evaporation rate of the spray. Fig.5.20 shows that the simulation captured with good accuracy the reduced G4 axial spray penetration which is direct consequence of the increased ambient gas density.

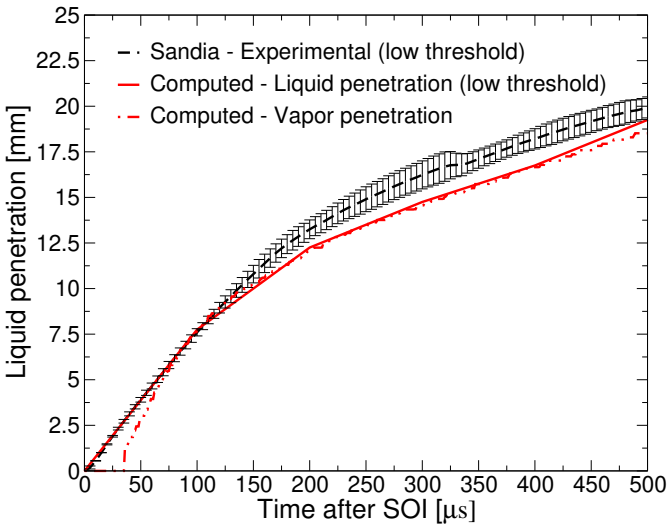

Figure 5.20: *G4 condition, axial liquid and vapor penetrations, comparison between computed results and experimental data from Sandia (low threshold) [79]*

Validation of the axial vapor penetration for the G7 case is shown in Fig.5.21. A good matching was achieved for the whole duration of the injection phase. After the EOI a slight numerical overprediction is observed but the discrepancy should be considered negligible even more so that no RMS range was available from the experiments.

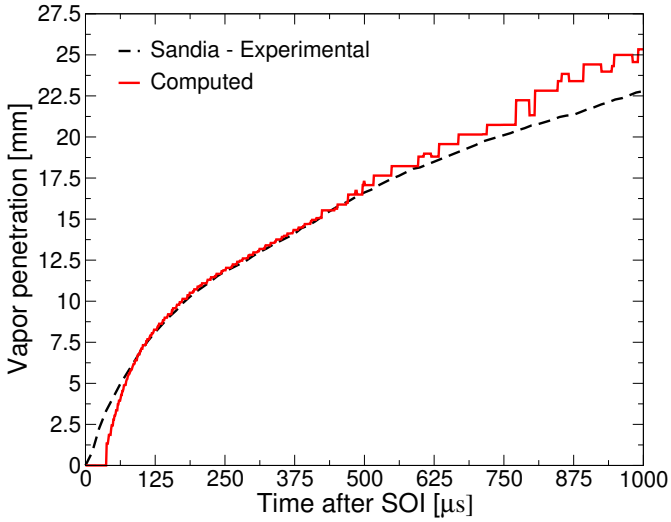

Figure 5.21: *G7 condition, axial vapor penetration, Sandia experimental data against computed results [79]*

Finally a numerical comparison between the PLV maps of the G1 and the G7 cases was performed at 0.3 ms (Fig.5.22(a)), 0.6 ms (Fig.5.22(b)) and 0.9 ms (Fig.5.22(c)). Results confirmed that the adopted numerical setup was capable to reproduce the expected spray collapse of the latter condition.

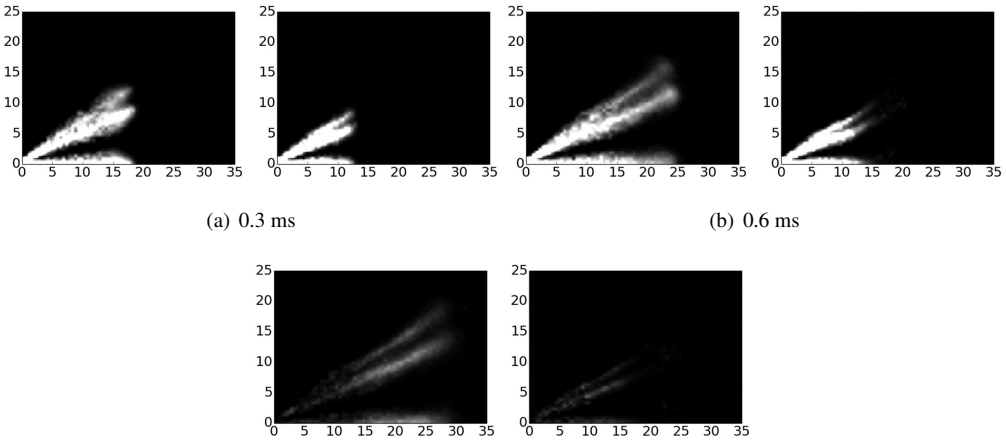

(a) 0.3 ms (b) 0.6 ms

(c) 0.9 ms

Figure 5.22: *PLV maps, comparison between computed G1 (left) and computed G7 (right) sprays. Range is* $0 - 0.01 \frac{mm^3}{mm^2}$ *[79]*

5.3 IFPEN Optical Access GDI Engine Full-Cycle Simulations

The proposed models were also applied to the IFPEN [7] optical access GDI engine in the context of the European UPGRADE research project [9].

5.3.1 The Numerical Framework

For the full-cycle simulations a set of computational grids with full boundary layers at the walls was generated to cover the whole engine cycle. A homogeneous cell size of 0.5 mm was adopted for the cylinder and the combustion chamber during the injection phase for the sake of consistency with the Spray G in-vessel calculations. As it is shown in Fig.5.23(a) a body-fitted mesh is generated for the starting crank angle position. Then, the grid points are moved and the topology is changed with reference to the main engine cycle and geometrical parameters. When the grid quality decays below user-defined thresholds a new grid is generated for the latest piston and valve crank angle positions and the process restarts until the full engine cycle is covered. Such an automatically prescribed motion technique (Fig.5.23(b)) for the grid points [53, 56], based on the solution of the Laplace equation, is available into the LibICE framework and it has been well validated in multiple research activities concerning full-cycle engine simulations [52, 54, 75].

Time-varying total pressure boundary condition profiles, derived from experimental data provided by IFPEN, were adopted for each full-cycle engine simulation. In total, six different profiles were considered both for the intake and the exhaust ports as a function of the specific engine configuration ("high-tumble", "standard" and "swumble") and the specific SOI value. Experiments were carried out with E10 as a fuel while for numerical simulations a conventional gasoline blending was employed. The standard k-ε model was adopted for turbulence with the $C_{1\varepsilon}$ set equal to 1.5 to ensure numerical consistency with the ECN6 Spray G vessel calculations. Coherently, also the spray setup was retained with the same calibration of the ECN6 simulations. Moreover, sub-models dedicated to liquid impingement and wall film formation were specifically employed for the full-cycle calculations. Impingement was modeled with the Bai-Gosman approach [15] by considering the possibility of regimes of *adhesion,*

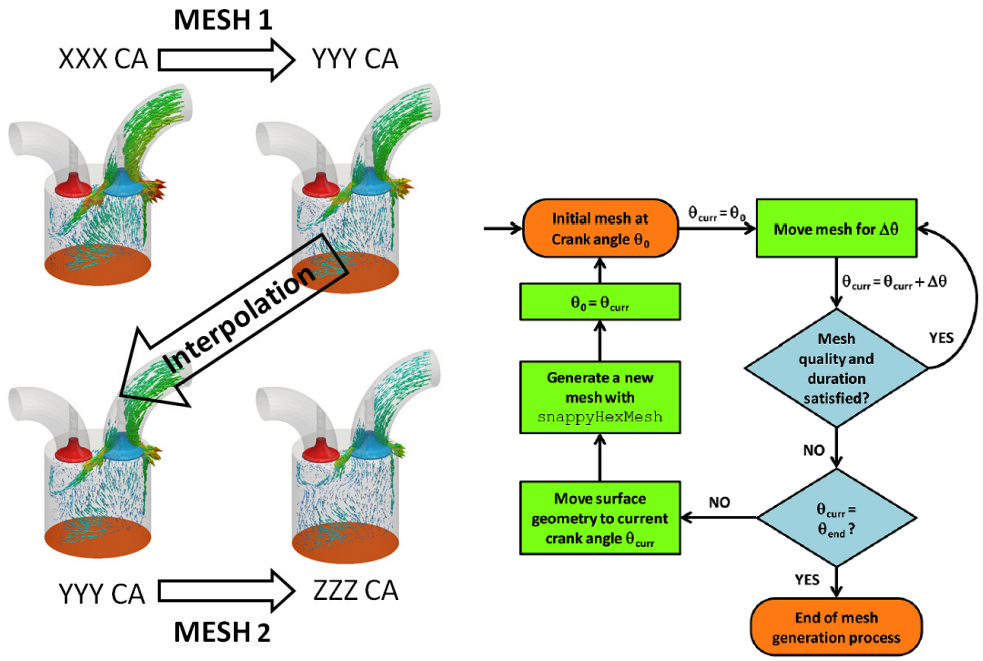

(a) Mesh to mesh mapping

(b) Main mesh generation and motion strategy

Figure 5.23: *Full-cycle mesh generation procedure*

sitck, rebound, spread and *splash* [47] for the interaction between a liquid drop and the engine surfaces. The type of regime depends on two main dimensionless parameters which are the Weber number (*We*, Eq.5.13) and the Laplace number (*La*, Eq.5.14)

$$We = \frac{\rho_l U_n^2 D}{\sigma} \tag{5.13}$$

$$La = \frac{\rho_l \sigma D}{\mu_l^2} \tag{5.14}$$

The term U_n is droplet velocity component normal to the surface. For a dry wall the impingement phenomenon is described by Eq.5.15.

$$Adhesion \Longrightarrow Splash : We_{crit} = 2600 \cdot La^{-0.18} \tag{5.15}$$

In case of a wet surface impingement relations are reported in Eq.5.16.

$$Stick \Longrightarrow Rebound : We_{crit} \approx 1.0 \tag{5.16}$$

$$Rebound \Longrightarrow Spread : We_{crit} \approx 5.0 \tag{5.17}$$

$$Spread \Longrightarrow Splash : We_{crit} = 1320 \cdot La^{-0.18} \tag{5.18}$$

When the *adhesion*, *stick* and *spread* conditions are satisfied the droplet coalesces with the existing film. Under the *rebound* regime the drop bounces back from the wall while losing a small part of its kinetic energy and thus carrying updated velocity components [98]. When the *splash* occurs specific relations allow to determine how much of the splashed liquid mass is retained in the existing wall film [15].

Fig.5.24 reports a schematic representation of the adopted film modeling methodology which consists into a "thin film" approach based on a Finite Area Method that has been extensively validated in previous literature works [54, 63]. Such a convention means that the governing liquid film equations (mass, momentum and energy, with contributions from impingement and film evaporation [50]) are discretized on a curved two-dimensional surface in the three-dimensional computational domain. The solution of the governing equations is carried out by means of a segregated approach [54].

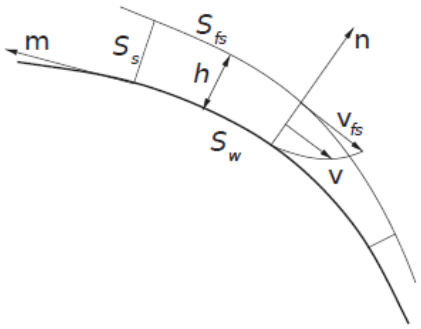

Figure 5.24: *Schematics representation of film modeling [54]*

The term S_w stands for the curved wall surface with normal **n**. The velocity profile of the film **v** varies from zero (at the wall) to the free surface velocity **v_fs** along the film height h. "Thin film" modeling means that the wall film is assumed to be thin enough that the spatial gradients in the surface tangential direction are negligible compared to those in the normal direction. The local liquid pressure p_l within the film is calculated according to Eq.5.19 where p_g is the surrounding gas pressure, p_d is the droplet impact pressure, p_σ the capillary pressure and p_h represents the hydrostatic pressure.

$$p_l = p_g + p_d + p_\sigma + p_h \tag{5.19}$$

The film motion is caused by spatial variation in the tangential directions of the local liquid pressure which is on the other hand assumed to be constant across the film depth.

In particularly complex cases such as those which are reported in this section fuel impingement can also take place on the intake valves because of the temporal superimposition between the engine intake valve lift profile and the injection timing of a top-mounted, multi-hole GDI injector. Within this context, the wall film can be subjected to considerably high velocity gradients due to the air coming from the intake ports. As a consequence if the film moves and reaches the valve edge it can stay attached or separate from the surface. Under the latter condition the film is thus stripped back as discrete liquid droplets into the computational domain as it is shown in Fig.5.25.

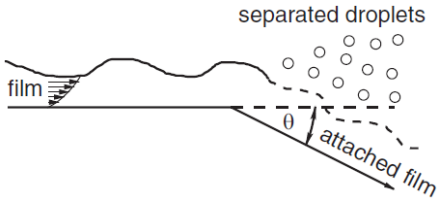

Figure 5.25: *Schematics representation of possible film separation [54]*

The pressure difference between the wall-side and the gas-side of the wall film is the main physical parameter which governs separation and stripping. That is, if the wall-side pressure drops to zero because of high liquid film inertia separation occurs according to a numerical criterion proposed by O'Rourke [89]. Stripping occurs when Eq.5.20 is satisfied where U_F is the liquid film velocity magnitude, ρ_F is the film density and θ is the angle defined in Fig.5.25.

$$3.0\frac{(\rho_F \cdot U_F)^2 \cdot sin\,(\theta)}{1 + cos\,(\theta)} > p_g \tag{5.20}$$

The separated film is thus stripped back again as discrete liquid droplets in the domain with a diameter d calculated according to Eq.5.21.

$$d_{strip} = 1.9 \cdot h \tag{5.21}$$

5.3.2 Results

Two SOI values of 460 CA and 540 CA were simulated for all the three engine intake ports ("standard", "high-tumble" and "swumble"). In this section focus will be particularly put on the comparison between the "swumble" and the "high-tumble" conditions at 460 CA SOI and between "standard" and "swumble" cases at 540 CA SOI. The aim of the activity was to investigate the effects of the different intake charge motions on spray and mixture formation while also taking into account changes due to different ambient conditions and SOI values.

The "high-tumble" operating point with a 460 CA start of injection time represented a complex case by a numerical point of view because of a strict time interaction between the rate of injection profile and the intake valve lift law. In fact, as it is shown in Fig.5.26(a)-5.26(c) the case was characterized by direct fuel impingement on the top surface of one of the two intake valves. As a consequence film formation, evaporation and stripping on a moving surface are physical phenomena that had to be simultaneously reproduced by the numerical setup under an intrinsically unstable motion condition.

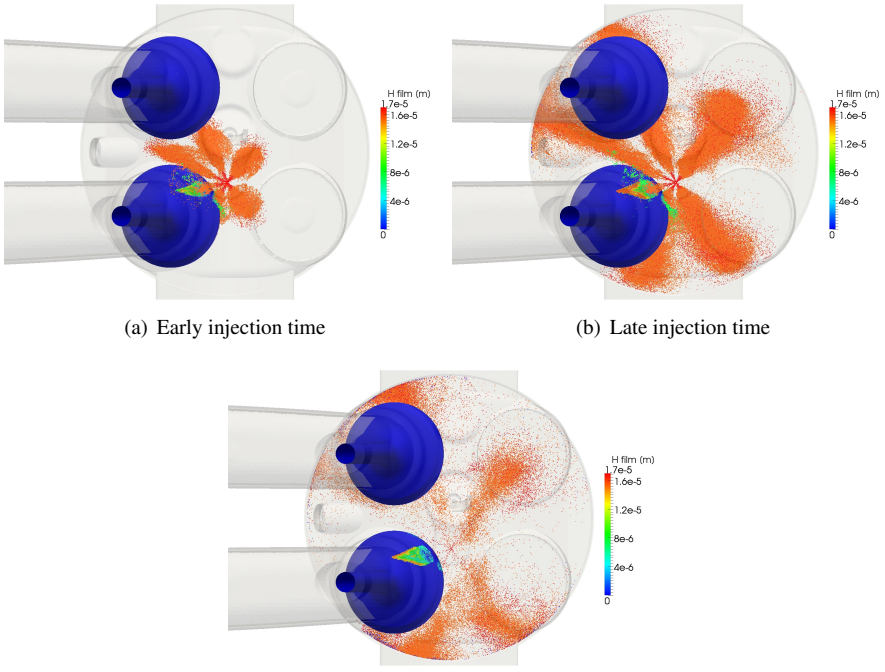

(a) Early injection time

(b) Late injection time

(c) Post EOI time

Figure 5.26: *High-tumble, SOI 460 CA condition, liquid valve impingement and film stripping*

In terms of air charge and in-cylinder motions the "swumble" condition represents an innovative approach employed on the IFPEN optical engine. The intake ports have the same shape of those of the "standard" configuration but one of the two intake valves is kept closed so that all the air mass flow rate is forced into the remaining duct. The aim of this setup is to couple the effects of the classic "tumble" GDI engine flow charge with those of the "swirl" motion [28, 36] which is generally adopted in Diesel engines. Fig.5.27(a)-5.27(c) report a slice of the engine geometry with the intake valves at maximum lift showing the computed velocity magnitude for each engine configuration under a constant scale.

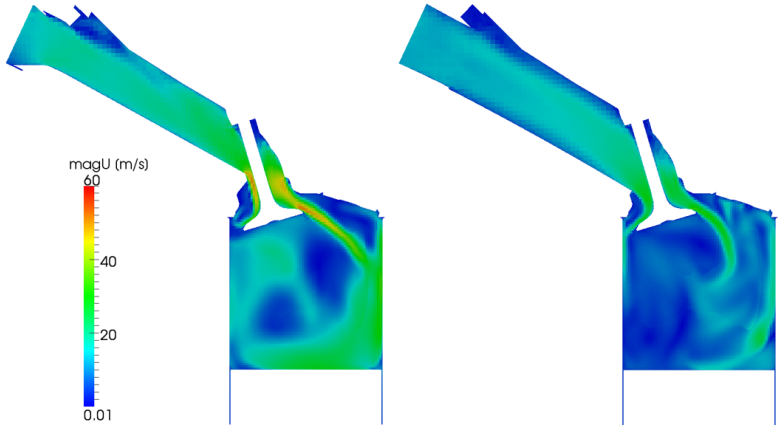

(a) High-tumble (b) Standard tumble

(c) Swumble

Figure 5.27: *IFPEN engine, comparison of the computed velocity magnitude at the maximum intake valve lift*

It is possible to observe that the "high-tumble" configuration is characterized by an in-cylinder motion which is similar to that of the "standard" geometry in terms of struc-

ture but with higher velocity and intensity because of the dedicated intake ports shape. The effects leading to the increased tumble ratio are well visible with a higher velocity magnitude in the valve jets and for the vortex generated nearby the piston. Fig.5.27(c) visually shows the expected motion characteristics for the "swumble" IFPEN engine configuration. The velocity magnitude of the intake valves flow is even higher than that of the "high-tumble" setup as all the mass flow rate is forced into a single duct. This fact, combined with the lack of a motion contribution from the secondary intake port allows to generate the expected in-cylinder hybrid turbulent structure. In this work CFD simulations were performed to assess potential strengths and weak points of such a methodology both against standard and enhanced tumble ports. Fig.5.28(a)-5.28(b), Fig.5.29(a)-5.29(b) and Fig.5.30(a)-5.30(b) report front visual comparisons of the interaction between the injected fuel and the in-cylinder air charge motion for the "swumble" and "high-tumble" SOI 460 CA configurations under selected times, respectively ranging from early injection to post EOI. CA values as comparable as possible between the two cases were chosen for the investigation. The charge motion is visualized by means of streamlines coloured by the gas velocity magnitude.

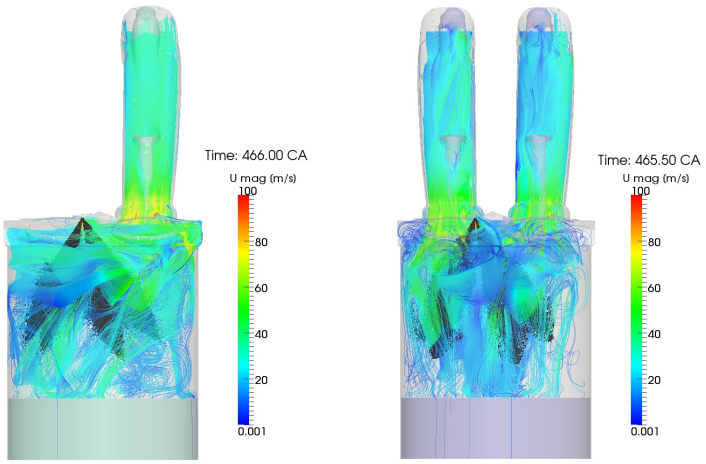

(a) Swumble (b) High-tumble

Figure 5.28: *SOI 460, early injection times*

It is possible to observe that higher velocities at the valve seat are computed for the "swumble" case. Moreover, the streamlines of the "high-tumble" condition appear to

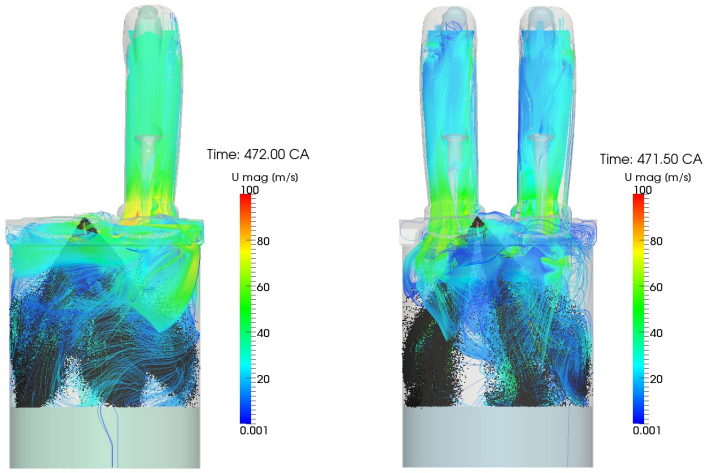

(a) Swumble (b) High-tumble

Figure 5.29: *SOI 460, full injection times*

suggest a stronger interaction between air and fuel with in fact Fig.5.29(b) showing the spray plumes to be more affected by the charge motion nearby the piston surface if compared to Fig.5.29(a). On the other hand, according to the anlysis of Fig.5.30(a)-5.30(b) the "swumble" motion promotes a faster fuel evaporation in the cylinder volume and nearby the engine head while maintaining a more coherent liquid distribution close to the piston, as it is also confirmed by the impinged liquid mass on the piston surface evaluated at 700 CA for all the SOI 460 CA cases and reported in Fig.5.31.

An investigation of the computed *Homogeneity Index* (HI) further confirms these observations. The HI allows for the evaluation of in-cylinder mixture homogeneity and it was calculated according to Eq.5.22 where σ represents the standard deviation of fuel mass fraction and $\sigma_{n,h}$ is the standard deviation under completely inhomogeneous charge conditions.

$$HI = 1 - \frac{\sigma}{\sigma_{n,h}} \tag{5.22}$$

The term $\sigma_{n,h}$ is computed as reported in Eq.5.23

$$\sigma_{n,h} = \frac{\sqrt{\frac{A}{F}}}{(1 + \frac{A}{F})} \tag{5.23}$$

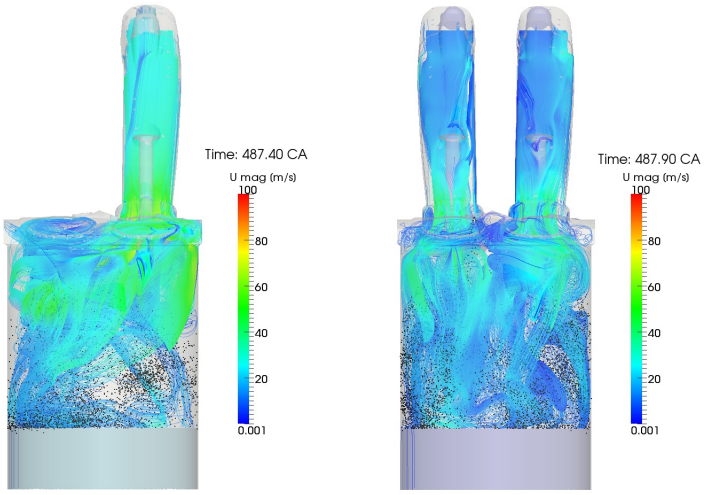

(a) Swumble (b) High-tumble

Figure 5.30: *SOI 460, post EOI*

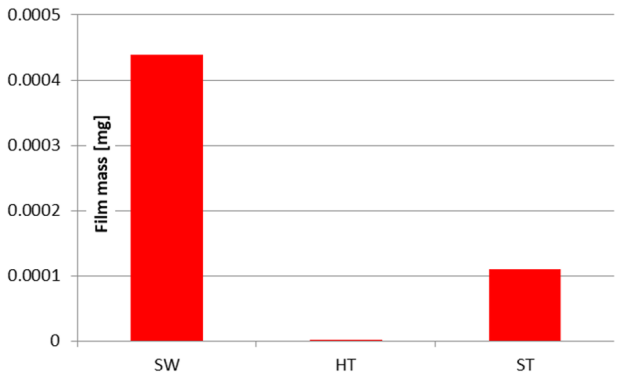

Figure 5.31: *Wall film, impinged fuel mass on the piston surface, SOI 460 CA, 700 CA*

The terms A and F respectively represent the air and fuel mass. The higher is the homogeneity of the mixture the closer to unity is the HI parameter.

Fig.5.32 shows that the in-cylinder mixture of the "high-tumble" case appears as less homogeneous if compared to the "swumble" condition during the whole engine intake phase and also for the majority of the compression stroke. However, at around 700 CA the difference is neglected because of the residual higher in-cylinder charge motion intensity of the "high-tumble" case.

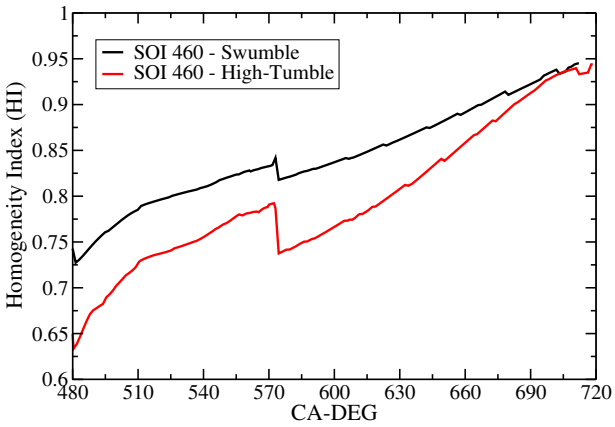

Figure 5.32: *Homogeneity Index (HI), SOI 460 CA, "swumble" and "high-tumble" configurations*

As a consequence, at 700 CA the in-cylinder λ probability function distributions do look similar between the two operating points as it is shown in Fig.5.33(a)-5.33(b).

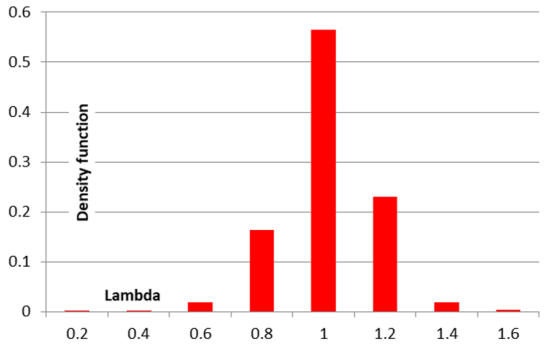

(a) Swumble

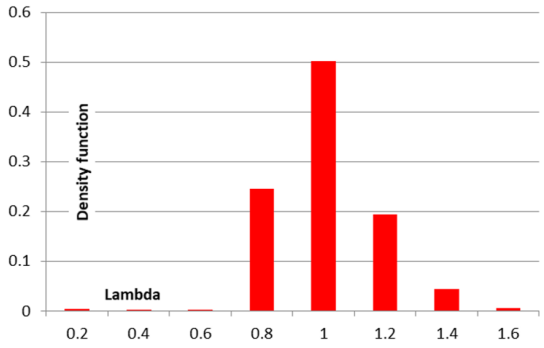

(b) High-tumble

Figure 5.33: *SOI 460, λ distribution, 700 CA*

The λ term is the air-fuel equivalence ratio which is defined according to Eq.5.24

where $\frac{A}{F}$ is the actual air-fuel ratio and $\left(\frac{A}{F}\right)_{Stoich}$ is the air-fuel ratio under stoichiometric conditions.

$$\lambda = \frac{\frac{A}{F}}{\left(\frac{A}{F}\right)_{Stoich}} \tag{5.24}$$

A three-dimensional visualization of the in-cylinder λ field distribution at 700 CA is also reported in Fig.5.34. The "swumble" case displays a lean mixture formation near the spark-plug and the cylinder head surface and rich mixture in the crevices. On the other hand, the "high-tumble" configuration is characterized by an overall mixing level closer to stoichiometric conditions in the chamber with both lean and rich distributions in the crevices.

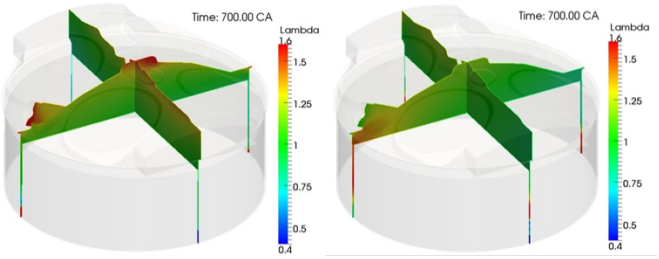

Figure 5.34: *3D in-cylinder λ field distribution at 700 CA, SOI 460 CA, "swumble" case (left) and "high-tumble" case (right)*

Finally, CFD simulations allowed to highlight a not perfectly optimized injection targeting because each SOI 460 CA operating case was characterized by the computed Tumble Ratio (TR) trend showing the air charge motion intensity to actually be destroyed by the liquid jets during the whole injection duration (Fig.5.35).

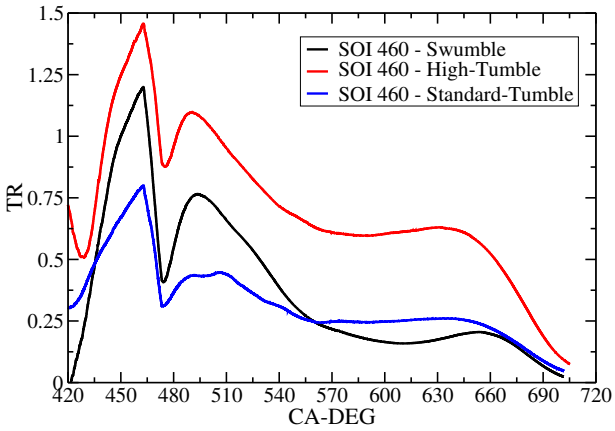

Figure 5.35: *Computed TR trends, SOI 460 CA*

As mathematically described by Eq.5.25 the TR quantity was numerically computed from a mean velocity distribution on the central engine symmetry plane as the ratio of the equivalent solid body angular speed to the engine speed [101].

$$TR = \frac{\sum_{i=1}^{n}\sum_{j=1}^{m}(\vec{r}_{i,j} - \vec{r}_c) \times \vec{U}_{i,j}}{\omega \sum_{i=1}^{n}\sum_{j=1}^{m}(\vec{r}_{i,j} - \vec{r}_c) \cdot (\vec{r}_{i,j} - \vec{r}_c)} \tag{5.25}$$

The tumble ratio is thus described as a vector perpendicular to a plane parallel to the cylinder axis with the center of rotation equal to the centroid of the cylinder symmetry plane. The $(\vec{r}_{i,j} - \vec{r}_c)$ term stands for the distance of a specific position *(i,j)* from the center of rotation with the index *i* referred to the x direction and the index *j* to the y direction. The parameter ω is the angular engine speed while $\vec{U}_{i,j}$ represents the velocity at the reference position.

Concerning the 540 CA start of injection time Fig.5.36 reports a comparison at 697 CA between SOI 460 CA and SOI 540 CA "high-tumble" cases of the mixture fraction distribution on a cut-plane perpendicular to the cylinder axis. As it was possible to expect the late injection condition displays increased charge inhomogeneities due to the delayed SOI.

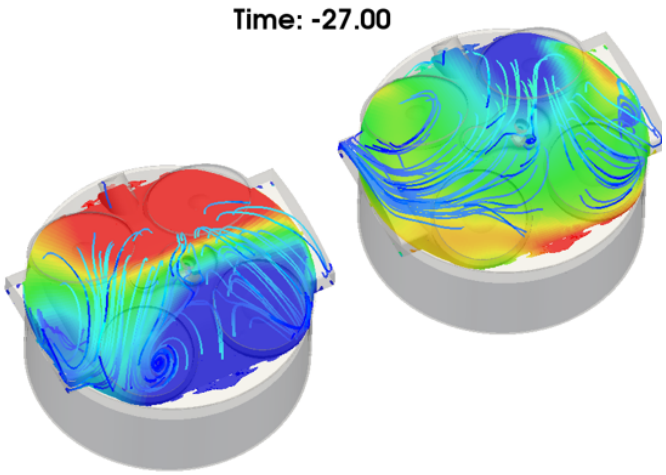

Figure 5.36: *Effects of delayed SOI on mixture distribution, "high-tumble" configuration, SOI 540 CA (left) against SOI 460 CA (right)*

For the 540 CA SOI configurations a detailed comparison between the "swumble" and the "standard tumble" simulations was carried out. Within this context, Fig.5.37(a)-5.37(b), Fig.5.38(a)-5.38(b) and Fig.5.39(a)-5.39(b) report front visual comparisons of the interaction between the injected fuel and the in-cylinder air charge for selected times respectively ranging from early injection to post EOI. In-cylinder motion is visualized by means of streamlines coloured by the gas velocity magnitude.

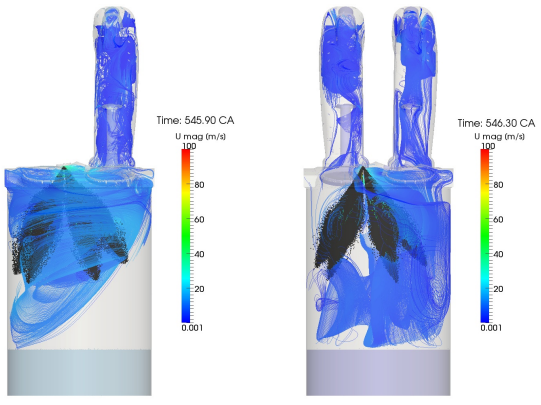

(a) Swumble (b) Standard tumble

Figure 5.37: *SOI 540, early injection times*

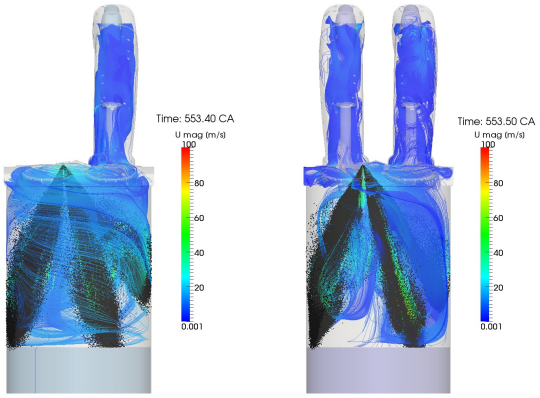

(a) Swumble (b) Standard tumble

Figure 5.38: *SOI 540, full injection times*

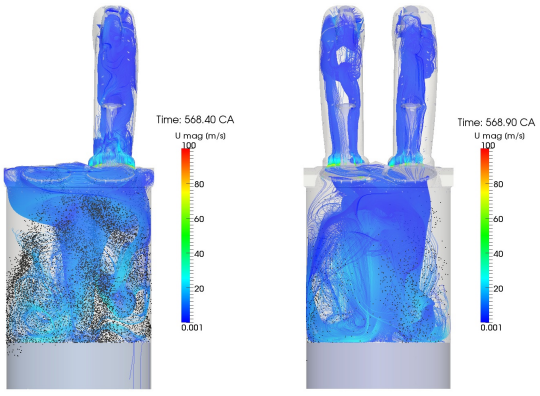

(a) Swumble (b) Standard tumble

Figure 5.39: *SOI 540, post EOI*

As expected, both cases show a lower intensity of the in-cylinder charge motion compared to the previous SOI 460 CA conditions because of the engine intake stroke approaching the IVC. As a consequence it is possible to observe that the interaction between the the gas phase and the spray is considerably reduced with the liquid jet proceeding almost undisturbed towards the engine walls. Coherently, Fig.5.40 shows that a similar amount of impinged liquid is found on the piston surface at 700 CA between the "swumble" and the "standard tumble" conditions.

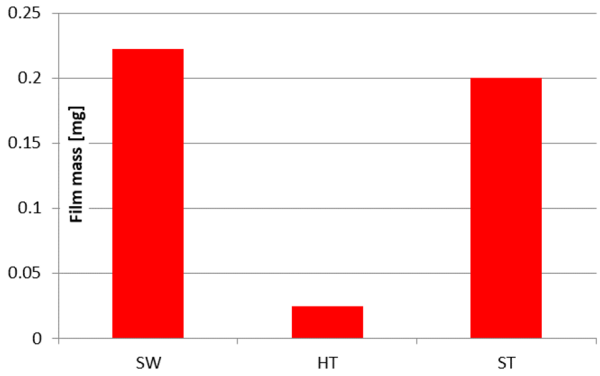

Figure 5.40: *Wall film, impinged fuel mass on the piston surface, SOI 540 CA, 700 CA*

The computed in-cylinder HI displayed in Fig.5.41 shows that a slightly higher mixture homogeneity is provided by the "swumble" configuration. However, λ probability function distributions of Fig.5.42(a)-5.42(b) confirm the presence of local rich and lean spots at 700 CA due to the reduced amount of time available for the air-fuel mixing process because of the delayed SOI.

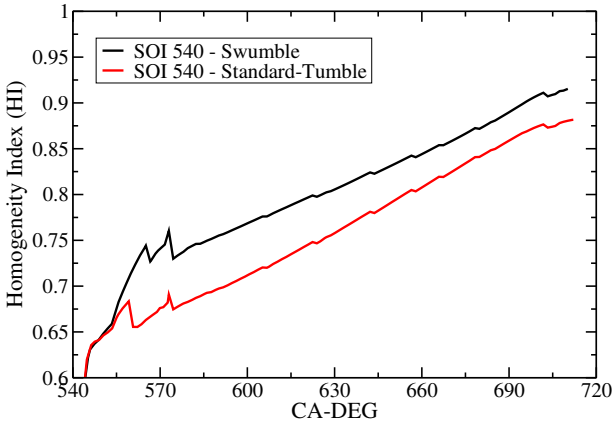

Figure 5.41: *Homogeneity Index (HI), SOI 540 CA, "swumble" and "standard tumble" configurations*

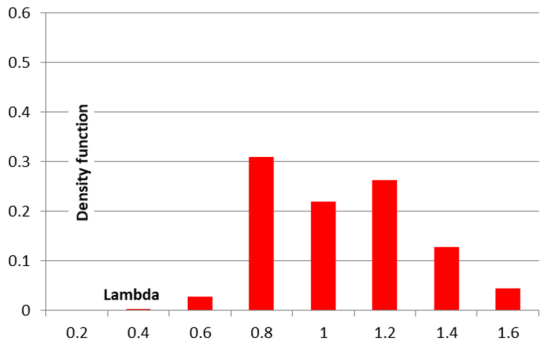

(a) Swumble

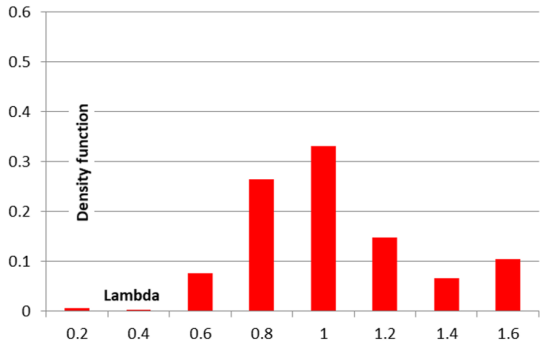

(b) Standard tumble

Figure 5.42: *SOI 540, λ distribution, 700 CA*

The overall inhomogeneity of the mixture is also demonstrated by the in-cylinder cut planes carried out at 700 CA both for the "swumble" and "standard tumble" configurations and reported in Fig.5.43 as coloured by the λ field.

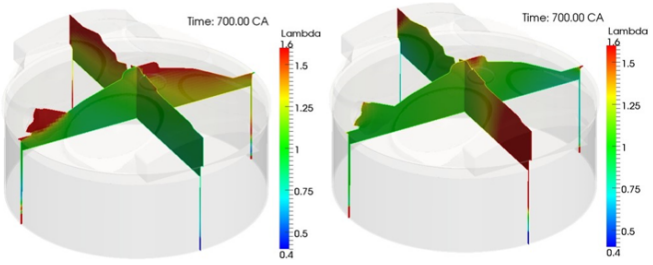

Figure 5.43: *3D in-cylinder λ field distribution at 700 CA, SOI 540 CA, "swumble" case (left) and "standard tumble" case (right)*

The "swumble" configuration is characterized by the presence of lean mixture nearby the spark-plug and the cylinder head with both lean and rich spots in the crevices. The "standard tumble" simulation shows a mixture distribution closer to stoichiometric con-

ditions in the center of the chamber and near the spark-plug but also a very lean zone on the right intake-side of the cylinder.

Moreover, the destructive effects on the intake charge motion due to the injector targeting are also observed for the SOI 540 CA cases thanks to the computed TR trends reported in Fig.5.44.

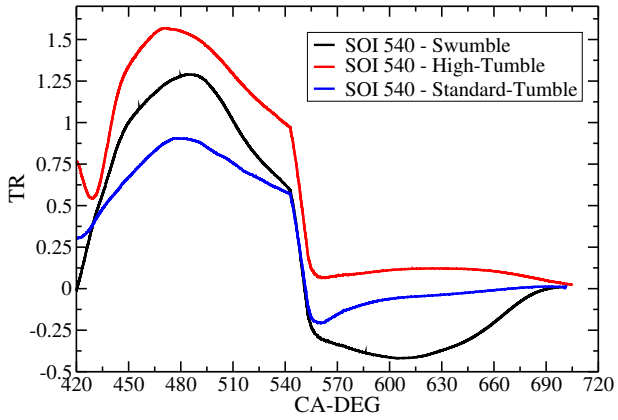

Figure 5.44: *Computed TR trends, SOI 540 CA*

Within the context of the UPGRADE project, the numerical research activity carried out on the IFPEN optical engine was concluded with the execution of combustion simulations for the previously described cases. Even if combustion investigations are not the main topic of this work few of the achieved results are reported in this section as they represent the final validation of the gas exchange, GDI injection and mixture formation modeling activities which stand at the core of this thesis.

The numerical methodology adopted to model both combustion and soot formation in modern GDI engines is summarized in Fig.5.45.

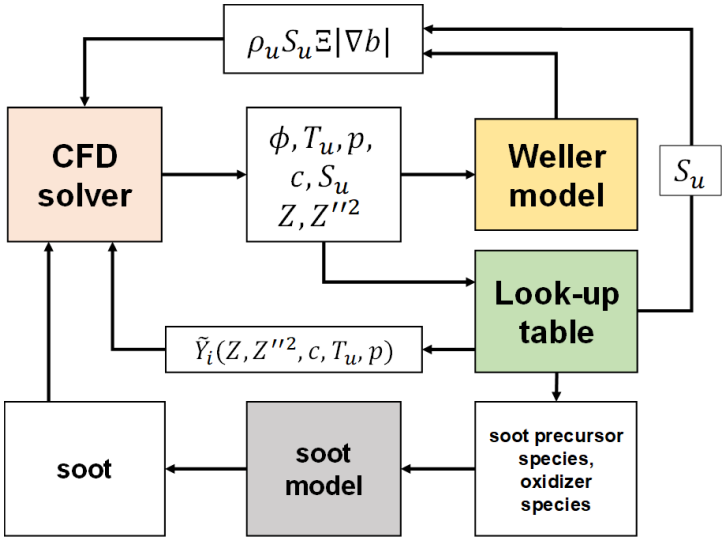

Figure 5.45: *GDI combustion and soot modeling methodology for GDI engines [57]*

Transport equations are solved for mass, momentum, energy, turbulence, mixture fraction and mixture fraction variance. Moreover, the combustion model solves a transport equation for the combustion regress variable with source terms related to ignition and turbulent flame propagation which is described by a Weller model [122] based on the laminar flamelet concept. The reaction rate is then computed by the model in each computational cell. A distinction between laminar and turbulent flame stretch is taken into account with a flame wrinkle factor estimated on the basis of the equilibrium value and a global transition factor. The latter is computed by the Herweg and Maly correlation [35] on the basis of the near average data of turbulence intensity, velocity and global flame radius which is derived from laminar flame speed and flame stretch. A lookup table provides the burned gas chemical composition from the cell thermodynamic and mixing conditions including the mass fraction of soot precursors. The latter can eventually be used by a semi-empirical model for the prediction of particle emissions. For more detailed insights on the overall combustion modeling methodology the reader is referenced to corresponding literature data [57].

Fig.5.46, related to the "swumble" and "high-tumble" SOI 460 CA cases, illustrates how the flame propagation is affected by tumble and swumble charge motions. The swirl motion persists even after the end of the combustion process thus probably increasing the mixing with consequent reduction of soot emissions. The SOI is antici-

pated enough to produce a nearly homogeneous mixture at spark timing and the flame is almost symmetrical with respect to the spark plug.

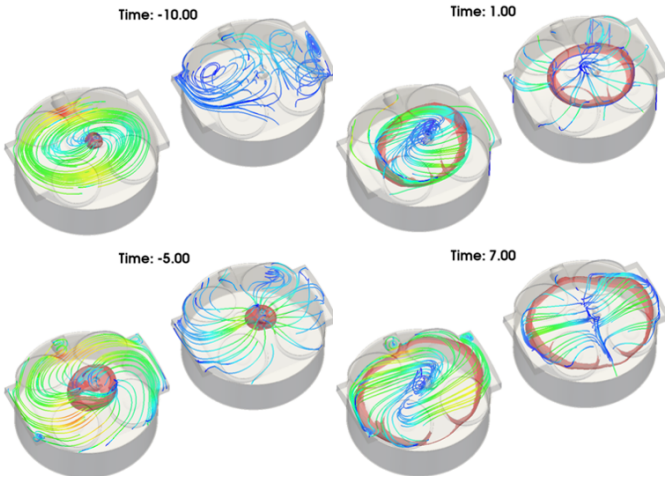

Figure 5.46: *Interaction between flame propagation and charge motion at different times, SOI 460 CA, "swumble" (left) and "high-tumble" (right) cases*

Fig.5.47(a)-5.47(b) show that for both cases there is a rather good agreement between computed and experimental data of in-cylinder pressure and apparent heat release rate (HRR).

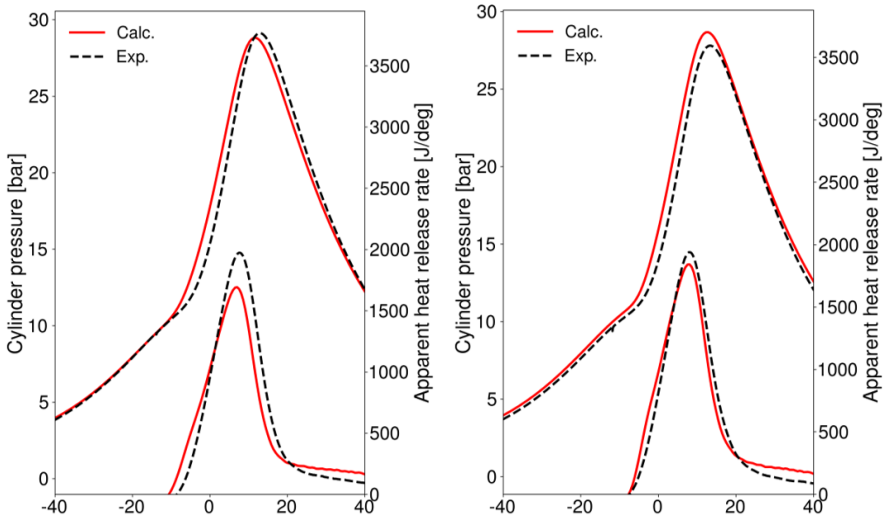

(a) Swumble (b) High-tumble

Figure 5.47: *Validation against experimental data of computed cylinder pressure and apparent HRR, SOI 460 CA*

Finally, concerning the "high-tumble" SOI 540 CA case Fig.5.48 demonstrates that,

despite the presence of a less homogeneous charge because of the delayed SOI, there are no relevant differences either on flame propagation and combustion modeling with provided overall accurate results.

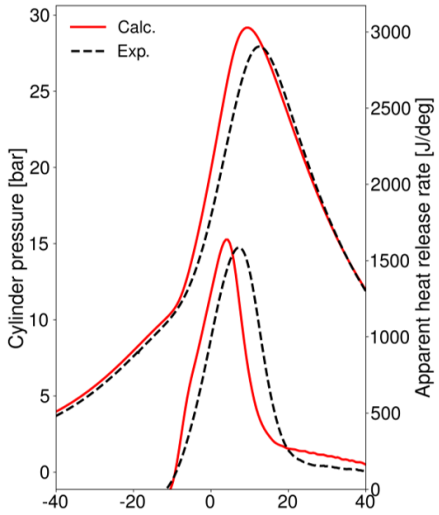

Figure 5.48: *Validation against experimental data of computed cylinder pressure and apparent HRR, SOI 540 CA, "high-tumble" case*

5.4 Conclusions

5.4.1 ECN6 Workshop Simulations

The proposed numerical setup for Spray G vessel simulations allowed to overcome many of the weak points typical of the preliminary approach discussed in Chapter 4. In particular, improvements were observed in terms of:

- prediction of the centerline velocity for the baseline G1 condition. The new results much better reproduced both the negative and positive zones of the profile with respect to available experimental data;
- prediction of the axial liquid and vapor penetrations for all the tested ECN operating points ranging from high to low evaporation rate;
- reproduction of the spray morphology at early, late and post injection times for each ECN operating point;

- consistency from case to case as each simulation was performed with the same mesh structure, cell size and secondary breakup model parameters.

Moreover, thanks to the Adachi-Rutland flash boiling evaporation model specifically implemented into the LibICE during this work even the challenging flash vaporization G2 operating point was reproduced with a very good grade of accuracy as far as spray morphology and in-plume axial liquid distribution are concerned.

Still, it was observed that there is further room for improvements concerning the following aspects:

- spray PCA reproduction. For each case, PLV maps demonstrated that the experimental plume cone angle is still greater than the respectively adopted computational values;
- spray morphology and in-plume liquid distribution. The novel post-processing methodology based on the projected liquid volume Eulerian field highlighted once more that axial liquid and vapor penetration profiles alones cannot be considered enough to fully assess the overall quality of a simulated GDI spray. In this regard, both G1 and G3 simulations were characterized by an "arrow-like" shape of the tip of the plumes which in turn appeared to carry more liquid mass than they should according to the experimental evidence at comparable times. The child parcels mass stripping mechanism of the KH secondary breakup model as well as the interaction between primary and secondary numerical atomizations are considered to be the main processes responsible for these observations.

As a general summary, in Tab.5.5 are reported the parameters which hold the highest influence on the improved numerical results along with those which still need interventions in order to further improve the available spray setup.

5.4.2 IFPEN Optical Access Engine Simulations

The research activity carried out on the IFPEN optical access engine represented an ideal condition to benchmark the proposed numerical spray models on simulations of a whole engine cycle. Moreover, it was also possible to carry out a comprehensive assessment of the full-cycle numerical setup available into the LibICE since three different

Table 5.5: *Impact of model parameters on achieved results (+) and on possible improvements (-)*

Imposed PCA	++
Decoupled PCA-atomization model	++
Pope round-jet correction	++
Flash boiling model	++
Mesh refinement and consistency	+
Shear stripping	+
Spray morphology (stripping breakup)	- -
Spray morphology (in-plume liquid distribution)	- -
Spray morphology (PCA value)	-

intake ports configurations ("high-tumble", "swumble" and "standard") were analyzed. No accurate combustion results can in fact be achieved without not only a good reproduction of the spray physical evolution but also a reliable prediction of the in-cylinder gas exchange process. It was observed that the numerical spray setup which was proposed for the ECN6 simulations well behaved both for the adopted SOI values (460 CA and 540 CA) in terms of breakup and evaporation rate. It could be stated that, despite the fact that parameters such as spray morphology and in-plume liquid distribution could be further optimized, the current numerical framework well predicted the most important physical phenomena influencing the interaction between the in-cylinder flow (related to mesh quality, numerical schemes, turbulence modeling and boundary conditions) and the liquid spray (directly influenced by breakup, evaporation and wall film models). This is proven by achieved combustion results showing good matchings between experimental and numerical pressure and apparent HRR profiles for each tested condition.

CHAPTER 6

Updated Prediction and Interaction of Atomization and Secondary Breakup Phenomena

Within the context of the analysis carried out in the previous chapters the specific interaction between atomization and secondary breakup processes is here further investigated. Updated models are proposed with the aim to improve the prediction of GDI sprays morphology under a wide range of operating conditions. Different numerical mechanisms were tested on the Spray G injector and the optimal solutions were implemented into the LibICE framework.

More in detail, in this chapter observations and results related to research acvities carried out on the coupling between dedicated atomization and secondary breakup numerical approaches are discussed. At first an atomization mechanism based on the original Pilch-Erdman [88] proposition was tested on the baseline G1 case. Afterwards, evidence from this test led to the validation of a decoupled KH methodology on the Spray G3 both under static vessel and dynamic conditions in the Darmstadt optical

access engine. Finally, the improved approach for the management of the atomization phase was further tested on the Spray G2 and G3 conditions by coupling it with a predictive literature-based KHRT secondary breakup model proposed by Nagaoka and Kawamura [70] and specifically implemented into the LibICE during the current research activity. Moreover, the flash boiling evaporating Spray G2 condition represented a further benchmark for evaluating the effects of the Adachi-Price evaporation model [92] which was suitably implemented into the LibICE framework. Strengths and weak points of the overall numerical setup were finally assessed with the aim to provide a comprehensive approach both for low-evaporating and high-evaporating GDI sprays. Within this context, validations on both high-evaporating G1 and G7 ECN cases were carried out against dedicated experimental data.

6.1 Numerical Atomization by Means of the Pilch-Erdman Mechanism: Spray G1 Vessel Results

By following the evidence gathered from numerical simulations carried out in Chapter 4 and Chapter 5, both atomization and secondary breakup phases were at first carried out with a single model based on the general KHRT mechanism. In particular, as suggested in literature [19] a dedicated KH atomization approach was considered within a specific spray core length region while the classic competing KHRT method was employed for the secondary breakup. The atomization core length was calculated according to Eq.6.1 [19]

$$L_c = C \cdot d\sqrt{\frac{\rho_l}{\rho_g}} \tag{6.1}$$

where C is a parameter expressing the influence of the nozzle flow conditions, d is the parcel diameter and ρ_l and ρ_g respectively represent the liquid and ambient gas densities.

Within this context, it was observed [77] that a B_1 parameter kept in common both for atomization and secondary breakup would lead to an overpredicted reduction of the parcels diameter nearby the injector nozzle. As a consequence, the spray morphology would be deformed by the small parcels carried on by the injection momentum which would not evolve any further downstream of the spray plumes. Moreover, to

have parcels with such a small diameter in the liquid core would negatively influence the entrainment because their interaction with the surrounding gas would be negligible. Consequently, an inaccurate prediction of the centerline velocity was observed. To address this problem a methodology based on the multi-motion regimes proposed by the research of Pilch and Erdman [88] was considered [77] for performing the primary atomization of the spray. The aim of this choice was to ensure that the diameter of the discrete parcels within the core length would be reduced gradually and smoothly leading to benefits both to the near-nozzle numerical spray morphology and the prediction of the centerline velocity. More in detail, the new parcel diameter within the core length is continuously updated according to the rate equation described in Eq.6.2 where D is the initial parcel diameter, D_{new} is the updated diameter at the end of the time-step and D_s represents the stable drop diameter proposed Pilch and Erdman [88] below which the secondary breakup of a specific drop is stopped.

$$D_{new} = \frac{D + frac \cdot D_s}{1.0 + frac} \tag{6.2}$$

The term *frac* is described according to Eq.6.3 where dt is the simulation time-step while τ_{PE} is the total dimensional breakup time calculated by multiplying the motion-dependent total adimensional breakup time from Pilch-Erdman [88] by the τ temporal term reported in Eq.6.4.

$$frac = \frac{dt}{\tau_{PE}} \tag{6.3}$$

$$\tau = \frac{D}{U_{rel}} \left(\frac{\rho_l}{\rho_g} \right)^{0.5} \tag{6.4}$$

The fundamentals of the KHRT methodology applied to the secondary breakup are the same of the Reitz-KHRT model which was adopted for the simulations reported in Chapter 4 and Chapter 5. However, a difference stands in the way the mass and thus the number of droplets of the stripped child KH parcels are computed. Under this latest configuration the *stripped mass of each parcel* m_{strip} is tracked and updated at each new time-step. When the KH stripping conditions are satisfied the *mass for stripped droplet* $m_{strip,d}$ is calculated with reference to the D_{KH} diameter. The ratio between

m_{strip} and $m_{strip,d}$ represents the number of droplets contained in the stripped mass and thus in the stipped numerical parcel. If such a computed quantity is greater than the number of droplets contained in the original parent parcel the KH stripping breakup takes place and a new child parcel is introduced into the computational domain.

The Pope correction [90] was applied as well with a value of 1.5 for the $C_{1\varepsilon}$ parameter in the turbulence dissipation rate ε transport equation.

The computational grid was defined on the basis of previous spray investigations [75] and consisted into a structured 3D mesh with Adaptive Mesh Refinement (AMR). The minimum cell size is equal to 0.5 mm coherently with full-cycle GDI engine simulation cases. Parcels were injected into the domain with a velocity value function of the C_v *velocity coefficient* set equal to 0.73 [6].

The test case consisted into the vessel Spray G1 operating condition with the main numerical parameters collected in Tab.6.1.

Table 6.1: *Spray model main parameters*

B_1	28
C_{RT}	0.8
Plume cone angle	17°
Drill angle	37°

Fig.6.1 shows the differences in predicted spray morphology between a classic KH approach with equal B_1 constant both for atomization and secondary breakup and the Pilch-Erdman-based method proposed in this work. Under the former configuration chances are that the transition between atomization and secondary breakup is never going to be completely predicted. In fact, a single B_1 value for both events means that the user is not taking into account the differences in terms of motion that arise between parcels that are within or out of the core length. That is, if a low B_1 value is required to correctly predict the secondary breakup phase the same parameter would probably not suit an accurate description of the atomization regime. As a consequence, the spray could be characterized by very small child droplets being stripped in the core length region which would negatively influence morphology, axial penetrations and interaction with the surrounding gas. On the other hand, the PE-based approach ensures a smooth diameter reduction of the primary parcels which should only be related to the specific spray conditions. Moreover, such a decoupled interaction between atomization and

secondary breakup allows the user for a higher degree of freedom with respect to the different tuning options, so that it is possible to carry out a more detailed calibration of the secondary breakup model.

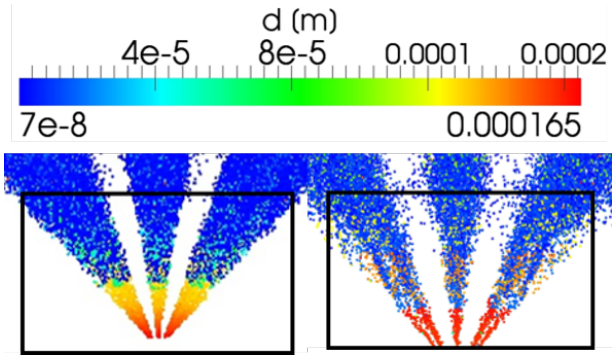

Figure 6.1: *Primary atomization, Pilch-Erdman (left) and KH (right). Parcels colored on diameter size (maximum 0.165 mm, minimum 1e-5 mm) [77]*

Good results in terms of axial liquid and vapor penetrations against available experimental data (Fig.6.2(a)-6.2(b)) were obtained with this model along with a good entrainment prediction as it is shown in Fig.6.2(c).

The analysis of the axial PLV profiles (Fig.6.3(a)-6.3(c)) and of the morphological PLV maps (Fig.6.4(a)-6.4(c)) further confirmed the importance of a correct prediction of the spray atomization phase and of a correct coupling with the secondary breakup modeling.

Finally, Fig.6.5(a)-6.5(b) and 6.6(a)-6.6(b) allow to investigate computed liquid droplets velocity and SMD at different times. Experimental measurements [81] were performed at an axial distance of 15 mm from the injector nozzle and on a radial profile of 10 mm. Time values of 0.3 ms (early injection phase) and 0.6 ms (late injection phase) were considered for the analysis.

These results further proved the importance of a good prediction of the parcels diameter reduction rate in the core length of the spray.

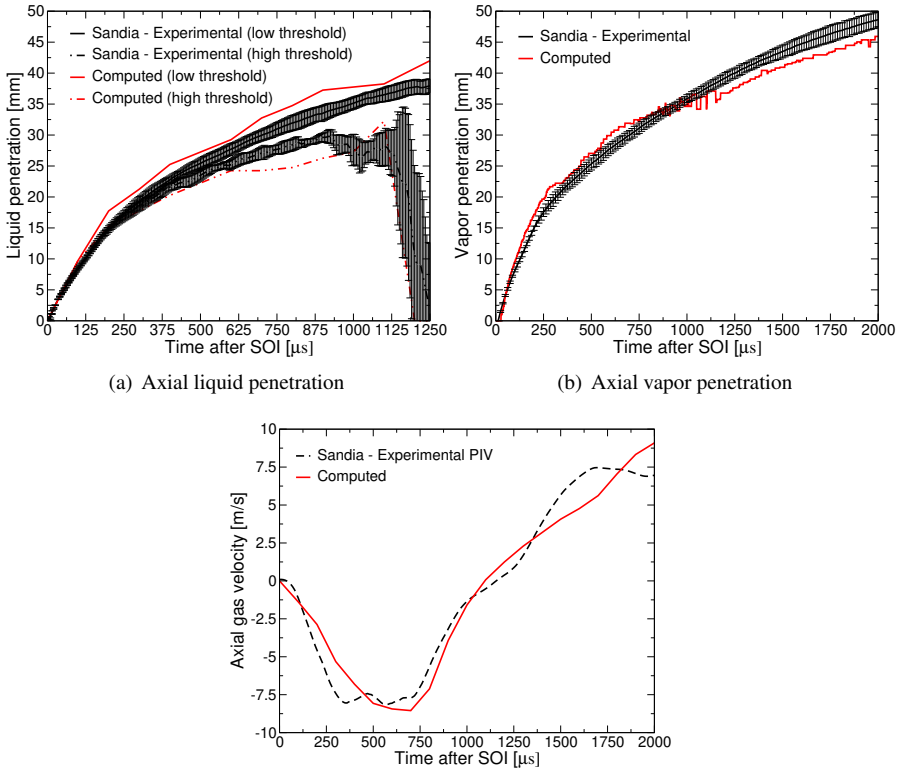

(a) Axial liquid penetration

(b) Axial vapor penetration

(c) Centerline axial velocity

Figure 6.2: *Validation of computed axial spray penetrations and centerline velocity [77]*

6.2 Numerical Atomization by Means of a Decoupled KH Approach

The proposed approach based on the Pilch-Erdman implicit equation only represents a single possible alternative to differently characterize the atomization phase. What appears to really be mandatory for a good reproduction of a GDI spray is to decouple numerical atomization and secondary breakup zones by providing a specific core length where the Pilch-Erdman approach or a KH mechanism with a dedicated $B_{1,atom}$ parameter could be employed. Within this context, the research activity continued by assessing the effects on the numerical spray due to a decoupled KH approach between atomization and secondary breakup by means of the investigation of the Spray G3 operating point [83] both in vessel and under real engine conditions. More in detail, the validation was carried out thanks to the experimental coupling between the ECN Spray G injector geometry and the Darmstadt optical access engine [30].

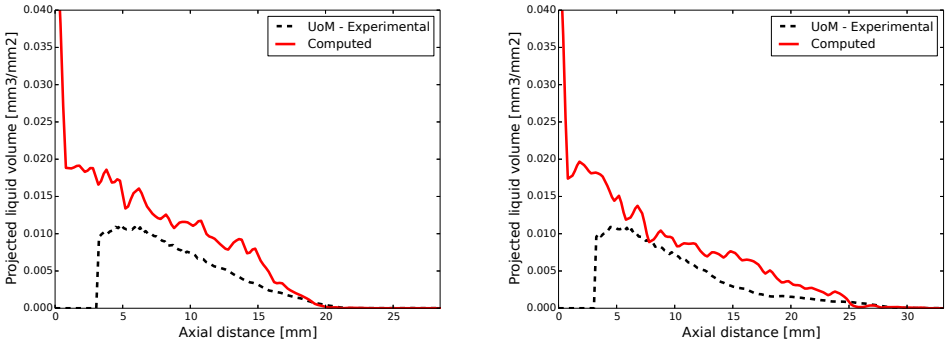

(a) 0.3 ms

(b) 0.6 ms

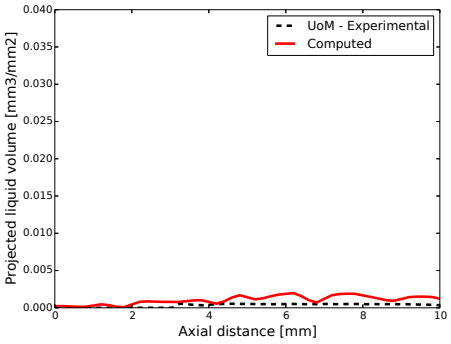

(c) 0.9 ms

Figure 6.3: *Axial PLV profiles, comparison between UoM experimental results and computed spray [77]*

6.2.1 Spray G3 Vessel Results

The numerical spray setup adopted for the vessel simulation was kept constant as well for the engine calculations and it is summarized in Tab.6.2.

Table 6.2: *G3 condition, spray model main parameters*

Turbulence model	RANS, standard k-ε, $C_{1\varepsilon} = 1.55$
Mesh	structured 3D, no AMR
Cell size	Constant at 0.5 mm
$B_{1,atom}$	40
B_1	50
C_{RT}	0.4
C_v	0.73
PCA	30°

It is possible to notice that the $B_{1,atom}$ atomization parameter is lower than the B_1

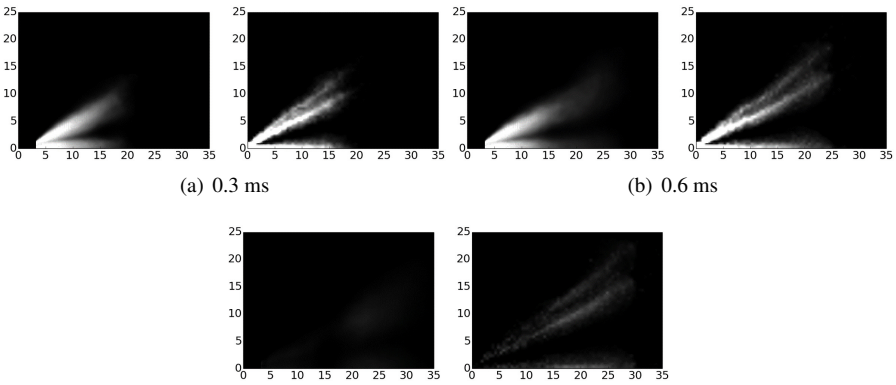

(a) 0.3 ms (b) 0.6 ms

(c) 0.9 ms

Figure 6.4: *PLV maps, comparison between UoM experimental results (on the left) and computed spray (on the right). Range is* $0 - 0.01 \frac{mm^3}{mm^2}$ *[77]*

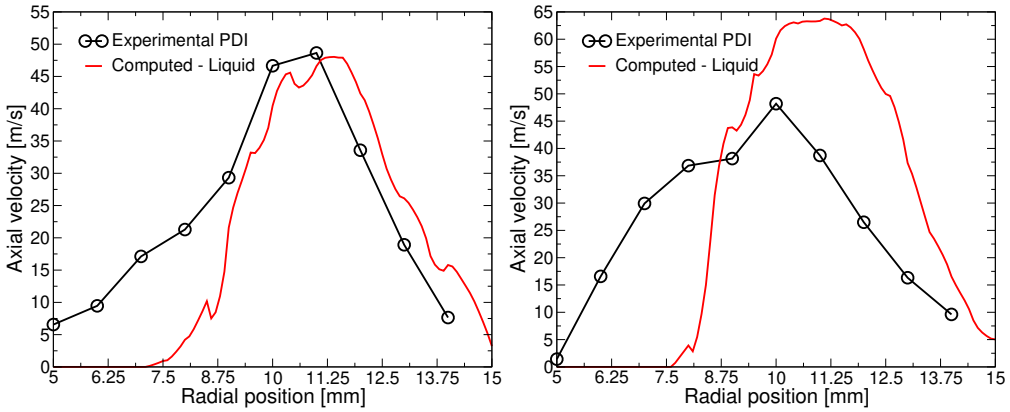

(a) 0.3 ms (b) 0.6 ms

Figure 6.5: *Radial PDI for liquid droplets velocity, experiments against simulation [77]*

which is dedicated to the secondary breakup. This fact was observed throughout the work to be an indicative characteristic of low-evaporating GDI spray conditions. A computational grid of 0.5 mm and without AMR was employed for the vessel to ensure maximum consistency with the full-cycle engine meshes dedicated to the injection phase.

At first, a visual comparison between G3 simulations respectively carried out with the decoupled KH and PE atomization approaches is reported to discuss about the effects of the two methods on the primary breakup phase. Within this context, Fig.6.7(a)-6.7(b) show the analysis of the atomization phase at 0.1 ms for the KH-based approach with reference to two specific parameters that are the stripping index (*stripIndex*) and the parcel diameter. The same post-processing procedure is reported for the case with

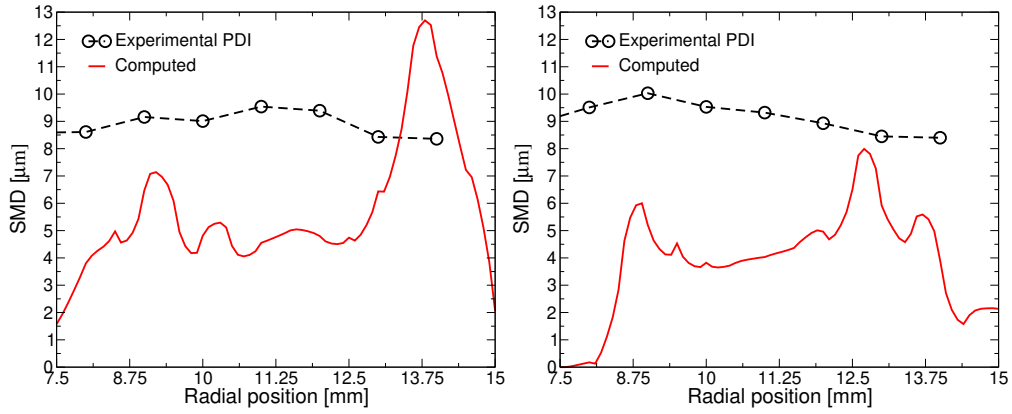

(a) 0.3 ms (b) 0.6 ms

Figure 6.6: *Radial PDI for the SMD, experiments against simulation [77]*

the PE atomization mechanism in Fig.6.8(a)-6.8(b).

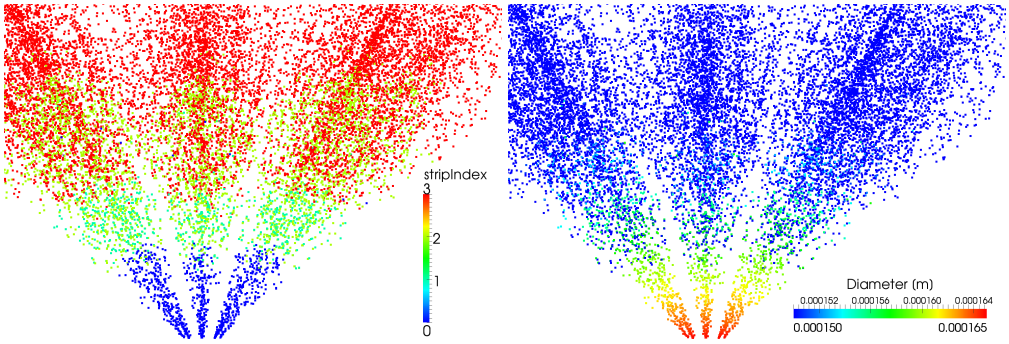

(a) Stripping index (b) Parcel diameter

Figure 6.7: *G3 simulation, KH atomization approach, 0.1 ms, detail of the spray evolution during the primary breakup phase*

The stripIndex parameter allows to understand if an injected parcel (value equal to 0) was subjected to diameter reduction (value equal to 1). Moreover, for the KH mechanism the stripped child parcels within the atomization core length assume a value of 2 while if the parameter becomes equal to 3 it means that the parcel was subjected to secondary breakup. This comparison allows to immediately understand the differences between the two approaches. The PE-based atomization shows just a gradual diameter reduction of the injected parcels (with the exception of those with a very limited Weber number which do not undergo atomization) while all the potentially stripped mass is stored and then assigned to child parcels which are stripped with the KH approach during the secondary breakup phase. On the contrary, the KH-based atomization mech-

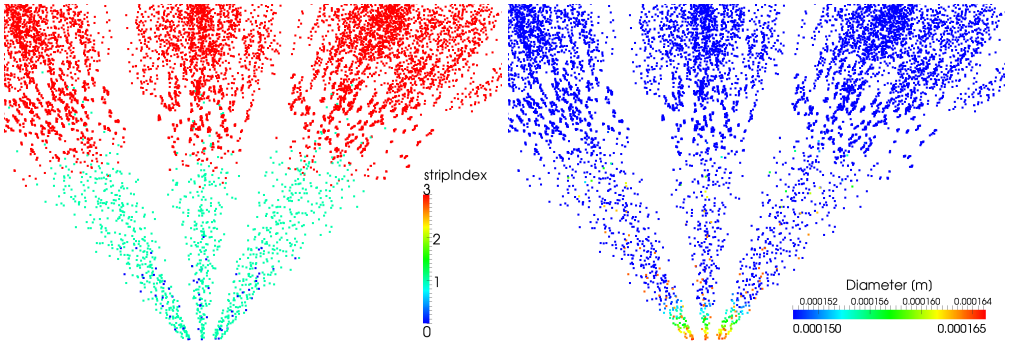

(a) Stripping index (b) Parcel diameter

Figure 6.8: *G3 simulation, PE atomization approach, 0.1 ms, detail of the spray evolution during the primary breakup phase*

anism includes the stripping activity even within the core length, fact which leads to a considerable difference in terms of computed spray morphology. In fact, as it is possible to observe in Fig.6.7(a) as long as the physical requirements for stripping breakup are not satisfied the drops are not subjected to atomization (stripIndex equal to 0) and they thus keep a diameter value which is very close to that of the injector hole for a higher distance from the nozzle if compared to the PE mechanism. Afterwards the KH activity starts and the parcels are subjected to diameter reduction and also stripping if a minimum threshold of total stripped mass is satisfied. As a consequence, the effects on the spray morphology consist into a more uniform diameter reduction rate, the presence of more parcels in the computational domain and a greater plume-to-plume interaction outside of the atomization core length. Overall, the PE mechanism represents a faster approach with less tuning activity required from the user for the reproduction of the atomization phase also between different operating conditions. However, this setup requires a more sensible calibration activity for the secondary breakup models in order to accurately predict quantities such as axial spray penetrations and entrainment. On the other hand, by employing a dedicated KH model for atomization the user has more control on the evolution of the spray within the core length and thus an easier interaction with the secondary breakup activity in terms of overall calibration can be achieved. Still, experience is required from the user to correctly set accurate values for the B_1 atomization parameter according to the specific spray operating conditions. Within this context, it must be remembered that the proper tuning of a GDI spray setup also heav-

ily depends on the mesh quality/refinement, the adopted numerical schemes, injector velocity coefficient, geometry and operating condition and the value of the plume cone angle. It is thus not a straightforward task to suggest a priori defined values for the B_1 parameters dedicated both to atomization and secondary breakup. On the basis of the experience gathered within this research activity, for low-evaporating conditions such as the ECN Spray G3 and cases with even lower ambient density the required atomization B_1 constant appeared to be lower in value compared to that related to the secondary breakup process (with a suggested general range of 10-40). Instead, G1, G4 and G7 operating conditions required a higher value for the $B_{1,atom}$ parameter (up to 90) compared to the secondary B_1 (range of 30-50), with the aim not to overestimate the intensity of the stripping activity within the core length since average spray Weber gas number and ambient density are already high enough to promote a strong diameter reduction rate.

Validation of the computed axial vapor penetration for the KH atomization approach vessel simulation is shown in Fig.6.9 while Fig.6.10 reports the computed axial liquid penetration.

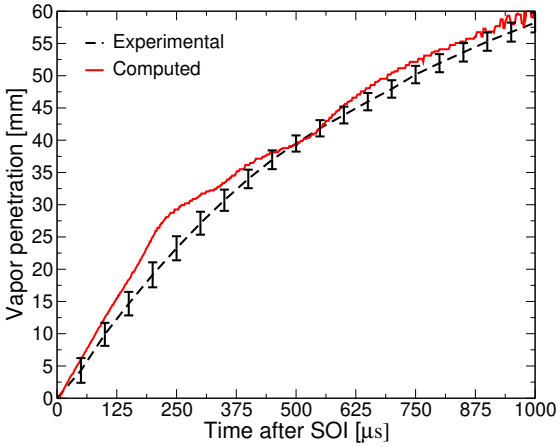

Figure 6.9: *G3 vessel simulation, comparison between experimental and numerical axial vapor penetration [83]*

A good accuracy was achieved and it is worth observing that the results are obtained with higher B_1 and C_{RT} model constants compared to what was shown in the previous chapters. This fact is a direct consequence of the adoption of a constant 0.5 mm size mesh without the employment of the AMR technique. The AMR allows to dynamically

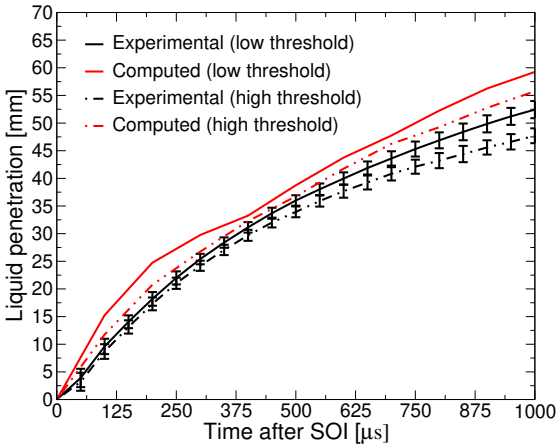

Figure 6.10: *G3 vessel simulation, comparison between experimental and numerical axial liquid penetration [83]*

refine the grid where the liquid is found, condition which typically leads to a smooth grid size reduction along the length of the spray plumes but does not specifically treat the axial zone of the domain which, in case of the multi-hole GDI geometries such as the Spray G, is coincident with the injector axis. The consequences are both a discrepancy and an inhomogeneity in cell size between the zones at the plumes and the mesh at the centerline, fact which holds great influence on the KHRT model parameters which must be adopted so that an accurate centerline velocity trend could be computed. In this regard, while axial spray penetration values may not be subjected to visible differences since they are evaluated with reference to each plume length, entrainment and thus gas velocity on the injector centerline are considerably affected by the changes in grid structure. Without the employment of the AMR technique a homogeneous mesh size of 0.5 mm is obtained for the whole computational domain promoting both higher positive and smaller negative computed peaks in magnitude for the centerline velocity. If all the other main model parameters (injector discharge coefficient, stripped mass threshold for child parcels and PCA value) are kept constant such a behavior indicates a numerically overestimated breakup rate which could negatively affect the prediction of evaporation and mixture formation in full-cycle engine simulations. As a consequence, an increment of B_1 and C_{RT} parameters is required to counterbalance the effects due to the different mesh structure. Overall, for the sake of higher numerical accuracy and stricter consistency with the engine cases the AMR approach was discarded for every

other GDI spray vessel simulation reported in this thesis.

The in-plume liquid distribution was assessed and verified by means of the analysis reported in Fig.6.11(a)-6.11(c) where experimental and numerical axial PLV distributions are compared at different times during (0.3 ms and 0.6 ms) and after (0.9 ms) the injection process.

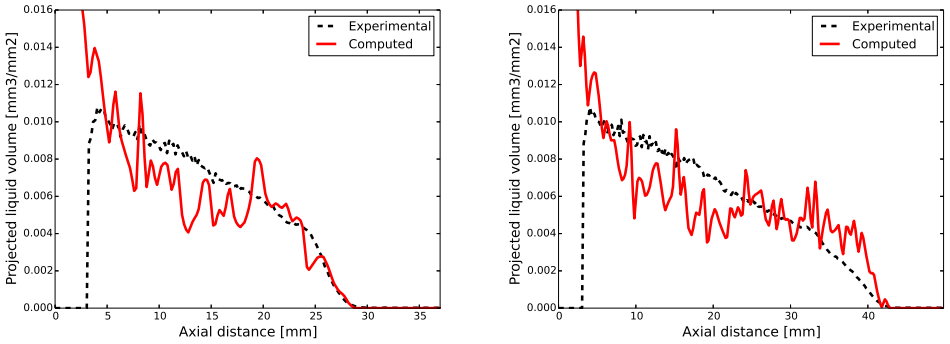

(a) 0.3 ms

(b) 0.6 ms

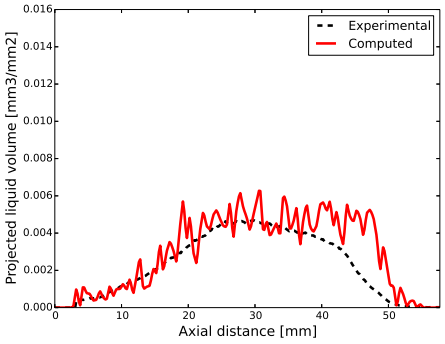

(c) 0.9 ms

Figure 6.11: *G3 vessel simulation, axial PLV profiles, comparison between experimental and computed data [83]*

Fig.6.12(a)-6.12(b) show the PLV distribution on the radial direction at two different axial distances (10 mm and 15 mm respectively) and two different times (1.3 ms and 0.8 ms respectively). The former combination allows to understand the projected Eulerian fuel field residual distribution closer to the nozzle after the end of the injection. The latter reports the analysis for a lower time and a greater axial distance to investigate the liquid distribution far away of the injector nozzle and immediately at the end of injection. Achieved results are accurate but could also be further enhanced by slightly

reducing the imposed plume cone angle or the intensity of the KH secondary parcels stripping activity. Finally, the morphology of the spray was assessed by means of the PLV maps reported in Fig.6.13(a)-6.13(c). A good matching for the in-plume evolution of the liquid core and for the transition from primary to secondary breakup can be observed, further confirming what was inferred from the analysis of the axial PLV profiles.

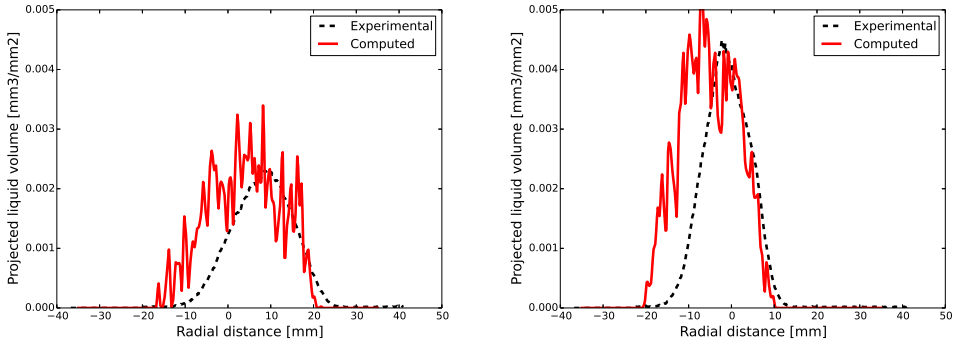

(a) 10 mm, 1.3 ms

(b) 15 mm, 0.8 ms

Figure 6.12: *G3 vessel simulation, radial PLV profiles, comparison between experimental and computed data [83]*

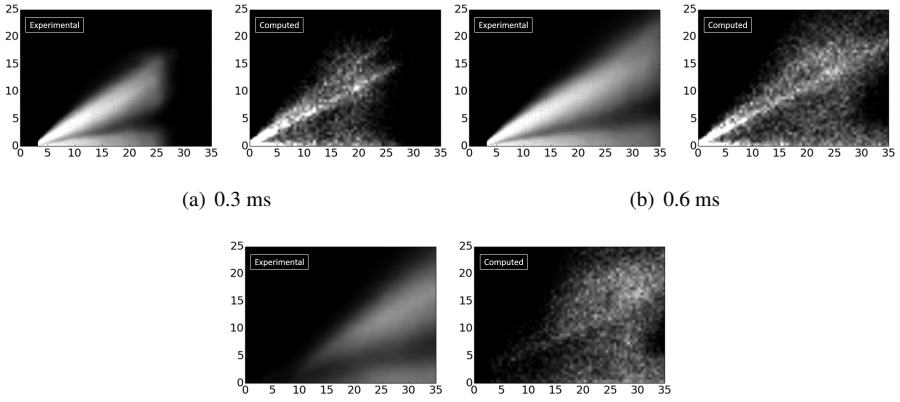

(a) 0.3 ms

(b) 0.6 ms

(c) 0.9 ms

Figure 6.13: *G3 vessel simulation, comparison between experimental and numerical spray morphologies based on PLV maps. Range is* $0 - 0.01\frac{mm^3}{mm^2}$*, axes dimensions in mm [83]*

6.2.2 Darmstadt Engine Results

The very same numerical setup was then applied to full-cycle simulations of the optical access Darmstadt engine coupled with the Spray G for a fuel injection process taking place under dynamic conditions as similar as possible to those of the in-vessel G3 operating point. Within this context, experimental engine data were only available at the time for the motored condition without fuel injection. As a consequence, the focus of this activity mainly consisted into the validation of the adopted numerical setup in terms of prediction accuracy of the main engine-related operating parameters. However, a simulation of the injection process under G3-like conditions was nevertheless carried out so that a first assessment of the in-cylinder liquid evolution and mixture fraction distribution could be performed. This analysis proved to be helpful in understanding the expected spray behavior under dynamic engine conditions and in providing a preliminary set of numerical results which could represent a starting point for future in-engine ECN Spray G research activities.

At first, cold flow simulations were thus carried out to validate the numerical reproduction of the in-cylinder ambient conditions and flow structure as it is shown by the computed in-cylinder pressure and velocities profiles reported in Fig.6.14, Fig.6.15 and Fig.6.16 respectively.

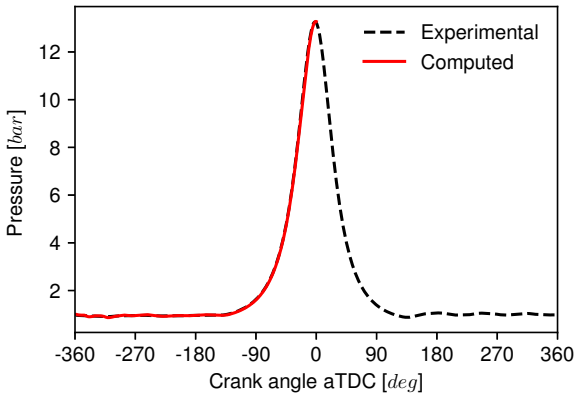

Figure 6.14: *Comparison between experimental and numerical cylinder pressure of the Darmstadt engine for the operating point A [83]*

The velocities were extracted at a crank angle value equal to $270°bTDC$ coherently with the available experimental measurements. The correct modeling of the in-cylinder

main flow structure is a mandatory requirement for an accurate prediction of the subsequent air-fuel mixture formation. Within this context, a PIV campaign with an uncertainty of 5% was performed on the optical engine to measure the in-cylinder flow onto the central tumble plane with the flow field being a result of an ensemble-average based on 500 cycles. For further details on the experimental methodology the reader is referred to [31].

In Fig.6.15 velocities were compared along two horizontal lines placed 15 mm and 25 mm below the deck surface. In Fig.6.16 three vertical lines were considered instead with the first one located -20 mm towards the intake valves, the second one at 0 mm right in the middle of the cylinder and the last one at $+20$ mm towards the exhaust valves.

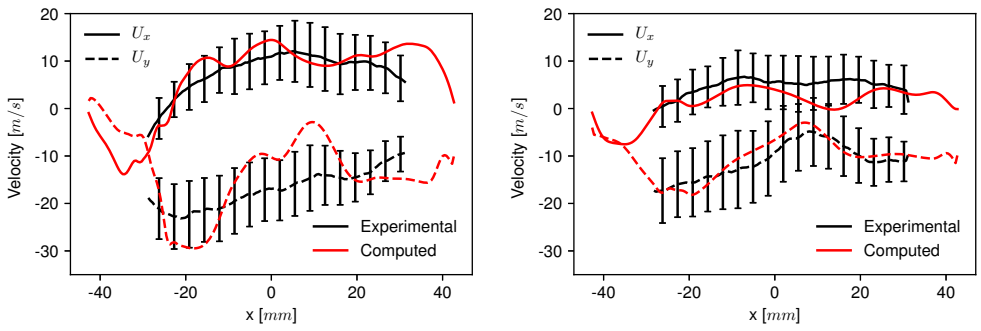

(a) $y = -15mm$ (b) $y = -25mm$

Figure 6.15: *Comparison between computed and experimental horizontal velocity profiles, on the tumble plane for the Darmstadt engine, under the operating point A, at* $90°aTDC$ *[83]*

Liquid impingement and wall film evolution were numerically treated with the same setup described in Chapter 5. Within this context, the physical interaction between the multi-hole Spray G liquid jets and the walls of the Darmstadt optical engine proved to be a considerable challenge for an accurate numerical simulation. In fact, since the injector is mounted on the center of the cylinder-head (Fig.6.17(a)) two of the eight plumes impact on the side and top surfaces of the two intake valves as it is show in Fig.6.17(b). As a consequence, these zones are characterized by moving walls conditions, direct impingement, film evaporation and film stripping due to the intake air flow motion.

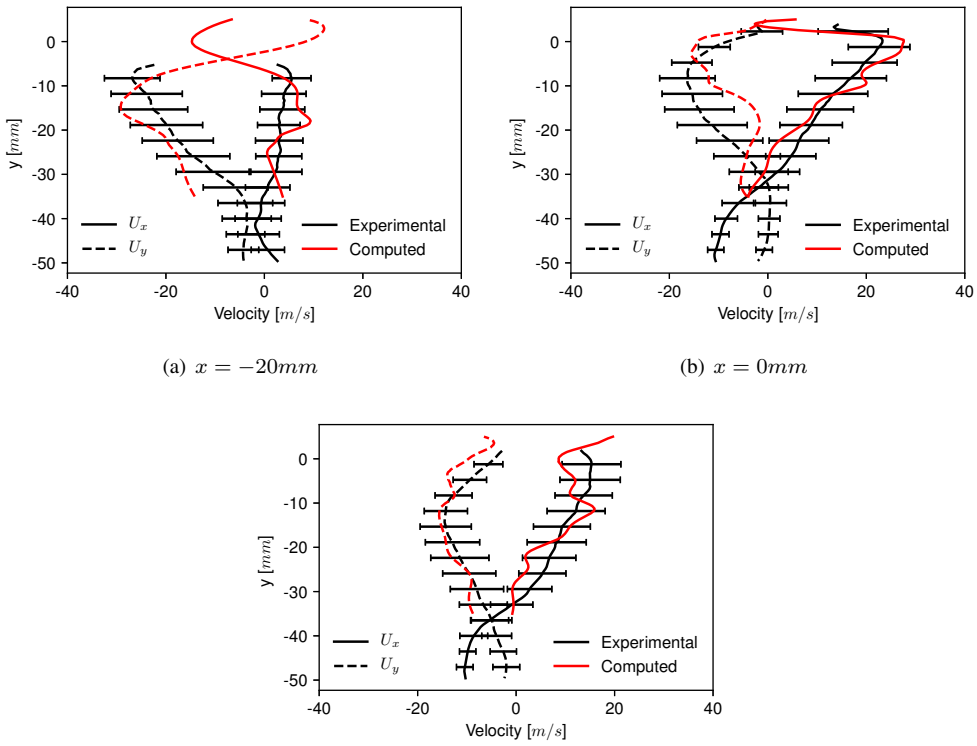

(a) $x = -20mm$

(b) $x = 0mm$

(c) $x = +20mm$

Figure 6.16: *Comparison between computed and experimental vertical velocity profiles, on the tumble plane for the Darmstadt engine, under the operating point A, at* $90°aTDC$ *[83]*

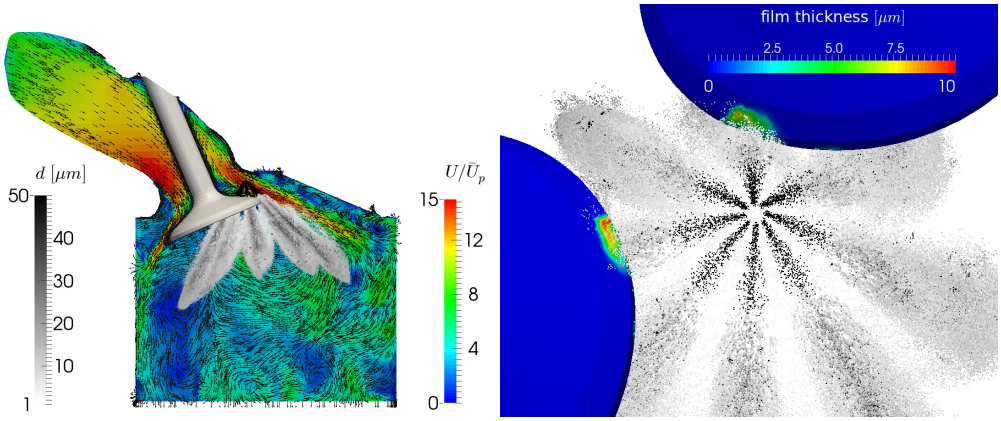

(a) Mid-valve plane, velocity fields adimensionalized with mean piston speed

(b) Detail of the interaction between jet plumes and intake valves

Figure 6.17: *Overview of the interaction between liquid spray and intake flow [83]*

In this particular case the adopted flow rate profile was the same between vessel and engine simulations. The total injected fuel mass was actually not enough to reach the

stoichiometric condition allowing the engine to fire up. As a consequence, phenomena of combustion and flame propagation could not be investigated. Still, the proposed spray numerical setup allowed to accurately model the main aspects of the expected in-cylinder charge stratification. These preliminary results are of great importance as they allowed to understand what is to be expected from future investigations on the Darmstadt engine coupled with the Spray G injector both under firing conditions and in the context of future ECN GDI dedicated research topics. More in detail, as it is shown in Fig.6.18 a set of 10 iso-surfaces was generated with the aim to observe the global distribution of the fuel vapor in the combustion chamber for the engine operating points reported in Tab.2.10.

As expected the mixture is lean for each reported operating point. However, phenomena of stratification are still visible in Fig.6.18(b) and Fig.6.18(d). Fig.6.18(e) and Fig.6.18(f) show that under high engine speed the stratification is reduced because of the diffusion which is induced by a higher TKE. For all the operating points the presence of spots with richer mixture (marked with arrows in the pictures) can be observed as a consequence of the liquid jet plumes hitting the engine walls during the injection phase and thus leading to wall-film formation.

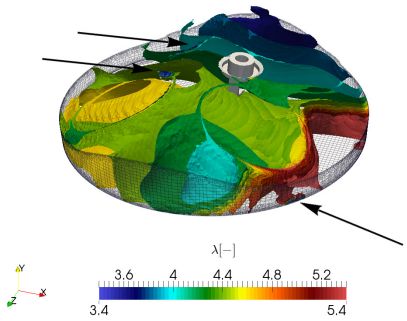

(a) Operating point A - iso surface

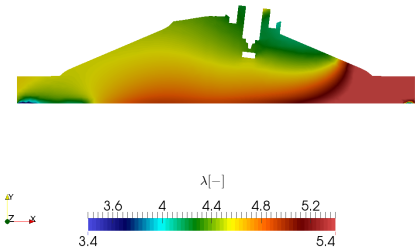

(b) Operating point A - tumble plane

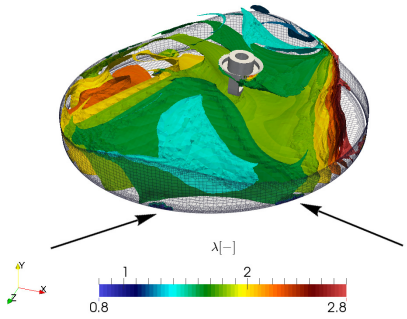

(c) Operating point B - iso surface

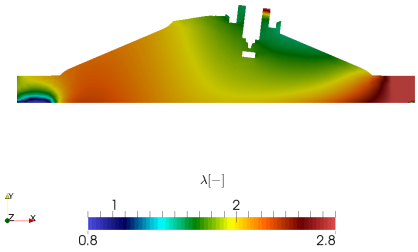

(d) Operating point B - tumble plane

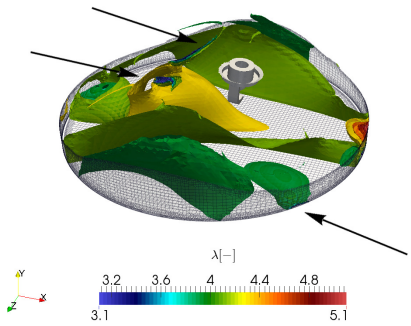

(e) Operating point C - iso surface

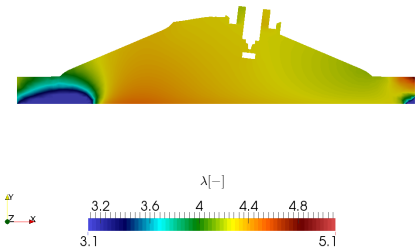

(f) Operating point C - tumble plane

Figure 6.18: *Influence of each operating condition on the air-fuel equivalence ratio distribution in the engine at* $20°bTDC$ *[83]*

6.3 The Adachi-Price Flash Boiling Evaporation Model

The model is based on the methodology proposed by Adachi and Price [92] and it was specifically implemented into the LibICE framework for the sake of this research activity. Within this context, the flash boiling simulations which are going to be discussed in this chapter were carried out by employing such specific mechanism. More in detail, the model accounts for heat transfer from the superheated droplet and its surrounding environment under physical assumptions similar to those of the Adachi-Rutland proposition. In particular, it is required that:

- the droplets are spherical;
- the droplet surface temperature is equal to the fuel saturation temperature at superheated conditions;
- the flash-boiling activity is modeled as external flash-boiling.

As it is shown in Fig.6.19 under superheated conditions the global evaporation rate is computed by the model as the sum of two contributions which are the *subcooled evaporation term*, M_{sc} and the *superheat evaporation term*, M_{sh}. The former is driven by the heat transfer from the surrounding gas to the droplet surface while the latter is due to the heat transfer from the droplet interior.

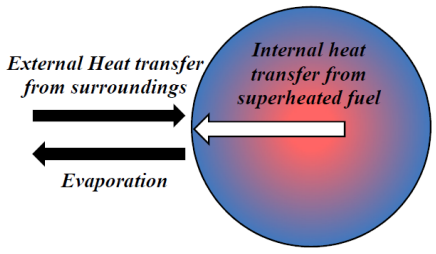

Figure 6.19: *Schematic of heat-transfer at droplet temperatures above and below the boiling temperature of the fuel [92]*

The M_{sc} term is computed by the model according to Eq.6.5 where A is the surface area of the droplet, P is the ambient pressure, Sh the Sherwood number, D_i the binary diffusive coefficient, T_f is the vapor film temperature (assumed as the average between the temperature values of the droplet and the surrounding gas), R_f is the specific gas

constant of the vapor film, D the droplet diameter while P_v and P_s respectively represent the partial vapor pressure in the computational cell and the saturation pressure of the fuel.

$$\frac{dM_{sc}}{dt} = AP\frac{ShD_i}{T_f R_f D}\ln\left(\frac{P-P_v}{P-P_s}\right) \tag{6.5}$$

The superheat M_{sh} contribution is calculated according to the same methodology proposed by the Adachi-Rutland model [11, 125] which was described in the previous chapters.

The total evaporation rate M_t is then calculated as the sum of the subcooled and superheat terms according to Eq.6.6.

$$\frac{dM_t}{dt} = \frac{dM_{sc}}{dt} + \frac{dM_{sh}}{dt} \tag{6.6}$$

6.4 Implementation of the Nagaoka-Kawamura Dynamic KHRT Secondary Breakup Model

In the context of this work, with the aim to define a predictive spray numerical methodology the KHRT secondary breakup mechanism proposed by Nagaoka and Kawamura [70] was investigated and implemented into the LibICE framework. Under the classic definition of the model the C_{RT} term is considered as a fixed parameter for each spray case. As a consequence, continuous recalibrations from the user may be needed when changing the simulated operating conditions of the spray. Low-evaporating cases such as the Spray G3 which is characterized by an almost atmospheric ambient pressure were proven to be particularly sensitive in this regard. Such a condition is related to a low value of the ambient density that in turn holds high influence in the decreasing of the Weber gas number (We_g) of the spray which may fall considerably below the range of validity of the catastrophic breakup regime. As a consequence, even small variations of the operating conditions would require a significant recalibration of the C_{RT} parameter for the model to still consistently perform the RT breakup. On the contrary, for high-evaporating GDI cases (such as G1, G4, G7) with an average Weber gas number approaching that of the literature catastrophic breakup regime the model performs

better with little necessity of parameter tuning activity.

The KHRT approach of Nagaoka and Kawamura was specifically thought to ensure spray-droplet consistency. That is, the aim was to have a breakup mechanism which is consistent both for a droplet in a spray plume or in isolated conditions [70]. Equations for the main B_0, B_1 and C_{RT} model parameters were proposed on the basis of breakup studies of an isolated droplet in an uniform flow and adjusted so that the KHRT method could match the correlations of total breakup time proposed by Pilch and Erdman [88] as it is shown if Fig.6.20.

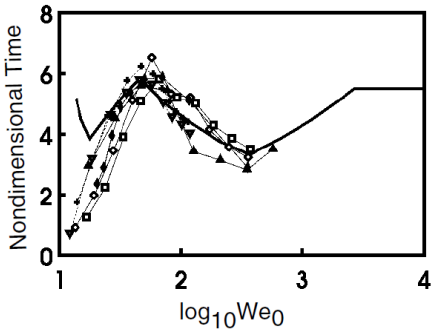

Figure 6.20: *Droplet total breakup time, correlation of Pilch-Erdman (solid line) against Nagaoka-Kawamura model (symbol) [70]*

According to the proposed approach droplets are subjected to enlargement before the secondary breakup takes place with Weber and Ohnesorge numbers becoming function of the deformed spheroidal radius *a* so that KH equations for drop size change and the radius of the stripped parcel are respectively computed as reported in Eq.6.7-6.8.

$$\frac{dD}{dt} = -\frac{D - D_{KH}}{\tau_{KH}} \tag{6.7}$$

$$a_{strip} = B_0 \lambda_{KH} \tag{6.8}$$

The KH τ_{KH} breakup time is computed as in the standard KH model and the B_1 constant is calculated according to Eq.6.9

$$B_1 = 161.7\sqrt{\frac{\rho_g}{\rho_l}} min\left[1.0, \left(\frac{15}{We_{g,a}}\right)^{0.8}\right] \tag{6.9}$$

while the mathematical formulation for B_0 is shown in Eq.6.10

$$B_0 = 0.61 \left[1.0 - 1.43 \left(\frac{\rho_g}{\rho_l} \right)^{0.2} exp \left(\frac{-We_{g,a}}{10} \right) \right] \tag{6.10}$$

The fundamentals of the competing RT mechanism are the same if compared to the classic KHRT model with only the C_{RT} parameter dynamically varying according to Eq.6.11 so that the trend of the Pilch-Erdman adimensional total breakup time as a function of the droplet Weber gas number could be reproduced.

$$C_{RT} = max \left(1.0, 0.11 \sqrt{We_{g,a}} \right) \tag{6.11}$$

It can be noticed that the value of B_1 decreases with the ambient density and with an increase of the Weber gas number of the droplet. While an enhanced KH breakup activity under low-evaporating conditions is promoted at the same time the parcel mass stripping activity appears to be overpredicted for high-pressure and high-evaporating sprays. As such, when tested on the different Spray G operating points the model proved to be completely predictive only for conditions such as G2, G3 and those with potentially lower ambient density and Weber gas number. Generally, during this research activity it was observed that for GDI sprays a threshold separating low-evaporation from high-evaporation injections could be defined on the basis of the ambient density. If the user is adopting a separated characterization of the KH mechanism between atomization and secondary breakup the ambient density value for which the required $B_{1,atom}$ term is smaller than the B_1 parameter can be considered as the reference threshold below which the Nagaoka-Kawamura KHRT modeling could provide a predictive behavior.

Within this context, a hybrid approach is proposed so that G1 and G7 operating points were simulated with a standard KHRT model under a constant setup while G2 and G3 sprays were tested with the dynamic Nagaoka-Kawamura KHRT approach. As far as the atomization phase is concerned the main model constants were the same for each condition and based on the general values proposed for the Pilch-Erdman mechanism. Tab.6.3 and Tab.6.4 report the main characteristics for the low-density and high-density cases respectively.

Table 6.3: *Low-density (G2, G3) spray model main parameters*

Mesh	0.5 mm, no AMR
Atomization	Pilch-Erdman
Breakup	Nagaoka-Kawamura KHRT
B_1	Dynamic
C_{RT}	Dynamic
$C_{1,\varepsilon}$	1.55
Plume cone angle (G2)	35°
Plume cone angle (G3)	22°
Drill angle	37°

Table 6.4: *High-density (G1, G7) spray model main parameters*

Mesh	0.5 mm, no AMR
Atomization	Pilch-Erdman
Breakup	KHRT
B_1	23
C_{RT}	0.35
$C_{1,\varepsilon}$	1.55
Plume cone angle	18°
Drill angle	37°

The setup of the remaining sub-models was kept consistent and equal to that of the previous chapters. The only relevant difference consisted into the adoption of the newly implemented Adachi-Price evaporation model for the G2 flash boiling condition.

6.4.1 Spray G Vessel Results

Concerning the reference Spray G1 condition Fig.6.21(a) reports the validation of the computed axial vapor penetration against experimental data available from the ECN6 Workshop. Results show a good prediction of the different profiles and the liquid extinction length time with reference to the low PLV threshold. Fig.6.21(b) and Fig.6.21(c) further confirm the accuracy of the model by respectively showing a well predicted axial vapor penetration trend and a correct entrainment nearby the injector nozzle during the whole simulation duration.

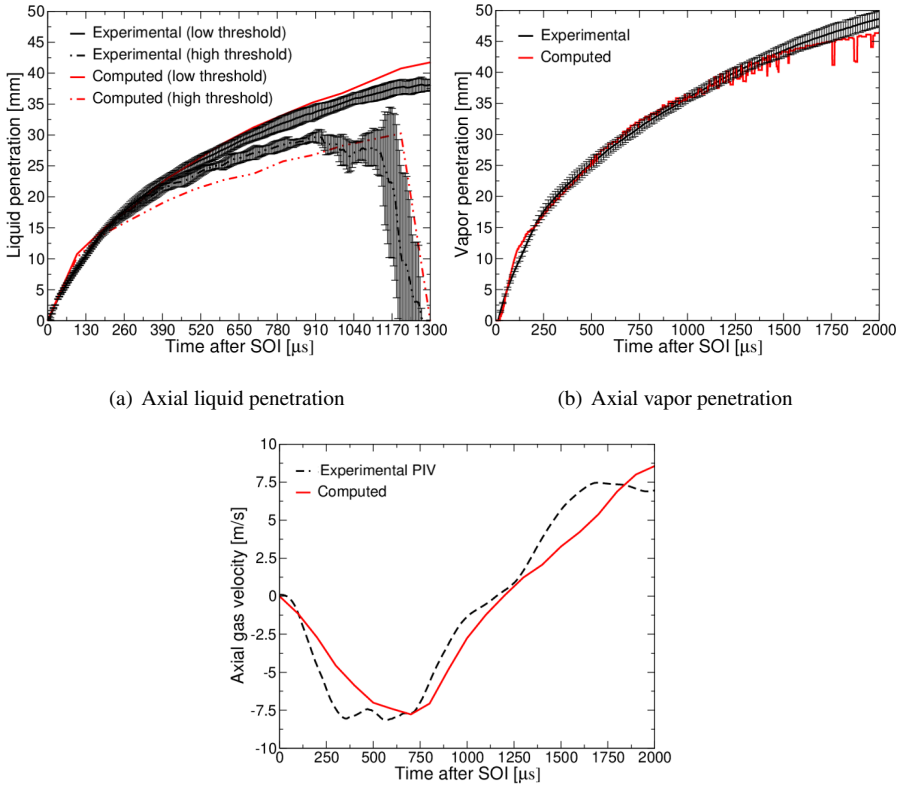

(a) Axial liquid penetration

(b) Axial vapor penetration

(c) Centerline axial velocity

Figure 6.21: *G1 condition, validation of computed axial spray penetrations and centerline velocity*

Finally, as shown by PLV maps in Fig.6.22(a)-6.22(c) the accurate prediction of these mandatory spray parameters reflects into a coherent numerical spray morphology both during and after the injection phase.

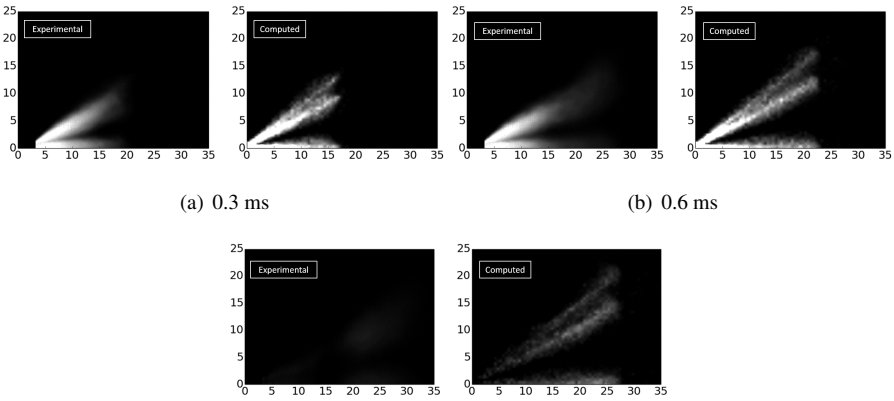

(a) 0.3 ms (b) 0.6 ms

(c) 0.9 ms

Figure 6.22: *G1 condition, PLV maps, comparison between experimental results and computed spray. Range is* $0 - 0.01 \frac{mm^3}{mm^2}$*, axes dimensions reported in mm*

The G7 operating point was tested and validated as well under a constant setup thanks to the latest available ECN6 data. The G7 condition is characterized by a high value of ambient density leading to a spray evaporation rate which is typical of late injection events in modern GDI engines. Fig.6.23 shows that the model is predictive enough to provide an accurate reproduction of the axial vapor penetration without requiring interventions from the user in terms of parameters calibration.

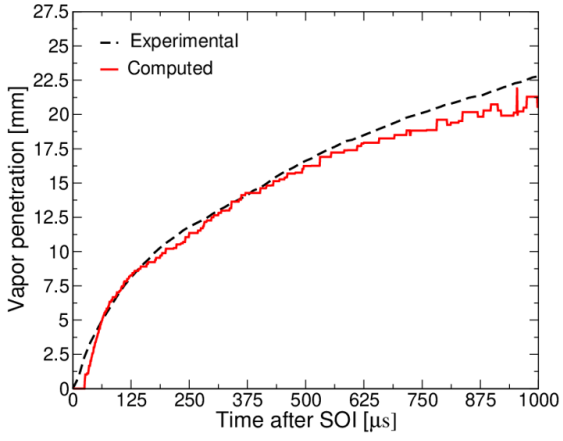

Figure 6.23: *G7 condition, comparison between computed and experimental axial vapor penetrations*

Moreover, the expected fast spray collapse typical of a late injection condition is also numerically predicted as it is possible to observe from the comparison between the computed G1 and G7 PLV spray morphologies which are reported in Fig.6.24(a)-6.24(c) for different simulation times.

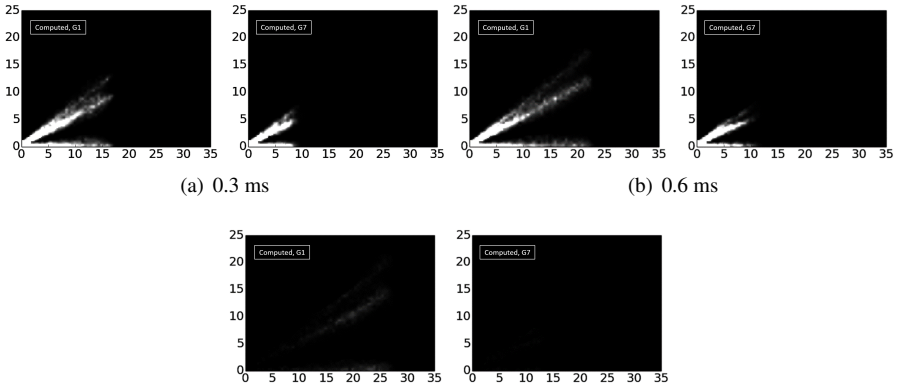

(a) 0.3 ms (b) 0.6 ms

(c) 0.9 ms

Figure 6.24: *PLV maps, comparison between computed G1 (left) and computed G7 (right) results. Range is* $0 - 0.01\frac{mm^3}{mm^2}$*, axes dimensions reported in mm*

The proposed results represent a further confirmation of the fact that GDI sprays characterized by typically "high-evaporating" conditions appear to be less sensitive to the variations of the main adopted secondary breakup model parameters.

On the other hand, G2 and G3 simulations were performed with the proposed dynamic KHRT secondary breakup model. Fig.6.25 shows the validation of the computed axial vapor penetration for the G2 case.

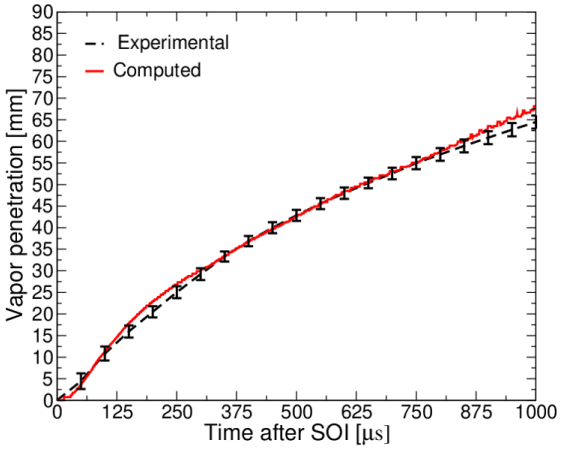

Figure 6.25: *G2 condition, comparison between computed and experimental axial vapor penetrations*

The combination between the dynamic KHRT secondary breakup model and the Adachi-Price flash-boiling evaporation mechanism allowed for a good matching between experimental and numerical axial vapor penetration trends. Moreover, the accuracy of the computed evaporation rate was further confirmed by the analysis of the axial PLV profiles and the spray morphology by means of the PLV maps as it is respectively shown in Fig.6.26(a)-6.26(c) and Fig.6.27(a)-6.27(c). In particular, the spray morphology highlights the effects due to the liquid fuel flash vaporization which leads to an increase of the PCA value along the plume length and to a strong collapse of the spray jets.

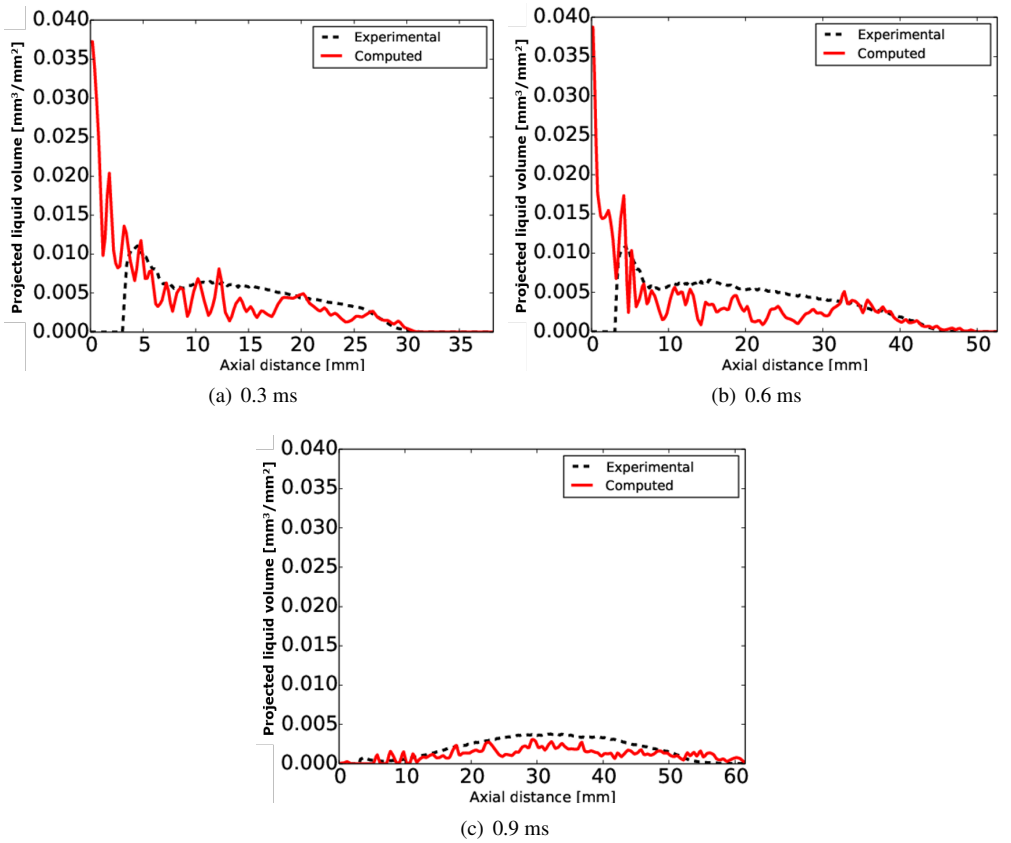

(a) 0.3 ms

(b) 0.6 ms

(c) 0.9 ms

Figure 6.26: *G2 condition, axial PLV profiles, comparison between experimental results and computed spray*

Concerning the G3 operating point, Fig.6.28(a) reports the comparison between computed and experimental axial liquid penetrations both for low and high threshold values. Results show that during the injection phase the numerical profiles match the experimental trends with a good level of accuracy. After the end of the injection (EOI)

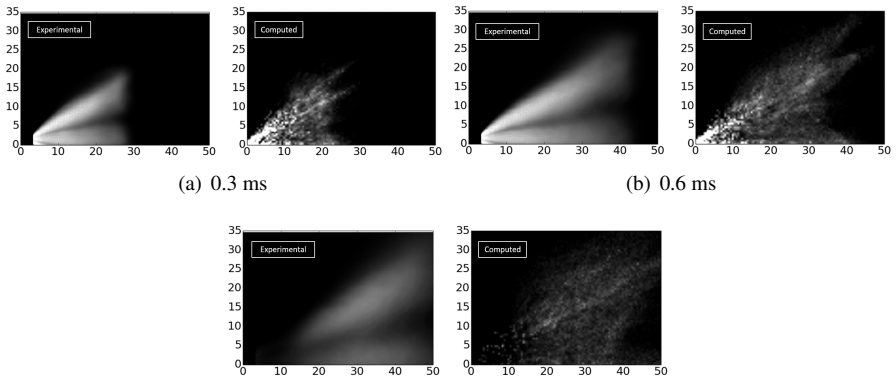

(a) 0.3 ms (b) 0.6 ms

(c) 0.9 ms

Figure 6.27: *G2 condition, PLV maps, comparison between experimental results and computed spray. Range is* $0 - 0.01 \frac{mm^3}{mm^2}$*, axes dimensions reported in mm*

a slight numerical overestimation of the axial liquid penetration is observed but the consistency of the spray model is ensured by the analysis of the axial vapor penetration proposed in Fig.6.28(b). The vapor profile is indeed well captured up to the simulation end-time with the computed fuel evaporation process which was verified to correctly be mixing limited.

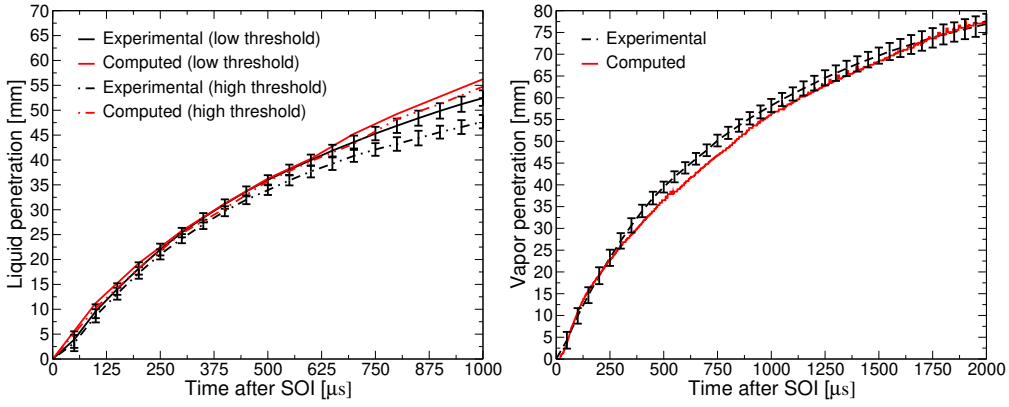

(a) Liquid (b) Vapor

Figure 6.28: *G3 condition, comparison between computed and experimental axial spray penetrations*

Fig.6.29(a)-6.29(c) further assess previous observations by showing the evolution of the in-plume liquid distribution at early injection (0.1 ms), late injection (0.5 ms) and post-injection (0.9 ms) times. Such investigation is based on the axial evolution over time of the projected liquid volume Eulerian field. For each timeframe it is possible to observe that the computed profiles are coherent with the experimental evolution at

both low axial distances (where a high quantity of in-plume resident liquid is expected nearby the injector nozzle) and high axial distances (where secondary breakup and liquid evaporation are the dominant physical phenomena).

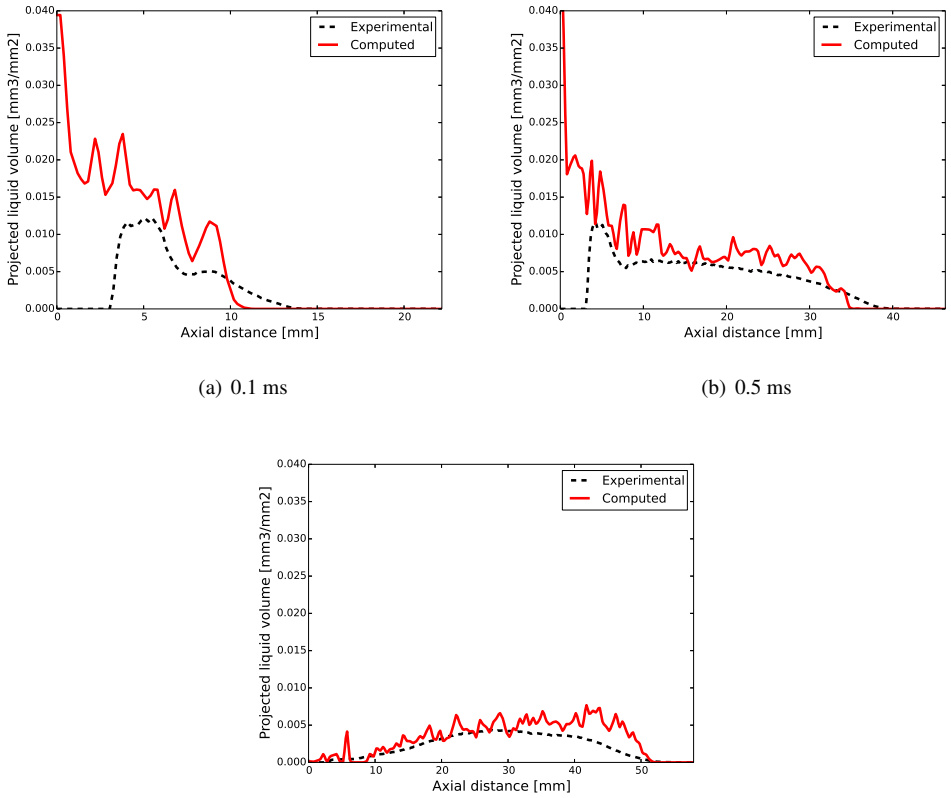

(a) 0.1 ms

(b) 0.5 ms

(c) 0.9 ms

Figure 6.29: *G3 condition, axial PLV profiles, comparison between experimental results and computed spray*

Finally, in Fig.6.30(a)-6.30(c) experimental and numerical spray morphologies are compared at different times during (0.3 ms and 0.6 ms) and after (0.9 ms) the injection process on the basis of the projected liquid volume field. For each timeframe the computed profiles show a good matching both axially and radially, further demonstrating the potential of the proposed numerical setup.

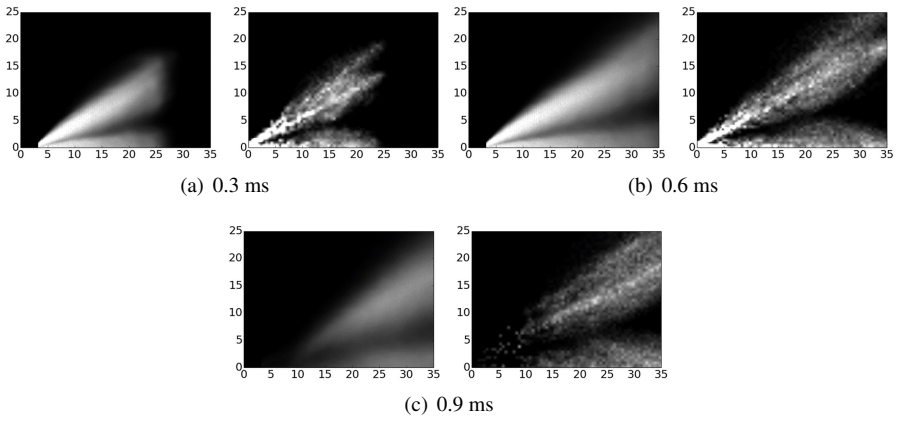

(a) 0.3 ms (b) 0.6 ms

(c) 0.9 ms

Figure 6.30: *G3 condition, PLV maps, comparison between experimental results and computed spray. Range is* $0 - 0.01 \frac{mm^3}{mm^2}$*, axes dimensions reported in mm*

6.5 Conclusions

In this chapter weak points of the previous numerical setup in terms of spray morphology and in-plume liquid distribution were addressed. Moreover, the idea behind the new proposed models also consisted into providing the user numerical configurations which could be as predictive as possible while requiring a low effort in terms of calibration and setting from case to case.

As a first step the dedicated Huh-Gosman atomization model was discarded so that both primary and secondary breakup phases could be modeled within a single setup. Such an option, which is already available in literature with the classic KHRT secondary breakup model, was found out during this research work not to be optimized for the numerical reproduction of modern multi-hole GDI sprays. Within this context, if the KHRT model is also adopted for atomization prediction in a single-model numerical configuration only the stripping breakup phase (KH) is allowed to take place within the liquid core length while the catastrophic contribution (RT) is neglected. This is because the RT contribution would cause too strong and fast droplet diameter reduction which would lead to an inaccurate computation of axial spray penetration, evaporation rate, entrainment and morphology. Still, a major weakness of this approach consists into the fact that a single B_1 model constant is employed for describing the specific characteristic times both of atomization and secondary breakup. It appears in fact clear that the model should instead act separately on atomization and secondary breakup so that

the different motion conditions to which injected and far-field parcels are respectively subjected could be correctly taken into account. As a consequence, in this chapter a decoupled approach was proposed with two different B_1 model constants specifically dedicated to primary and secondary breakup. The model was validated both in vessel on the low-evaporating Spray G3 operating point and under transient conditions by simulating a full-cycle of the optical access Darmstadt Engine coupled with the ECN Spray G injector operating under a configuration very close to the ECN G3 condition. Results showed that the already good achievements in terms of liquid/vapor axial penetrations were mantained while also significant improvements in terms of spray morphology (PLV maps) and in-plume liquid distribution (axial PLV profiles) were achieved. Moerover, considering the accuracy of the proposed gas exchange results the Darmstadt Engine-related simulations could represent a preliminary investigation of the mixture formation process and thus a starting point for the study of the Spray G under real engine conditions which is a topic that will in fact be of great importance in future ECN activities. The introduction of a second B_1 parameter could appear as a step towards numerical complication. However it must be remembered that the proposed model is just a single parameter-replacement solution compared to more complex approaches based on a dedicated atomization model. In this regard, solutions such as the Huh-Gosman mechanism were demonstrated not to provide any significant advantage in terms of numerical accuracy. In any case, thanks to what was observed on the ECN Spray G injector an estimated range of validity for the $B_{1,atom}$ parameter was provided in this chapter as a basis for potential future investigations on GDI sprays.

Another proposed solution consisted into the adoption of the Pilch-Erdman model as a main mechanism of diameter reduction and atomization for the parcels within the liquid core length. It is an approach based on the concept of total breakup time which is usually adopted in literature to numerically reproduce the secondary breakup phase of a spray in a rather simplified manner and without taking into account the phenomenon of child parcel stripping. Considering that the structure of the Lagrangian spray is numerically reproduced under the same constraints within or out of the core length, the capability of the model to provide a smooth drop diameter reduction rate with almost no required tuning activity was seen as a potential alternative for modeling the atomization

process of GDI sprays. Within this context, validation was carried out in vessel on both G1 and G3 operating points showing no required calibration from case to case and an easy coupling with the KHRT secondary breakup model which led to overall accurate spray results.

To further expand the work in the direction of reduced setup complexity and tuning activity a predictive version of the KHRT secondary breakup model based on the literature proposition of Nagaoka-Kawamura was specifically implemented into the LibICE numerical framework. The B_0, B_1 and C_{RT} parameters become function of the density ratio and the parcel Weber gas number so they dynamically vary with the motion regime of each single parcel and with the global operating conditions of the spray. The proposed configuration provided good overall spray results both for the low-evaporating G3 and the flash boiling G2 operating points. The latter condition was well simulated also thanks to the literature-based Adachi-Price flash boiling evaporation model which was accordingly implemented into the LibICE. Given that the Spray G operating points characterized by low values of ambient density and Weber gas number proved to be the most sensitive and complex in terms of required numerical calibration, the provided predictive setup could be considered as a potentially easier albeit accurate alternative for the modeling of early injection events in modern GDI engines.

CHAPTER 7

Implementation of the NTC Collision Model into the LibICE Framework

In this chapter the No-time-counter (NTC) droplet collision model proposed by Schmidth and Rutland [102] was implemented into the LibICE framework and validated on the ECN Spray G1 and G3 operating conditions. Collision between liquid droplets represents an important physical phenomenon which should influence both spray morphology and evaporation rate. More in detail, effects are particularly visible in the dense spray region nearby the injector nozzle where there is a high number od droplets per unit volume and thus a high probability of collision [19]. Collision is heavily dependent on the difference between droplets velocities which in turn are functions of multiple phenomena such as deceleration, breakup, drag and liquid evaporation rate. It appears thus clear that the collision process can characterize injection events with different degrees of intensity according to main typical operating parameters such as injection pressure, ambient pressure, temperature and viscosity [19]. As it is shown in

Fig.7.1 the possible collision outcomes can be divided into five main events which are *bouncing, coalescence, reflexive separation, shattering* and *stretching separation* [19].

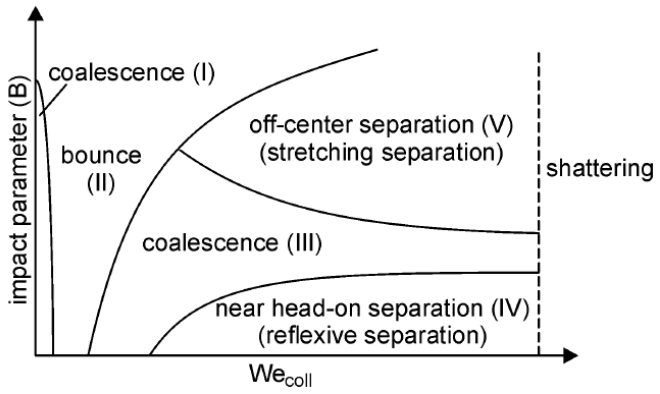

Figure 7.1: *Schematics of possible droplet collision regimes [19]*

As it can be observed the different regimes depend on two main parameters which are the *Weber collision number* (We_{coll}) and the dimensionless impact parameter *B*. More in detail, the former is defined according to Eq.7.1 where ρ_l is the liquid density, U_{rel} is the relative velocity of the drops, D_2 the diameter of the smaller drop and σ represents the surface tension.

$$We_{coll} = \frac{\rho_l D_2 U_{rel}^2}{\sigma} \tag{7.1}$$

The definition of the *dimensionless impact parameter* is reported in Eq.7.2.

$$B = \frac{2X}{D_1 + D_2} \tag{7.2}$$

The D_1 term is the diameter of the larger drop while X represents an *impact collision parameter* defined as the projection of the distance between the centers of the two drops in a normal direction compared to the relative velocity [19], as it is also displayed by Fig.7.2.

The dimensionless impact quantity *B* can vary between 0 and 1 in value with the former representing complete head-on collision between two droplets and the latter standing for tangential (grazing) collision [19]. Along with these parameters other mandatory quantities are required to correctly define the characteristics of a collision process such as the Reynolds number Re_{coll} and the droplet diameter ratio Δ, respec-

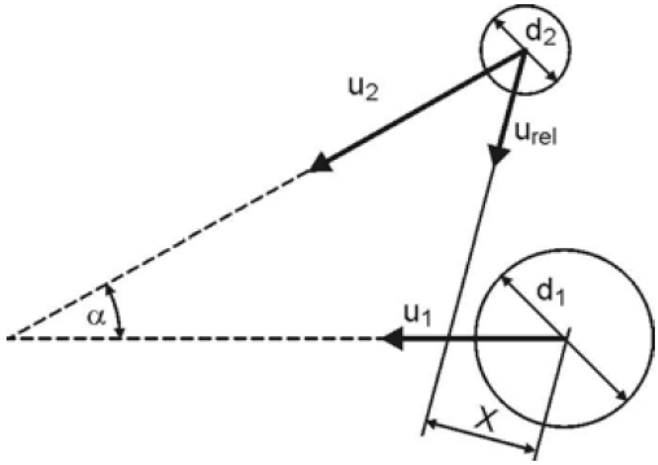

Figure 7.2: *Illustration of the impact parameter X definition [19]*

tively introduced by Eq.7.3 and Eq.7.4.

$$Re_{coll} = \frac{\rho_l D_1 U_{rel}}{\mu_l} \tag{7.3}$$

$$\Delta = \frac{D_2}{D_1} \tag{7.4}$$

The term μ_l represents the dynamic viscosity of the liquid phase while the relative velocity U_{rel} is calculated according to Eq.7.5 where α is the collision angle between the trajectories of both droplets.

$$U_{rel} = \sqrt{U_1^2 + U_2^2 - 2U_1 U_2 cos\alpha} \tag{7.5}$$

However, not all the different motion regimes which are reported in Fig.7.1 are taken into account for collision by the available CFD models because an evaluation of the related effects by means of comparisons with dedicated experimental data is basically not possible. In fact, parameters such as droplet size and velocity are directly dependent on such a wide range of physical phenomena like breakup and evaporation that it is virtually impossible to identify the effects that would be solely due to collision [19]. Moreover, despite its physical relevance, collision is often numerically overlooked in CFD also because of the high required computational times since almost all the models operate based on an iterative check for collision probability which is performed on

every parcel within the computational domain. As a consequence, already available classic literature models such as that of O'Rourke [74] and Nordin [72] take into account only two main physical collision outputs which are *permanent coalescence* and *stretching separation* [19].

With reference to multi-hole GDI sprays it can be straightforward to understand that early injection, low-evaporating cases may be characterized by a very high number of parcels in the computational domain. While collision could hold significative influence under these specific operating conditions, inefficiencies of classic parcel-to-parcel iterating mechanisms in terms of required computational time are likely to be faced during simulations. To assess this aspect, with reference to the ECN Spray G injector geometry the radially sampled spray SMD evolutions at 15 mm downstream of the injector nozzle at times of 0.3 ms and 0.6 ms are reported in Fig.7.3(a)-7.3(b) for the baseline G1 condition. Simulations were carried out both without a collision model and with the employment of the Nordin mechanism. This preliminary analysis allowed to understand if droplet collision was numerically worth to be numerically considered when applied to the ECN Spray G injector.

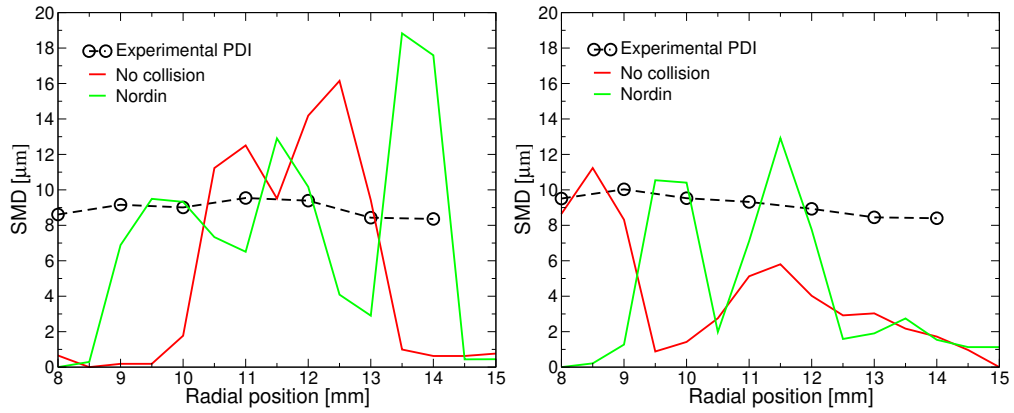

(a) 0.3 ms (b) 0.6 ms

Figure 7.3: *G1 condition, radial PDI for liquid droplet velocity, experiments against simulations without collision and with the Nordin model*

It is possible to observe that under early injection conditions droplet collision allowed to computed SMD values closer to the experimental profile even for radial positions far from the plume center. The physical droplet-to-droplet interaction basically allowed for a more uniform radial distribution of the spray compared to what

was achieved without employing a collision model. At higher times closer to the EOI threshold a less dense parcel distribution is expected because of liquid evaporation. As a consequence, collision should have less impact on the spray. Nevertheless higher SMD values are observed on average along the sampled radial lenght, fact which could be considered as a direct result of the physical droplet coalescence process. Given that any other component of the numerical setup was kept constant between the two reported cases it could be inferred that the adoption of a collision model can influence to a certain degree the numerical evolution of a modern multi-hole GDI injection process such as that of the Spray G injector. The investigation of numerical approaches which could take into account the effects of collision on GDI sprays while reducing the required computational time is thus justified.

Within this context, the literature-based NTC collision model [102] was implemented into the numerical LibICE framework with the aim to provide a compromise between accuracy and calculation time. NTC, O'Rourke and Nordin models were then compared to each other by carrying out G1 and G3 simulations and by investigating parameters such as total required computational time, computed axial vapor penetration and average spray SMD. Observed weaknesses of the NTC model were then discussed and a modified version was proposed with the aim to provide the best possible compromise between an accurate numerical spray reproduction and the minimization of the required computational time.

The organization of the chapter is thus as follows:

- at first the main features of the newly implemented NTC model are described;
- the model is then tested on the G1 condition with results that are compared to those achieved without a collision model and with both O'Rourke and Nordin approaches;
- on the basis of the observed behavior of the different methodologies a modified NTC model is proposed and tested on ECN Spray G1 and G3 cases. More in detail, the aim of the changes was to ensure spray results as close as possible to those of the Nordin model (which appeared to be the most accurate method both with reference to G1 experimental data and the simulation without collision) while

retaining the computational efficiency of the original NTC mechanism.

7.1 The NTC Collision Model

Compared to the O'Rourke model the original form of the NTC approach provides an analytical alternative in the way parcels are considered and eventually selected for collision while after a pair of parcel has been chosen there is no difference in the way the subsequent collision process is physically managed. Rather than iterating on each parcel the NTC method sorts the parcels for all the computational cells so that a list of every parcel in a given cell is always available and updated at every time-step. Within this context, the model checks the parcel population of each cell with the aim to evaluate which approach between a direct (similar to that of O'Rourke) or a NTC collision calculation method is the fastest and less demanding in terms of required computational time. Considering a specific number of droplets *N* contained into a computational cell the probability of all possible collisions M_{coll} is given by Eq.7.6 [102] where N_p is the number of parcels in the cell, V is the cell volume, $U_{i,j}$ the relative velocity between the two droplets, q represents the number of droplets in each parcel and Δt stands for the adopted time-step.

$$M_{coll} = \frac{1}{2} \sum_{i=1}^{N_p} q_i \sum_{j=1}^{N_p} q_j \frac{U_{i,j} \sigma_{i,j} \Delta t}{V} \tag{7.6}$$

The term $\sigma_{i,j}$ represents the collision cross section of the two parcels and it is defined according to Eq.7.7 where r is the drops radius.

$$\sigma_{i,j} = \pi \left(r_i + r_j \right)^2 \tag{7.7}$$

The direct evaluation of this summation leads to a computational cost in the order of N_p^2. According to the NTC approach this is avoided by pulling a specific term out of the summation with Eq.7.6 which is thus rewritten in the form of Eq.7.8.

$$M_{coll} = \frac{\left(qU\sigma\right)_{max} \Delta t}{2V} \sum_{i=1}^{N_p} q_i \sum_{j=1}^{N_p} \frac{q_j U_{i,j} \sigma_{i,j}}{\left(qU\sigma\right)_{max}} \tag{7.8}$$

The term $\left(qU\sigma\right)_{max}$ must be chosen to be sufficiently large so that the mathematical

relation expressed in Eq.7.9 holds.

$$\frac{q_j U_{i,j} \sigma_{i,j}}{(qU\sigma)_{max}} < 1.0 \tag{7.9}$$

Within this context, Eq.7.8 can again be rewritten as Eq.7.10 where the quantity M_{cand} is defined according to Eq.7.11.

$$M_{coll} = \sum_{i=1}^{\sqrt{M_{cand}}} q_i \sum_{j=1}^{\sqrt{M_{cand}}} \frac{q_j U_{i,j} \sigma_{i,j}}{(qU\sigma)_{max}} \tag{7.10}$$

$$M_{cand} = \frac{N_p^2 \, (qU\sigma)_{max} \, \Delta t}{2V} \tag{7.11}$$

Eq.7.10 is mathematically equivalent to Eq.7.6 but now the summation is evaluated on M_{cand} terms instead of N_p^2. The M_{cand} parameter thus represents the number of pairs actually selected for collision, each one chosen at random and with replacement. Since the M_{cand} term is linearly proportional to N_p the NTC rearrangement shows that a considerably reduced computational time should be required for numerical collision.

For the NTC approach to be efficient it thus appears clear that the user must make a sensible choice of the $(qU\sigma)_{max}$ parameter. Such a value may change from cell to cell so, for it to always correspond to the in-cell optimum, in the present work an automatic evaluation at each time-step has been implemented. Still, if the M_{cand} parameter of a cell is greater than the $\frac{N_p^2}{2}$ quantity a direct calculation may prove to be a more efficient approach which means that all the parcels within a given cell are scanned for possible collision. This is the classic approach which is adopted by the O'Rourke model with however a difference which consists into the fact that it is already known if a parcel is or not within the computational cell.

After a pair of parcels has been selected they collide if a deviate r chosen in the interval $[01)$ satisfies Eq.7.12 where q_g stands for the greater number of droplets between q_i and q_j.

$$r < \frac{q_g U_{i,j} \sigma_{i,j}}{(qU\sigma)_{max}} \tag{7.12}$$

Once the probability of collision is verified the physical phenomenon is modeled in

the same way as the classic O'Rourke method.

7.2 Validation of the NTC Model on the Spray G1 Operating Point

Every reported G1 simulation was performed on a 14 core Intel Xeon E5-2690 V4 CPU server with a computational grid of 0.5 mm without AMR and a time-step equal to $5e^{-7}$ seconds. Within this context, Tab.7.1 reports the required computational times for each tested condition.

Table 7.1: *Spray G1, required computational times*

Case	Computational time
No collision	~ 11 hours
O'Rourke	~ 17 hours
Nordin	~ 17 hours
NTC	~ 11.2 hours

As previously discussed, O'Rourke and Nordin models check for collision by means of an iterative scan through every spray parcel to search for possible colliding pairs. The difference between the two models stands in the process which verifies if the selected pair of parcels can effectively collide. More in detail, the O'Rourke mechanism requires the parcels to be in the same computational cell and then to satisfy a specific collision probability while the Nordin method can provide a collision outcome between parcels from different computational cells as long as the following conditions are satisfied [72]:

- the parcels are travelling towards each other;
- the travelled distance is larger than the distance between the parcels;
- the collision is verified to be physically possible within the time interval.

The required computational time is mainly influenced by the initial scanning activity while quality and physical properties of the computed spray appear to depend on the approach which is chosen to assess if selected pairs of parcels can collide or not. Within this context, reported similar values of required simulation time between O'Rourke and Nordin cases were to be expected.

On the other hand, the NTC collision model proved to be considerably faster since a list of the parcels in each cell is automatically sorted for every time-step and M_{cand}

pairs of parcels are actually selected for possible collision. Furthermore, if Eq.7.9 is not satisfied the model acts by means of a direct approach which is still faster than a conventional method because the parcels were already grouped and listed for each computational cell.

Fig.7.4 shows a validation of the computed axial penetration against available ECN6 experimental data respectively for cases without collision model, with the O'Rourke method, with the Nordin mechanism and with the implemented NTC model. It can be observed that the Nordin model provides the best axial vapor penetration trend which is the one closest to that of the G1 simulation without collision and to the experimental range. The two computed profiles are in fact consisten, with the Nordin case being characterized by a slightly higher axial vapor penetration which could be due to the momentum exchange of grazing colliding parcels and the formation of bigger, coalesced droplets within the spray plumes.

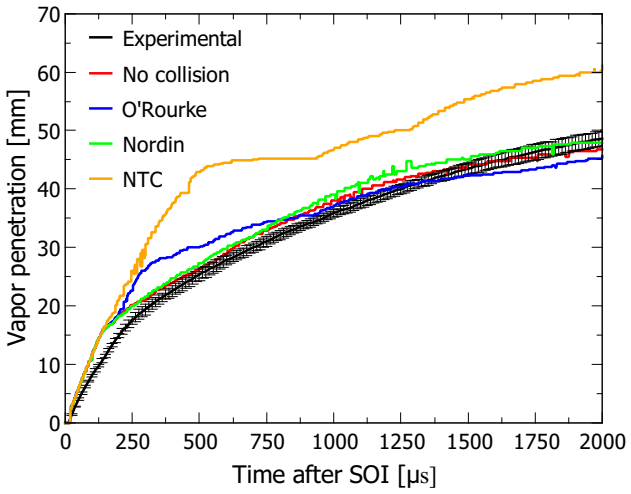

Figure 7.4: *G1 condition, validation of the computed axial vapor penetration profiles*

On the other hand, the O'Rourke simulation shows a distorted axial vapor penetration profile during the early phase of the injection event. This fact appears to be due to the collision probability methodology adopted by the model which leads to a collision event between parcels that should have not physically occurred if the conditions required by the Nordin model were to be taken into account. As a consequence, during the early injection phase when the average parcel diameter is still high in size

an overpredicted coalescence event takes place leading to high-mass and high-inertia droplets which axially penetrate more than it should be physically expected. The same phenomenon is observed with an even higher frequency for the NTC case probably as a consequence of the mathematical relation of Eq.7.12 which determines if two selected parcels can collide. Afterwards, O'Rourke and NTC models appear to behave in a similar fashion as it is demonstrated by the evolution over time of their axial vapor penetration profiles.

7.3 A Modified Version of the NTC Collision Model

The analysis which was carried out in the previous section demonstrated that the Nordin model is the one which appears to better predict the physics behind droplet collision phenomena taking place during the Spray G1 injection process. Still, its required computational time is predictably similar to that of the O'Rourke model while the new NTC approach provides a considerable advantage. Within this context, the final aim of the research was to employ a model which could ensure the low computational time of the NTC mechanism while providing the physical accuracy of the Nordin method. A modified NTC collision approach was thus proposed, tested and implemented into the LibICE framework. The new model adopts the same mechanism of the original NTC proposition to numerically group and list the parcels in each computational cell thus minimizing the required scanning computational time. Then, a pair of parcels is selected for collision if the physical constraints of the Nordin model are satisfied. A critical point of such an approach could be moved with reference to the fact that the parcels are listed cell by cell before exploiting possible collisions. This fact means that, coherently with the original NTC mechanism, only parcels within the same computational cell can collide with each other by means of the selection of M_{cand} pairs. However, according to the Nordin model collision events should be expected also from parcels which are not in the same computational cell. As a consequence, the modified NTC approach would not take into account all the possible collision events within a given time-step which should instead happen according to the theory proposed by Nordin. To compensate for this numerical limitation a higher number of in-cell collisions for each time-step was promoted for the modified NTC model by specifically tuning the value

of the C_2 constant which influences the probability of collision $Coll_{prob}$ according to the mathematical formulation originally proposed by the method of Nordin [72] and reported in Eq.7.13.

$$Coll_{prob} = \left(\frac{r_1 + r_2}{max\left(r_1 + r_2, \Delta_{12}\right)} \right)^{C_1} e^{\frac{-C_2|\alpha_0 - \beta_0|}{\Delta t}} \tag{7.13}$$

The r_1 and r_2 terms are the radius values of the two parcels, Δ_{12} is the minimum distance between the two trajectories, C_1 is the spatial probability decay outside of the cylinders swept by the droplets, C_2 is the temporal probability decay while α_0 and β_0 represent specific collision times which vary in the interval $[0, \Delta t]$. The Δt quantity stands for the simulation time-step. Within this context, a potential compensation to the numerical limitation of the NTC sampling method when coupled to Nordin methodology for collision modeling was proposed by means of a sensitivity analysis carried out on the C_2 parameter. This specific investigation led to the reduction of the temporal probability decay from a value of 0.3 (iterature reference value for the Nordin model) to 0.05 allowing for an increase of the $Coll_{prob}$ parameter and thus of the collision probability within each computational cell for the modified NTC mechanism.

The approach was then validated on the Spray G1 case in terms of computed axial vapor penetration and SMD with the results that are respectively reported in Fig.7.5 and Fig.7.6.

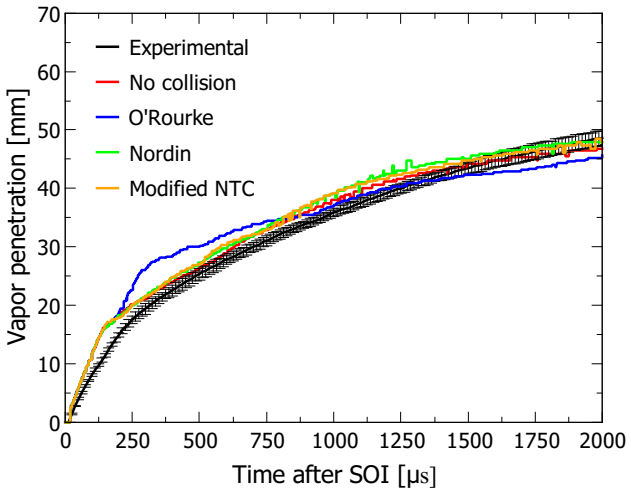

Figure 7.5: *G1 condition, validation of the modified NTC model based on the axial vapor penetration*

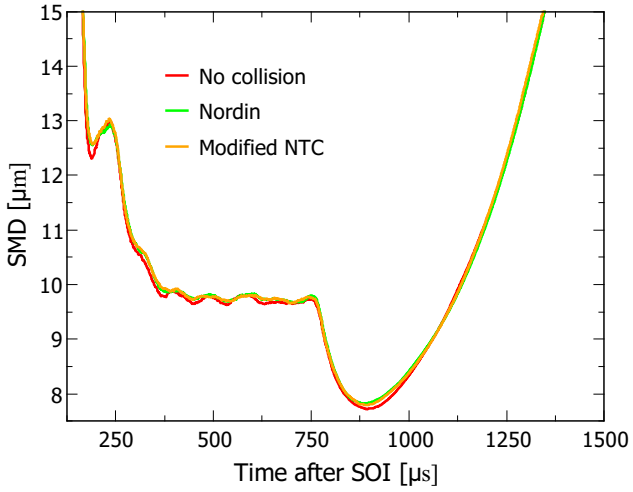

Figure 7.6: *G1 condition, validation of the modified NTC model based on the computed SMD*

The modified NTC case well matched the Nordin simulation in terms of predicted axial vapor penetration and SMD thus showing considerable improvements in terms of accuracy if compared to what was achieved with the original model. At the same time the statistic approach for the selection of parcel pairs minimized the required computational time thus granting the same considerable adavantage over other collision models which was observed for the original NTC mechanism and reported in Tab.7.1.

Further validation was carried out by performing G3 simulations without a collision model, with the classic Nordin approach and with the modified NTC mechanism. Computed axial vapor penetration profiles and spray SMD values are respectively shown in Fig.7.7 and Fig.7.8.

Once more the modified NTC model allowed to match the accurate physical results which could be achieved with the Nordin approach. Moreover, PLV maps and axial PLV profiles were computed at simulated times respectively equal to 0.3 ms and 0.6 ms. Fig.7.9 shows a comparison of the computed PLV-based spray morphologies at 0.3 ms for the standard G3 case (left), for the Nordin collision simulation (center) and for the modified NTC calculation (right).

No significant differences in spray morphology were observed for the three different G3 cases as it was also possible on the basis of the previous analysis of the computed axial vapor penetration profiles. In fact, given the low-evaporating condition of the

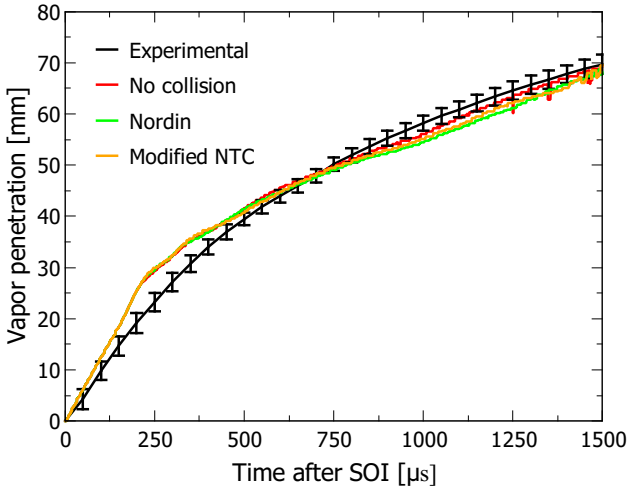

Figure 7.7: *G3 condition, validation of the modified NTC model based on the axial vapor penetration*

setup any important discrepancy in the behavior of the liquid would directly affect the evolution of the axial vapor profile over time. Still, a more careful look can show a slightly enhanced plume-to-plume interaction at the jet tips for both collision simulations. This phenomenon can be seen as a direct consequence of the in-jet droplet grazing collision process which allows for a radial enlargement of the spray plumes as expected (Fig.7.3(a)).

Fig.7.10(a)-7.10(c) also demonstrate that the adoption of a collision model does not alter the in-plume axial liquid distribution with the computed axial PLV profiles always matching available experimental data at a time equal to 0.3 ms.

Similar conclusions can be inferred by investigating PLV maps (Fig.7.11) and axial profiles (Fig.7.12(a)-7.12(c)) at 0.6 ms. For the Spray G injector it thus appears clear that the biggest impact due to the adoption of a collision model is related to an increase of the average spray SMD value with also a slightly higher liquid dispersion around each plume axis due to a better numerical prediction of drop-to-drop physical interaction.

Moreover, Fig.7.12(a)-7.12(c) show that the phenomenon of droplet coalescence seems to lead to the plume core being slightly richer in liquid neaby the injector nozzle if compared to the results achieved for the case without collision. As a consequence, a slightly better matching between numerical and experimental PLV profiles is observed

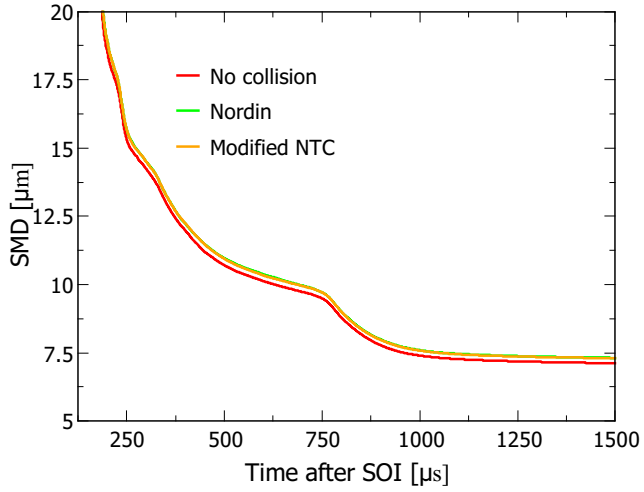

Figure 7.8: *G3 condition, validation of the modified NTC model based on the computed SMD*

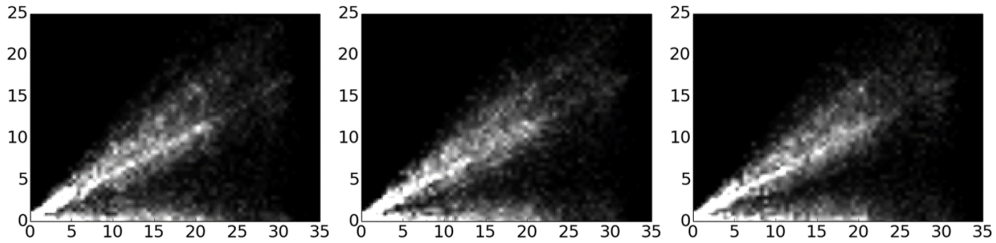

Figure 7.9: *G3 condition, computed PLV-based spray morphologies at 0.3 ms, standard G3 case (left), Nordin collision simulation (center) and modified NTC calculation (right). Range is* $0 - 0.01 \frac{mm^3}{mm^2}$, *axes dimensions reported in mm*

at axial distances below 20 mm for the collision cases while a satisfying computed liquid extinction is still achieved.

Overall, previous investigations demonstrated that simulations run with the modified NTC collision model provided very similar spray results compared to the Nordin model. Still, since the main target of the proposed research activity on collision modeling was to provide a compromise between accuracy and fast calculations it is mandatory to perform a final assessment on the observed computational times. For the Spray G3 case the difference between simulations run with and without the Nordin model became even greater than before because such operating point is characterized by the presence of a considerably higher number of parcels in the computational domain as a consequence of its limited evaporating condition. Such a fact depends on the parcel motion regime with most of the drops mainly experiencing a regime of shear stripping (KH) rather than

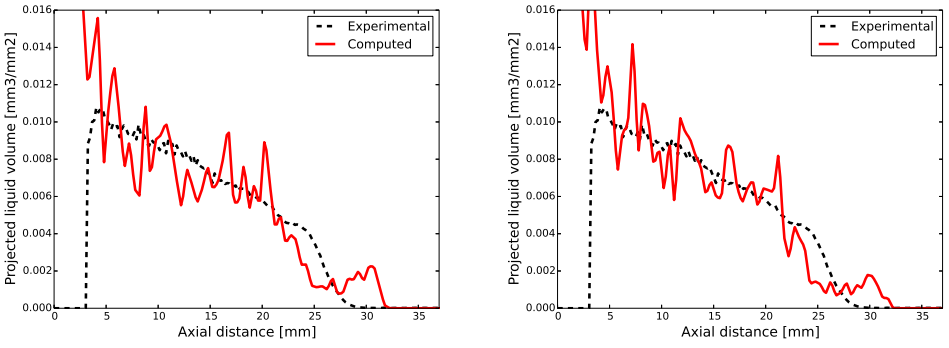

(a) No collision

(b) Nordin

(c) Modified NTC

Figure 7.10: *G3 condition, 0.3 ms, axial PLV profiles comparison between experiments and simulations*

catastrophic breakup (RT). As a consequence, the required calculation time of a classic collision approach further increases since a scanning activity on possibly hundreds of thousands of parcels is required at each time-step. In Tab.7.2 the computational times of the different Spray G3 simulations are reported with calculations that were again carried out on a 14-core Intel Xeon E5-2690 V4 CPU server with a time-step value equal to $5e^{-7}$ seconds.

Table 7.2: *Spray G3 condition, required computational times*

Case	Computational time
No collision	~ 17.6 hours
Nordin	~ 220.4 hours
Modified NTC	~ 18.9 hours

As it can be observed, the modified NTC simulation was more than a order of magnitude faster compared to the Nordin case while providing very similar spray results as previously demonstrated.

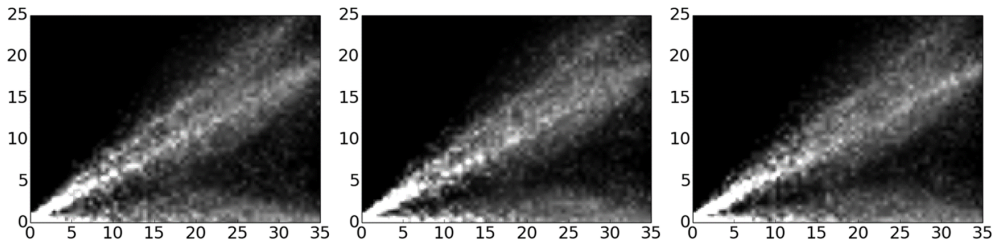

Figure 7.11: *G3 condition, computed PLV-based spray morphologies at 0.6 ms, standard G3 case (left), Nordin collision simulation (center) and modified NTC calculation (right). Range is* $0 - 0.01 \frac{mm^3}{mm^2}$, *axes dimensions reported in mm*

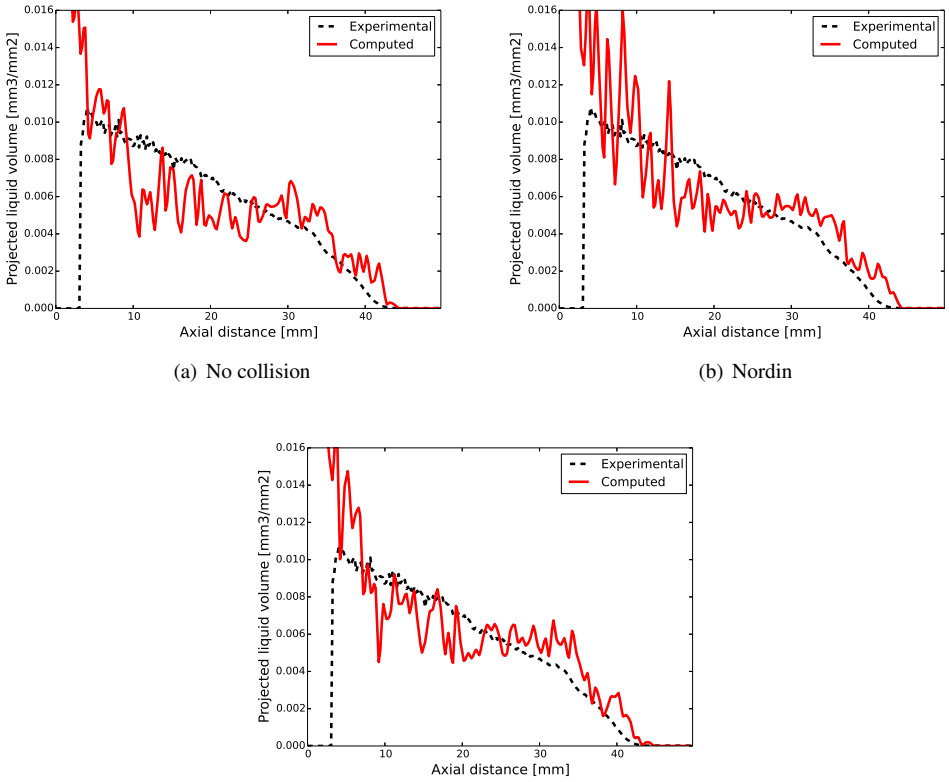

(a) No collision

(b) Nordin

(c) Modified NTC

Figure 7.12: *G3 condition, 0.6 ms, axial PLV profiles comparison between experiments and simulations*

7.4 Conclusions

A dedicated approach for numerical collision modeling was proposed in this chapter. As droplets collision is a physical phenomenon which is often overlooked in CFD simulations of multi-hole GDI sprays due to the high required computational time the aim of this research was to provide the LibICE framework with a method which could overcome such a weakness. As a consequence, the literature-based NTC approach was specifically implemented and then tested on the ECN Spray G injector against already available literature models such as those of O'Rourke and Nordin. Achieved results confirmed a better computational efficiency for the NTC method at the cost of an apparently less accurate spray modeling if compared to the Nordin model. The O'Rourke simulation was characterized by a required computational time very close to that of the Nordin case while apparently providing less accurate results as well. More in detail, the computed O'Rourke axial vapor penetration profile showed a trend which is similar to that of the NTC model, fact which was expected given that the physical phenomenon of collision of a selected pair of parcels should be equally handled by the two models. As a direct consequence of such a preliminary analysis a modification of the original NTC collision model was proposed, implemented into the LibICE and then validated on both G1 and G3 operating points with the aim to ensure the best possible compromise between reduced calculation times and accuracy of computed spray results. Overall, the difference in required computational time between modified NTC simulations and cases without parcel collision appeared negligible while the advantage over calculations with the Nordin model was considerable, especially with reference to the low-evaporating G3 condition which is characterized by a high number of parcels in the computational domain. Moreover, results showed a very similar behavior between the modified NTC model and the classic Nordin approach in terms of spray numerical reproduction. Overall, the proposed approach could represent an efficient way to model the phenomenon of physical collision which has often been overlooked in simulations of multi-hole GDI sprays. However, this chapter should still be considered as a first step towards this specific direction with further validations of the model which are highly encouraged by the author especially on different injector geometries and conditions which may be even

more influenced by the phenomenon of droplet collision compared to the ECN Spray G injector.

CHAPTER 8

Conclusions

This final chapter aims to provide a summary about the developed models, the performed simulations and the results achieved during the thesis work. The main contributions are divided into three sections:

- in the first one, conclusions are drawn on the adopted numerical methodologies for the modeling of fundamental physical phenomena for GDI sprays such as atomization and secondary breakup. A discussion on both the in-vessel and engine spray results is proposed;

- in the second section, the effects of the implemented collision model are summarized;

- finally, possible future lines of research within the field of this thesis are suggested.

8.1 Atomization and Secondary Breakup Modeling for GDI Sprays

Results reported in Chapter 4 determined what could be considered the starting point of the research activity carried out during this thesis. An at-the-time state of the art numerical setup was employed for the numerical prediction of the most important physical phenomena associated to a complex multi-hole GDI injector such as the ECN Spray G. Moreover, a wide range of operating points was tested with the aim to provide a significant dataset which could represent a solid basis for the upcoming investigations. From the very beginning one of the main targets of this activity has been to develop a comprehensive numerical setup which could provide accurate results for GDI sprays while also minimizing the activity of model tuning required from the user. This is not an easy task to achieve because direct injection gasoline sprays are employed in modern SI engines under significantly different operating conditions that can range from early injection events, characterized by low ambient pressure/density, to late injection operations for which ambient temperature, pressure and density increase dramatically leading to a higher evaporation rate. Moreover, early injection processes can be subjected to the phenomenon of flash boiling which occurs when the saturation pressure of the injected liquid fuel is greater than the surrounding gas pressure. As a consequence the liquid spray is subjected to a considerably increased evaporation rate which leads to plume collapse and enhanced air-fuel mixing within the engine chamber. It thus appears clear that reference spray parameters such as axial vapor penetration, axial liquid penetration and gas-liquid physical interaction may appear more complex to be accurately computed compared to what happens for Diesel sprays. Within this context, results achieved with the baseline numerical setup of Chapter 4 showed a good matching for the computed SMD and simulated axial liquid/vapor penetration trends which are comparable to those experimentally available for each tested case. However, the employed values of plume cone angle were observed to be considerably smaller if compared to experimental evidence. The plume cone angle also holds high influence on the evolving interaction between the liquid plumes and thus on the phenomena of entrainment and mixture formation. As a consequence, values which are too small proved to negatively influence the prediction of the centerline recirculation velocity at an axial position 15

mm downstream of the injector nozzle. More in detail, the positive peak of downard motion resulted underpredicted and hevily influenced by the size and the velocity of the droplets after the end of the injection. Furthermore, drops of smaller size are more easily carried on downards by the overall spray momentum leading to a greater positive peak of centerline velocity. It thus appears clear that the results of Chapter 4 showed a great influence due to the lack of parcel stripping activity from the employed secondary breakup model. The position where the centerline velocity is computed is also sensitive to the effects from the atomization phase with the rate of primary diameter reduction influencing both the computed positive and negative peaks of the profile. Overall, it can be stated that:

- a numerical prediction of the plume cone angle decoupled from the atomization model was necessary since the correlation employed in the Huh-Gosman mechanism was shown to underpredict such a value. As such, the user could be forced to calibrate the main model parameters to values well outised of the suggested literature range of validity;
- a different numerical methodology to model the atomization phase is required so that more control can be given to the user to fine tune the parcel diameter reduction rate within a well defined liquid core length.

It was also observed a reduced secondary breakup efficiency of the Reitz-Diwakar mechanism under evaporating conditions that are characterized by low ambient temperature, pressure and density. Within this context, to provide acceptable results in terms to computed axial liquid and vapor penetrations it was shown that the secondary breakup model required to work with a minimum Weber gas number below the reference threshold of physical droplet stability. On the other hand, the stipped mass mechanism for child parcels which is employed by the Reitz-KHRT model led to the formation of a non-physical cluster of droplets at the tip of the plumes negatively affecting the predicted spray morphology as a consequence.

In Chapter 5 many of these aspects were addressed by proposing a numerical setup which is still based on Huh-Gosman and Reitz-KHRT models while now satisfying the new following conditions:

- decoupling of the numerical plume cone angle prediction from the atomization model. As a consequence it was possible to work on the interaction between the spray angle and the entrainment without forcing the adoption of out-of-range parameters in the Huh-Gosman mechanism;
- calibration of the Reitz-KHRT tuning constants on the baseline Spray G1 operating case with the aim to achieve the best compromise in terms of axial spray penetration and centerline velocity prediction. Moreover, all the tested cases were simulated under the same baseline numerical setup so that it could be possible to evaluate the accuracy of the proposed approach when employed under a wide range of operating conditions.

An innovative post-processing methodology for the liquid component was then developed on the basis of a projected liquid volume (PLV) Eulerian field allowing to better investigate fundamental quantities such as axial liquid penetration, spray morphology and in-plume liquid distribution thanks to validations against bespoke experimental data made available for the ECN6 Workshop. Within this context, improvements were observed regarding the computed centerline velocity for the baseline G1 condition (now much closer to the experimental profile) and in terms of case-to-case consistency given that the calculated axial liquid and vapor penetration profiles matched with good accuracy the experimental data for each operating point. The more detailed analysis based on the PLV field however demonstrated numerical limitations of the setup in computing the axial in-plume liquid distribution with both G1 and G3 operating points characterized by plumes too rich in fuel at the tip. While this phenomenon could be mitigated by providing a better numerical transition from the atomization to the secondary breakup phase, the good morphology prediction of the flash boiling G2 condition showed that an underprediction of the spray evaporation rate could as well be considered as the reason behind these results. It must be noticed that such a detailed investigation is possible with a dedicated vessel setup for which bespoke experimental data are made available so that a fine sub-model optimization can be carried out. Under dynamic engine conditions it is more difficult to assess the computed spray with such a degree of detail and main injection quantities such as axial liquid/vapor penetrations, plume cone angle, targeting and entrainment hold higher influence on combustion modeling accu-

racy. Full-cycle simulations of the IFPEN optical access engine reported in Chapter 5 confirmed this hypothesis since the numerical spray setup of the ECN6 Workshop was carried over without any change in the setup. Weak points assessed under vessel conditions such as the not perfect computed in-plume liquid distribution only marginally affected the final goal of the activity. Combustion results of peak pressure and heat release rate demonstrated that it is more important to correctly predict the main physical characteristics of the in-cylinder flow motion by means of an accurate full-cycle numerical setup. In any case, a mandatory objective of research activities such as the one reported in this thesis work must always be to pursue improvements in numerical accuracy down to the smallest degree of detail.

Within this context, the focus of the proposed activity was to optimize as much as possible the numerical spray setup for the CFD modeling of Lagrangian sprays. In Chapter 6 different approaches for atomization and secondary breakup were thus proposed so that the weaknesses of the ECN6 setup could be addressed. At first, the atomization phase was separately treated with two smooth parcel diameter reduction mechanisms either based on the Pilch-Erdman model or on a dedicated Kelvin-Helmholtz approach. As a consequence, a better control on the atomization rate and on the transition to secondary breakup was achieved. The proposed modification was also tested on the Spray G3 operating condition coupled under multiple operating points of the optical access Darmstadt engine. The activity allowed to extract preliminary information on the in-cylinder mixture formation which could be valuable for the calibration of upcoming full-cycle simulations performed under firing conditions in the context of the ECN research activity. A dynamic KHRT secondary breakup model was then implemented into the LibICE framework on the basis of the proposition of Nagaoka and Kawamura. Under this configuration the main model parameters are treated as a function both of the operating density ratio and the droplet Weber gas number so that the computed breakup could happen within conditions matching the total breakup time proposed by Pilch and Erdman. Rresults showed that for operating points with low ambient density and Weber gas number values such as G2 and G3 the model provided accurate results in terms of axial liquid penetration, axial vapor penetration, spray morphology and in-plume PLV liquid distribution without any recalibration activity required from the user. On the

other hand, as the Weber gas number increased it was observed that such a dynamic approach tended to overpredict the fuel evaporation rate leading to an underpredicted computed axial liquid penetration. This fact was however observed mainly for wave-crest stripping and catastrophic motion regimes for which the prediction of secondary breakup appears to be less sensitive to a variation of the main model parameters. For these conditions a fixed setup was thus proposed, calibrated and tested on the baseline Spray G1 and then also validated on the high evaporation and high collapse G7 operating point. Finally, the literature-based evaporation mechanism of Adachi-Price was specifically implemented into the LibICE to further enhance the available options for flash boiling modeling. Overall, a comprehensive set of models was made available so that good numerical results for multi-hole GDI sprays under a wide range of operating conditions could be achieved within the OpenFOAM®-LibICE numerical framework.

8.2 Droplets Collision Modeling

Numerically modeling the physical phenomenon of droplets collision is a difficult task because of the high required computational time. In particular, this aspect is true for complex, multi-hole GDI sprays which can be characterized by a considerably high amount of parcels that are present in the computational domain especially under low-evaporating conditions. Because of such a limitation collision prediction, albeit being a relevant and impactful process on the morphology and evaporation rate of a spray, is often overlooked in CFD simulations. To address this limitation, in this work the literature-based NTC model was implemented into the LibICE framework with the aim to provide an optimized compromise on the required computational time for collision modeling. For each cell a list of the contained parcels is updated at every time-step with the model being based on a mathematical rearrangement concerning the way a pair of parcels is numerically selected for collision and the statistical sampling of the potentially colliding pairs. As a consequence the model is much faster than classic O'Rourke or Nordin mechanisms because a more mathematically efficient selection method is employed while still providing consistent results in terms of collision output. Once a pair of parcels is selected collision takes place according to the same physical constraints adopted by the O'Rourke model. By comparing literature data and results respectively

obtained without collision, with the O'Rourke approach and with the Nordin model it was possible to observe that the employed NTC method, albeit considerably faster than the others, provided inaccurate results in terms of axial spray penetration. The same behavior was noticed for the case simulated with the available O'Rourke model, even if to a lesser extent. The discrepancy between NTC and experimental penetration profiles was considered to be due to numerical reasons and to be dependent on the formulation for collision probability which is employed by the model. However, after such an initial difference the computed NTC and O'Rourke axial penetration trends appeared to be characterized by an extremely similar behavior during the whole simulation duration. This fact was specifically investigated and considered to be dependent on the physical approach adopted for collision of two parcel, which is in common between the two models. On the contrary, the Nordin case provided the most accurate spray results with a computational time similar to that of the O'Rourke method and considerably higher than what it was required by the NTC mechanism. Within this context, a modification of the original NTC model was proposed so that a compromise between fast computations and accurate results could be achieved. The physical collision approach adopted by Nordin was extendend to the NTC model as well while keeping the quick mathematical approach for parcel selection. Unlike for O'Rourke and NTC models, the physical mechanism proposed by Nordin takes collision into account also between parcels from different computational cells by calculating their trajectories. However, to sample parcels in different cells would nullify the computational advantages of the NTC approach. To overcome this drawback the modified NTC mechanism was subjected to an increase of the temporal probability decay parameter. This is a model constant which is typical of the trajectory method and its increment allowed to enhance the in-cell collision probability of the modified NTC approach so that the original Nordin model could be matched in terms of overall spray output accuracy. The proposed model was then validated in terms of computational speed, axial vapor penetration, Sauter Mean Diameter and spray morphology on the low-evaporating G3 operating point which was chosen as the benchmark condition because of its high number of persisting parcels. Results showed that the model could provide a very similar physical spray output to that of the original Nordin mechanism while being much faster in terms of required

computational time.

8.3 Future Works

The CFD modeling of multi-hole GDI Lagrangian sprays represent a complex task which requires a wide set of dedicated sub-models coherently interacting with each other so that an accurate numerical output can be provided. Despite the proposed effort towards improved numerical accuracy, further research activities may still be needed to address remaining weaknesses such as:

- lack of correlations capable to provide accurate values for the spray plume cone angle as a function of ambient conditions. In fact, while directly providing the PCA value allows for a fine spray reproduction in a static vessel, in transient full-cycle simulations the angle should vary over time according to changes in ambient conditions as a mandatory requirement especially for late injection events towards engine compression phase. Existing formulations do vary the angle as a function of the injection main parameters but on multiple occasions a considerable under-prediction was observed compared to experimental evidence. Moreover, a correlation directly related to the injector model would represent the best solution as it would ensure the previous advantages while also allowing for an the utilization of different atomization/secondary breakup configurations;
- lack of more detailed heat transfer models which could specifically be implemented into the LibICE framework;
- utilization of single component liquid fuels. On the path towards emissions reduction it will in fact become mandatory to validate the different Lagrangian sub-models on injection simulations with multi-component surrogates. In this regard, the recently held ECN7 Workshop led the way by proposing preliminary GDI Spray G results which will serve as an important starting point for upcoming investigations.

Bibliography

[1] *ESI Group. OpenFOAM website: https://openfoam.org/.*

[2] *https://ecn.sandia.gov/ecn-workshop/ecn6-workshop/.*

[3] *https://ecn.sandia.gov/ecn-workshop/search-presentations/.*

[4] *https://ecn.sandia.gov/gasoline-spray-combustion/.*

[5] *https://ecn.sandia.gov/gasoline-spray-combustion/target-condition/primary-spray-g-datasets/.*

[6] *https://ecn.sandia.gov/wp-content/uploads/2016/08/ECN4Grover.mov.*

[7] *https://www.ifpenergiesnouvelles.com/.*

[8] *https://www.rsm.tu-darmstadt.de/home_rsm/events_3/darmstadt_engine_workshop/index.en.jsp.*

[9] *http://www.upgrade-project.eu/.*

[10] Proposal for post-2020 CO2 targets for cars and vans. *European Commission*, https://ec.europa.eu/clima/policies/transport/vehicles/proposal_en, 2018.

[11] M. Adachi, V.G. McDonell, D. Tanaka, J. Senda, and H. Fujimoto. Characterization of fuel vapor concentration inside a flash boiling spray. *SAE Technical Paper*, 970871, 1997.

[12] L. Allocca, A. Montanaro, R. Di Gioia, and G. Bonandrini. Spray characterization of a single-hole gasoline injector under flash boiling conditions. *SAE Technical Paper*, 2014-32-0041, 2014.

[13] A.A. Amsden, P.J. O'Rourke, and T.D. Butler. KIVA-II: A computer program for chemically reactive flows with sprays. Los Alamos Natl. Lab., LA-11560-MS, 1989, doi:10.1007/BF01054829, 1989.

[14] F. Backes, S. Blochum, M. Härtl, and G. Wachtmeister. Experimental analysis of gasoline direct injector tip wetting. *SAE International Journal of Engines*, 13(1), 2019.

[15] C. Bai and A. Gosman. Mathematical modelling of wall films formed by impinging sprays. *SAE Technical Paper*, 960626, 1996.

[16] E.T. Baldwin, R. Grover, S.E. Parrish, D.J. Duke, K.E. Matusik, C.F. Powell, A.L. Kastengren, and D.P. Schmidt. String flash-boiling in gasoline direct injection simulations with transient needle motion. Int. J. Multiphase Flow 87:90-101, 2016.

[17] Michele Bardi, Guillaume Pilla, and Xavier Gautrot. Experimental assessment of the sources of regulated and unregulated nanoparticles in gasoline direct-injection engines. *International Journal of Engine Research*, 20(1):128–140, 2019.

[18] E. Baum, B. Peterson, B. Böhm, and A. Dreizler. On the validation of LES applied to internal combustion engine flows: Part 1: Comprehensive experimental database. *Flow, Turbulence and Combustion*, 92(1):269–297, 2014.

[19] C. Baumgarten. *Mixture Formation in Internal Combustion Engines*. Springer, 2006.

[20] Bharat Bhatia and Ashoke De. Flash boiling in sprays: Recent developments and modeling. *Journal of the Indian Institute of Science*, 2019.

[21] M. Bode, T. Falkenstein, V. Le Chenadec, and S. Kang et al. A new euler/lagrange approach for multiphase simulations of a multi-hole GDI injector. *SAE Technical Paper*, 2015-01-0949, 2015.

[22] Sebastian Bornschlegel, Chris Conrad, Alexander Durst, Jin Wang, and Michael Wensing. Multi-hole gasoline direct injection:in-nozzle flow and primary breakup investigated in transparent nozzlesand with X-Ray. *International Journal of Engine Research*, 19(1):67–77, 2018.

[23] Myungsik Choi, Young-Hong Kwak, Jerry Song, Varun Negandhi, and Daniel Gajowski. Synergies of cooled external EGR, water injection, miller valve events and cylinder deactivation for the improvement of fuel economy on a turbocharged-GDI engine; part 1, engine simulation. *SAE Technical Paper*, 2019-01-0245, 2019.

[24] Matthieu Cordier, Matthieu Lecompte, Louis-Marie Malbec, Benjamin Reveille, Cedric Servant, Faycal Souidi, and Nicola Torcolini. Water injection to improve direct injection spark ignition engine efficiency. *SAE Technical Paper*, 2019-01-1139, 2019.

[25] Daniel Duke, Alan L. Kastengren, Katarzyna Matusik, Andrew Swantek, Christopher F. Powell, Raul Payri, Daniel Vaquerizo, Lama Itani, Gilles Bruneaux, Jr Ronald O. Grover, Scott Parrish, Lee Markle, David Schmidt, Julien Manin, Scott A. Skeen, and Lyle M. Pickett. Internal and near nozzle measurements of engine combustion network "Spray G" gasoline direct injectors. *Experimental Thermal and Fluid Science*, 88, 07 2017.

[26] K. Gopal Duleep. The impact of gasoline direct injection system design on PM emissions. *SAE Technical Paper*, 2019-01-0072, 2019.

[27] Sreelekha Etikyala, Lucien Koopmans, and Petter Dahlander. Particulate emissions in a GDI with an upstream fuel source. *SAE Technical Paper*, 2019-01-1180, 2019.

[28] G. Ferrari. *Motori a Combustione Interna*. Edizioni Il Capitello, 2001.

[29] Joel H. Ferziger and Milovan Peric. *Computational methods for fluid dynamics*. Springer Science & Business Media, 2012.

[30] D. Freudenhammer, E. Baum, B. Peterson, B. Böhm, B. Jung, and S. Grundmann. Volumetric intake flow measurements of an IC engine using magnetic resonance velocimetry. *Experiments in Fluids, 55:1724*, 2014.

[31] Daniel Freudenhammer, Brian Peterson, Carl-Philipp Ding, Benjamin Boehm, and Sven Grundmann. The influence of cylinder head geometry variations on the volumetric intake flow captured by magnetic resonance velocimetry. *SAE International Journal of Engines*, 8(4):1826–1836, 2015.

[32] J. Garcia-Oliver, J. Pastor, A. Pandal, N. Trask, E. Baldwin, and D. Schmidt. Diesel spray CFD simulations based on the $\sum$-y eulerian atomization model. Atomization and Sprays, vol. 23, pp. 71-95, 2013.

[33] J. Hammer, A. Kufferath, and K. Wehmeier. Modern GDI combustion systems with focus on fuel metering technology fulfilling future emission legislation. In: SIA conference: the spark ignition engine of the future, Strasbourg, France, 30 November 1 December 2011.

[34] J. Harada, T. Tomita, H. Mizuno, Z. Mashiki, and Y. Ito. Development of direct injection gasoline engine. *SAE 970540*.

[35] R. Herweg and R. R. Maly. A fundamental model for flame kernel formation in S. I. engines. 1992.

[36] J.B. Heywood. *Internal Combustion Engine Fundamentals*. McGraw-Hill, 1988.

[37] C.W. Hirt and B.D. Nichols. Volume of fluid (VOF) method for the dynamics of free boundaries. journal of computational physics. *Journal of Computational Physics, 39, 201-225*, 1981.

[38] Jérôme Hélie, Nicolas Lamarque, Jean-Luc Fremaux, Philippe Serrecchia, Maziar Khosravi, and Oliver Berkemeier. The process of tip wetting at the spray injection end. *International Journal of Engine Research*, page 1468087419840842, 2019.

[39] K.Y. Huh and A.D. Gosman. A phenomenological model of diesel spray atomization. Proceedings of the International Conference on Multiphase Flows, Tsukuba, Japan, 1991.

[40] A. Isenstadt, J. German, M. Dorobantu, D. Boggs, and T. Watson. Downsized, boosted gasoline engines. *International Council On Clean Transportation, Working Paper 2016-2*, 2016.

[41] H. Jasak. *Error Analysis and Estimation for the Finite Volume Method with Applications to Fluid Flows*. PhD Thesis, Imperial College, London.

[42] S.J. Jeong, S.D. Oh, H.K. Lee, J.K. Park, G.S. Lee, Y.D. Pyo, and O.T. Lim. Research and development of a 2.9 liter light-duty dme truck using common rail fuel injection system. *KSAE 2011 Annual Conference, KSAE11-A0073, 2011*.

[43] A. Joshi. Review of vehicle engine efficiency and emissions. *https://doi.org/10.4271/2019-01-0314*, 2019.

[44] Mutsumi Kanda, Toyokazu Baika, Senji Kato, and Minoru Iwamuro. Application of a new combustion concept to direct injection gasoline engine. *SAE Transactions*, 2000.

[45] Yunyoung Kim, Cheolmin Park, Jonghyuk Kim, and Byeongdu Min. The effect of low temperature egr and low compression ratio on nox reduction for eu6 diesel engine. *SAE Technical Paper*, 2013-01-2644, 2013.

[46] Makoto Koike, Akinori Saito, Terutoshi Tomoda, and Yasuhiro Yamamoto. Research and development of a new direct injection gasoline engine. *SAE Transactions*, 109:543–552, 2000.

[47] A.V. Kolpakov, K.V. Romanov, and E.I. Titova. Calculation of the rebound condition for colliding drops of sharply different sizes. *Kollodn Zh, 47: 953*, 1985.

[48] T. Larsson, O. Stenlaas, and A. Erlandsson. Future fuels for DISI engines: A review on oxygenated, liquid biofuels. *SAE Technical Paper*, 2019-01-0036, 2019.

[49] S. Lee, S. Jeong, and O. Lim. An investigation on the spray characteristics of DME with variation of ambient pressure using the common rail fuel injection system. *J Mech Sci Technol 26, 3323–3330 (2012). https://doi.org/10.1007/s12206-012-0806-8*.

[50] Haifeng Lu, Jun Deng, Zongjie Hu, Zhijun Wu, Liguang Li, Fangen Yuan, Degang Xie, Shuang Yuan, and Yuan Shen. Study on fuel economy improvement by low pressure water-cooled egr system on a downsized boosted gasoline engine. *SAE Technical Paper*, 2016-01-0678, 2016.

[51] T. Lucchini, G. D'Errico, F. Brusiani, G.M. Bianchi, Z. Tukovic, and H. Jasak. Multi-dimensional modeling of the air/fuel mixture formation process in a PFI engine for motorcycle applications. SAE paper, 2009-24-0015, 2009.

[52] T. Lucchini, G. D'Errico, and M. Fiocco. Multi-dimensional modeling of gas exchange and fuel-air mixing processes in a direct-injection, gas fueled engine. SAE paper, 2011-24-0036, 2011.

[53] T. Lucchini, G. D'Errico, A. Onorati, G. Bonandrini, L. Venturoli, and R. Di Gioia. Development of a cfd approach to model fuel-air mixing in gasoline direct-injection engines. *SAE Paper*, 2012-01-0146, 2012.

[54] T. Lucchini, G. D'Errico, A. Onorati, G.Bonandrini, L. Venturoli, and R. Di Gioia. Development and application of a computational fluid dynamics methodology to predict fuel-air mixing and sources of soot formation in gasoline direct injection engines. *International Journal of Engine Research*, 10.1177/1468087413500297, 2013.

[55] T. Lucchini, D. Paredi, and J. Lacey. Topic 10: Evaporative Spray G (external, plume interaction, flash boiling). *ECN6 proceedings*, Valencia, 2018.

[56] T. Lucchini, A. Della Torre, G. D'Errico, G. Montenegro, M. Fiocco, and A. Maghbouli. Automatic mesh generation for cfd simulations of direct-injection engines. *SAE Paper*, 2015-01-0376, 2015.

[57] Tommaso Lucchini, Gianluca D'Errico, Davide Paredi, Lorenzo Sforza, and Angelo Onorati. Cfd modeling of gas exchange, fuel-air mixing and combustion in gasoline direct-injection engines. *SAE Technical Paper*, 2019-24-0095, 2019.

[58] Noud Maes, Nico Dam, Bart Somers, Tommaso Lucchini, Gianluca D'Errico, and Gilles Hardy. Experimental and numerical analyses of liquid and spray penetration under heavy-duty diesel engine conditions. *SAE Int. J. Fuels Lubr.*, 9:108–124, 04 2016.

[59] J. Manin, Y. Jung, S.A. Skeen, L.M. Pickett, S.E. Parrish, and L. Markle. Experimental characterization of DI gasoline injection processes. *SAE Technical Paper*, 2015-01-1894, 2015.

[60] Xandra Margot. Editorial — 'Thermo- and fluid-dynamic processes in direct injection engines': THIESEL 2018 special issue by Xandra Margot. *International Journal of Engine Research*, 20(1):3–5, 2019.

[61] Gabrielle L Martinez, Farzad Poursadegh, Gina M Magnotti, Katarzyna E Matusik, Daniel J Duke, Benjamin W Knox, Alan L Kastengren, Christopher F Powell, and Caroline L Genzale. Measurement of sauter

mean diameter in diesel sprays using a scattering–absorption measurement ratio technique. *International Journal of Engine Research*, 20(1):6–17, 2019.

[62] G. Martini. Scientific evidence on vehicle's emissions. *EU Commission Stakeholder Event, https://ec.europa.eu/docsroom/ documents/32164*, 2018.

[63] Marianna Migliaccio, Alessandro Montanaro, Davide Paredi, Tommaso Lucchini, Luigi Allocca, and Gianluca D'Errico. CFD modeling and validation of the ECN Spray G experiment under a wide range of operating conditions. *SAE Technical Paper*, 2019-24-0130, 2019.

[64] N Mitroglou, J M Nouri, M Gavaises, and C Arcoumanis. Spray characteristics of a multi-hole injector for direct-injection gasoline engines. *International Journal of Engine Research*, 7(3):255–270, 2006.

[65] M. Mojtabi, N. Chadwick, G. Wigley, and J. Helie. The effect of flash boiling on break up and atomization in GDI sprays. *ILASS 2008*, 2008.

[66] A. Montanaro, L. Allocca, D. Ettorre, T. Lucchini, F. Brusiani, and G. Cazzoli. Experimental characterization of high-pressure impinging sprays for CFD modeling of GDI engines. SAE paper, 2011-01-0685, 2011.

[67] A. Montanaro, L. Allocca, and M. Lazzaro. Iso-octane spray from a GDI multi-hole injector under non- and flash boiling conditions. *SAE Technical Paper*, 2017-01-2319, 2017.

[68] A. Montanaro, L. Allocca, and G. Meccariello. Gasoline fuel sprays characterization at very-high injection pressures. *SAE Technical Paper*, 2019.

[69] M. Moulai, R. Grover, S. Parrish, and D. Schmidt. Internal and near-nozzle flow in a multi-hole gasoline injector under flashing and non-flashing conditions. *SAE Technical Paper*, 2015-01-0944, 2015.

[70] Makoto Nagaoka and Kiyomi Kawamura. A deforming droplet model for fuel spray in direct-injection gasoline engines. *SAE Technical Paper*, 2001-01-1225, 2001.

[71] Kazutoshi Noma, Yasuyuki Iwamoto, Nobuaki Murakami, Kazumasa Iida, and Osamu Nakayama. Optimized gasoline direct injection engine for the european market. *SAE Technical Paper*, 10.4271/980150, 1998.

[72] P.A. Niklas Nordin. Complex chemistry modeling of diesel spray combustion. 2001.

[73] Sechul Oh, Seokwon Cho, Eunsu Seol, Chiheon Song, Woojae Shin, Kyoungdoug Min, Han Ho Song, Byeongsoek Lee, Jinwook SON, and Soo Hyung Woo. An experimental study on the effect of stroke-to-bore ratio of atkinson disi engines with variable valve timing. *SAE Int. J. Engines*, 11:1183–1193, 04 2018.

[74] P J O'Rourke. Collective drop effects on vaporizing liquid sprays. 11 1981.

[75] D. Paredi, T. Lucchini, G. D'Errico, and A. Onorati et al. Gas exchange and injection modeling of an advanced natural gas engine for heavy duty applications. SAE Technical Paper, 2017-24-0026, 2017.

[76] D. Paredi, T. Lucchini, G. D'Errico, A. Onorati, A. Montanaro, L. Allocca, and R. Ianniello. Combined experimental and numerical investigation of the ECN Spray G under different engine-like conditions. *SAE Technical Paper*, 2018-01-0281, 2018.

[77] Davide Paredi, Tommaso Lucchini, Gianluca D'Errico, A. Onorati, L. Pickett, and J. Lacey. Cfd modeling of spray evolution for spark-ignition, direct injection engines. *AIP Conference Proceedings*, 2191:020125, 12 2019.

[78] Davide Paredi, Tommaso Lucchini, Gianluca D'Errico, Angelo Onorati, Alessandro Montanaro, Luigi Allocca, and Roberto Ianniello. Combined experimental and numerical investigation of the ECN Spray G under different engine-like conditions. *SAE Technical Paper*, 2018-01-0281, 2018.

[79] Davide Paredi, Tommaso Lucchini, Gianluca D'Errico, Angelo Onorati, Lyle Pickett, and Joshua Lacey. Validation of a comprehensive computational fluid dynamics methodology to predict the direct injection process of gasoline sprays using Spray G experimental data. *International Journal of Engine Research*, page 146808741986802, 08 2019.

[80] S. Parrish. Evaluation of liquid and vapor penetration of sprays from a multi-hole gasoline fuel injector operating under engine-like conditions. *SAE Int. J. Engines*, 2014-01-1409, 2014.

[81] S. Parrish. Gasoline spray Spray G Topic 3.4, drop size measurement. *ECN3 workshop*, Detroit, 2014.

[82] S.E. Parrish, R.J. Zink, Y. Sivathanu, and J. Lim. Spray patternation of a multi hole injector utilizing planar line of sight extinction tomography. *ILASS Americas, 22nd Annual Conference on Liquid Atomization and Spray Systems*, 2010.

[83] Andrea Pati, Davide Paredi, Tommaso Lucchini, and Christian Hasse. CFD modeling of gas-fuel interaction and mixture formation in a gasoline direct-injection engine coupled with the ECN Spray G injector. *SAE Technical Paper*, 2020-01-0327, 2020.

[84] R. Payri, J. Gimeno, P. Marti-Aldaravi, and D. Vaquerizo. Momentum flux measurements on an ECN GDI injector. *SAE Technical Paper*, 2015-01-1893, 2015.

[85] R. Payri, F.J. Salvador, P. Martí-Aldaraví, and D. Vaquerizo. ECN Spray G external spray visualization and spray collapse description through penetration and morphology analysis. Applied Thermal Engineering. 112. 304-316. 10.1016/j.applthermaleng.2016.10.023, 2017.

[86] R. J. Pearson and J. W. G. Turner. *Renewable fuels - an automotive perspective*. Elsevier, Netherlands, 2012.

[87] L.M. Pickett. Spray G lagrangian modeling. ECN5 proceedings, Detroit, MI, 2016.

[88] M. Pilch and C.A. Erdman. Use of breakup time data and velocity history data to predict the maximum size of stable fragments for acceleration-induced breakup of a liquid drop. Int. J. Multiphase Flow Vol. 13, No. 6, pp. 741-757, 1987, 1987.

[89] O'Rourke P.J. and Amsden A.A. A particle numerical model for wall film dynamics in port-injected engines. 1996.

[90] S.B. Pope. An explanation of the turbulent round-jet/plane-jet anomaly. *AIAA Journal*, 16:279–281, 02 1978.

[91] Adèle Poubeau, Arthur Vauvy, Florence Duffour, Jean-Marc Zaccardi, Gaetano de Paola, and Marek Abramczuk. Modeling investigation of thermal insulation approaches for low heat rejection diesel engines using a conjugate heat transfer model. *International Journal of Engine Research*, 20(1):92–104, 2019.

[92] C. Price, A. Hamzehloo, P. Aleiferis, and D. Richardson. An approach to modeling flash-boiling fuel sprays for direct-injection spark-ignition engines. *Atomization and Sprays*, 26 (2): 1-43, 2016.

[93] Sampath K Rachakonda, Arman Paydarfar, and David P Schmidt. Prediction of spray collapse in multi-hole gasoline direct-injection fuel injectors. *International Journal of Engine Research*, 20(1):18–33, 2018.

[94] W.E. Ranz and Jr. W.R. Marshall. Evaporation from drops, part i. *Chem. Eng. Prog., 48(4):173-180*, April 1952.

[95] W.E. Ranz and Jr. W.R. Marshall. Evaporation from drops, part i. *Chem. Eng. Prog., 48(3):141-146*, March 1952.

[96] R. D. Reitz. Modeling Atomization Processes In High Pressure Vaporizing Sprays. *Atomization and Spray Technology*, Vol. 3:pp. 309–337, 1987.

[97] R.D. Reitz. A photographic study of flash-boiling atomization. Aerosol Sci. Technol., 1990, 12, 561-569, 1990.

[98] Matsumoto S. and Saito S. On the mechanism of suspension of parcels in horizontal conveying: Monte carlo simulation based on the irregular bouncing model. J Chem Eng Jpn 1970; 2: 83-92.

[99] K. Saha, S. Quan, M. Battistoni, and S. Som et al. Coupled eulerian internal nozzle flow and lagrangian spray simulations for GDI systems. *SAE Technical Paper*, 2017-01-0834, 2017.

[100] K. Saha, S. Som, M. Battistoni, Y. Li, E. Pomraning, and P.K. Senecal. Numerical investigation of two-phase flow evolution of in- and near-nozzle regions of a gasoline direct injection engine during needle transients. SAE 2016-01-0870, 2016.

[101] R. Scarcelli, T. Wallner, H. Obermair, V.M. Salazar, and S.A. Kaiser. CFD and optical investigations of fluid dynamics and mixture formation in a DI-H2 ICE. *ASME*, ICEF2010-35084, 2010.

[102] David P. Schmidt and C.J. Rutland. A new droplet collision algorithm. *Journal of Computational Physics*, 164(1):62 – 80, 2000.

[103] M. Sellnau, M. Foster, W. Moore, and J. et al. Sinnamon. Pathway to 50injection compression ignition. *doi:10.4271/2019-01-1154*, 2019.

[104] P. Smith, J. Heywood, and W. Cheng. Effects of compression ratio on spark-ignited engine efficiency. *SAE Technical Paper*, 2014-01-2599, 2014.

[105] P. Sphicas, L. Pickett, S. Skeen, and J. Frank et al. A comparison of experimental and modeled velocity in gasoline direct-injection sprays with plume interaction and collapse. *SAE Int. J. Fuels Lubr.*, 2017-01-0837, 2017.

[106] P. Sphicas, L.M. Pickett, S.A. Skeen, and J.H. Frank. Inter-plume aerodynamics for gasoline spray collapse. *International Journal of Engine Research*, 19(10), 1048–1067. https://doi.org/10.1177/1468087417740306, 2018.

[107] Panos Sphicas, Lyle M Pickett, Scott A Skeen, and Jonathan H Frank. Inter-plume aerodynamics for gasoline spray collapse. *International Journal of Engine Research*, 19(10):1048–1067, 2018.

[108] G. Stiesch. *Modeling Engine Spray and Combustion Processes*. Springer.

[109] John M. Storey, Melanie Moses-DeBusk, Shean Huff, John Thomas, Mary Eibl, and Faustine Li. Characterization of GDI PM during vehicle start-stop operation. *SAE Technical Paper*, 2019-01-0050, 2019.

[110] P. Strek, D. Duke, A. Swantek, A. Kastengren, C.F. Powell, and D.P. Schmidt. X-Ray radiography and CFD studies of the Spray G injector. *SAE Technical Paper*, 2016-01-0858, 2016.

[111] Jianye Su, Min Xu, Tie Li, Yi Gao, and Jiasheng Wang. Combined effects of cooled egr and a higher geometric compression ratio on thermal efficiency improvement of a downsized boosted spark-ignition direct-injection engine. *Energy Conversion and Management*, 78:65–73, 02 2014.

[112] Daisuke Takaki, Hirofumi Tsuchida, Tetsuya Kobara, Mitsuhiro Akagi, Takeshi Tsuyuki, and Morihiro Nagamine. Study of an egr system for downsizing turbocharged gasoline engine to improve fuel economy. *SAE Technical Paper*, 2014-01-1199, 2014.

[113] R. Torelli, G. D'Errico, T. Lucchini, V. Ikonomou, and R.M. McDavid. A spherical volume interaction DDM approach for diesel spray modeling. Atomization and Sprays, vol. 25, no. 4, pp. 335-374, 2015.

[114] Augusto Della Torre, Gianluca Montenegro, Angelo Onorati, Tarcisio Cerri, Enrico Tronconi, and Isabella Nova. Numerical optimization of a SCR system based on the injection of pure gaseous ammonia for the NOx reduction in light-duty diesel engines. *SAE Technical Paper*, 2020-01-0356, 2020.

[115] Augusto Della Torre, Gianluca Montenegro, Angelo Onorati, Sumit Khadilkar, and Roberto Icarelli. CFD modeling of compact heat exchangers for I.C. engine oil cooling. *SAE Technical Paper*, 2019-24-0179, 2019.

[116] Noboru Uchida, Takeshi Okamoto, and Hiroki Watanabe. A new concept of actively controlled rate of diesel combustion for improving brake thermal efficiency of diesel engines: Part 1—verification of the concept. *International Journal of Engine Research*, 19(4):474–487, 2018.

[117] Noboru Uchida and Hiroki Watanabe. A new concept of actively controlled rate of diesel combustion (ACCORDIC): Part II—simultaneous improvements in brake thermal efficiency and heat loss with modified nozzles. *International Journal of Engine Research*, 20(1):34–45, 2019.

[118] B.A. VanDerWege. The effect of fuel volatility and operating conditions on spray from pressure swirl fuel injectors. PhD Thesis, Massachusetts Institute of Technology, 1999.

[119] B.A. VanDerWege, T.H. Lounsberry, and S. Hochgreb. Numerical modeling of fuel sprays in DISI engines under early-injection operating conditions. SAE Paper, 2000-01-0273, 2000.

[120] Henk Kaarle Versteeg and Weeratunge Malalasekera. *An introduction to computational fluid dynamics: the finite volume method*. Pearson Education, 2007.

[121] L. Weiss, M. Wensing, J. Hwang, L.M. Pickett, and S.A. Skeen. Development of limited-view tomography for measurement of Spray G plume direction and liquid volume fraction. *Exp Fluids 61,51, https://doi.org/10.1007/s00348-020-2885-0*, 2020.

[122] HG Weller. The development of a new flame area combustion model using conditional averagingthermo-fluids section report TF 9307. *Imperial College of Science, Technology and Medicine, London*, 1993.

[123] H. Zhao. Overview of gasoline direct injection engines, no. di. Woodhead Publishing Limited, 2009.

[124] Denghao Zhu, Yuedong Chao, Jun Deng, Zongjie Hu, Liguang Li, Li Guan, Chen Yang, and Yuan Shen. Combined technologies for efficiency improvement on a 1.0 l turbocharged GDI engine. *SAE Technical Paper*, 2019-01-0233, 2019.

[125] B. Zuo, A.M. Gomes, and C.J. Rutland. Modeling superheated fuel sprays and vaporization. *Journal of Engine Research*, 2001.

Appendices

APPENDIX $\mathcal{A}$

ECN Spray G1 Operating Point, Effects Of Turbulence Modeling on Computed Results

In this appendix of the thesis an investigation on the effects due to the adopted turbulence models was carried out on the baseline ECN Spray G1 operating condition. More in detail, two simulations were performed by respectively adopting the Pope correction ($C_{1\varepsilon} = 1.55$) standard $k - \varepsilon$ model and the RNG $k - \varepsilon$ approach with reference literature setup for its main parameters.

Calculations were carried out under equal setup between the two cases in terms of mesh characteristics, injector angle values and spray models setup, as it is reported in Tab.A.1. The computational grids were employed without AMR with a homogeneous cell size of 0.5 mm. A decoupled approach for the modeling of the atomization phase was chosen by means of the adoption of a dedicated $B_{1,atom}$ parameter for parcel stripping within the liquid core length. A KHRT model was adopted for the secondary breakup phase.

Fig.A.1(a)-A.1(b) respectively report the computed axial vapor penetration and centerline velocity profiles of the two simulated cases. Under a constant setup it was possible to address the influence on the spray evolution due to turbulence modeling. It can be observed that the behavior of the two cases is very similar up to the EOI temporal threshold (around 0.75 ms).

More in detail, no particular differences can be found during the whole atomization phase and for the early stages of the secondary breakup process. In fact, axial vapor penetration profiles look to be superimposed up to

Appendix A. ECN Spray G1 Operating Point, Effects Of Turbulence Modeling on Computed Results

Table A.1: *Adopted numerical spray setup*

Mesh	0.5 mm, no AMR
Atomization	Decoupled KH
Breakup	KHRT
B_0	0.61
$B_{1,atom}$	80
B_1	32
C_{RT}	0.35
Plume cone angle	25°
Drill angle	37°

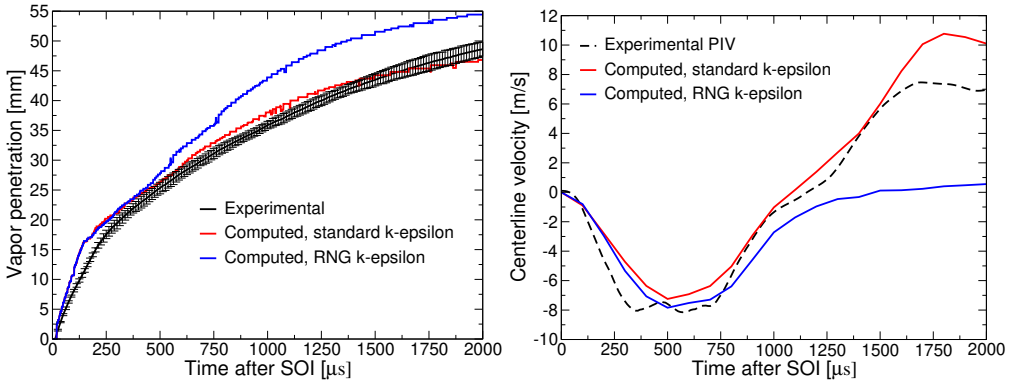

(a) Axial vapor penetration

(b) Centerline velocity

Figure A.1: *G1 simulations, effects of the adopted turbulence models on computed axial vapor penetration and centerline velocity*

0.5 ms and also the centerline velocity trends do not display significant discrepancies. Different behaviors begin to arise after the end of injection. The axial vapor penetration profile computed by the RNG $k-\varepsilon$ turbulence model considerably exceeds the experimental range of validity. At first, one may justify this phenomenon by claiming that the RNG mechanism promotes a higher liquid evaporation rate of the spray. This possible explanation is however immediately refuted by the fact that more residual liquid fuel is left in the computational domain at each time-step if compared with the results achieved by means of the standard $k-\varepsilon$ model with Pope round-jet correction. A further confirmation comes from the analysis of the centerline velocity which for the RNG case shows what can basically be considered as a lack of positive downward peak. After the EOI threshold the computed axial velocity magnitude stays in fact close to zero in value up to the end of the simulation. This fact means that at a position 15 mm downstream of the nozzle the gas phase appears to be almost quiescent with respect to the injector axis. Such an unphysical behavior appears as a direct consequence of a lack of entrainment and gas-liquid interaction.

It is thus clear that the overpredicted RNG axial vapor profile does not depend on a correct liquid evaporation process but it is strictly related to an expected inaccuracy of the computed spray morphology. This is confirmed by the analysis of the Lagrangian spray plumes coloured by the parcel velocity magnitude which is reported for both turbulence models in Fig.A.2(a)-A.2(b), Fig.A.3(a)-A.3(b) and Fig.A.4(a)-A.4(b) at time values respectively equal to 0.3 ms, 0.6 ms and 0.9 ms.

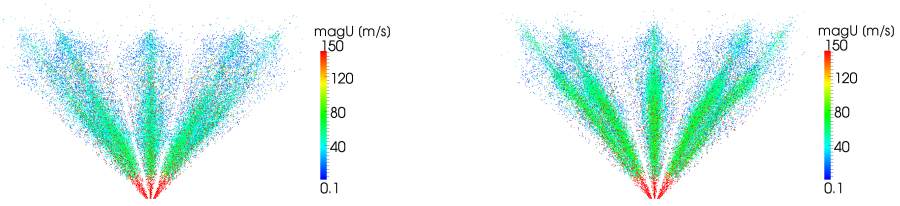

(a) Standard $k - \varepsilon$ with round-jet correction (b) RNG $k - \varepsilon$

Figure A.2: *Comparison of computed Lagrangian spray morphologies coloured by the liquid velocity magnitude, 0.3 ms*

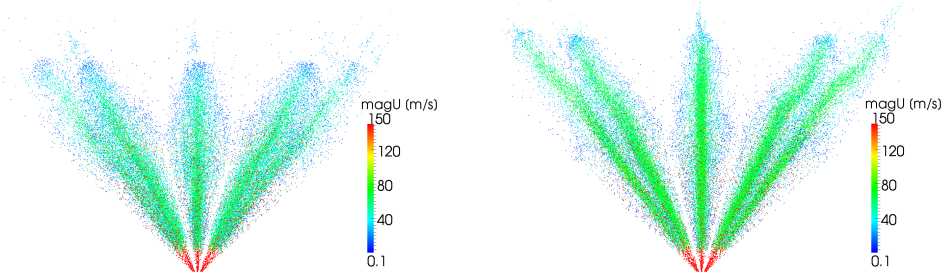

(a) Standard $k - \varepsilon$ with round-jet correction (b) RNG $k - \varepsilon$

Figure A.3: *Comparison of computed Lagrangian spray morphologies coloured by the liquid velocity magnitude, 0.6 ms*

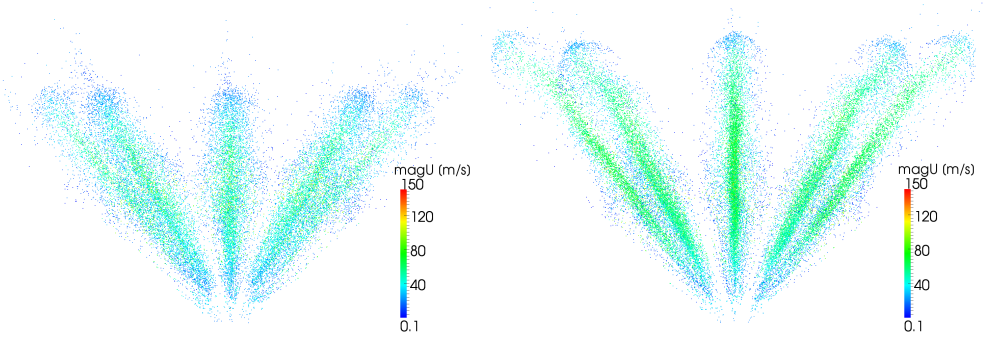

(a) Standard $k - \varepsilon$ with round-jet correction (b) RNG $k - \varepsilon$

Figure A.4: *Comparison of computed Lagrangian spray morphologies coloured by the liquid velocity magnitude, 0.9 ms*

Results show that, as expected, computed plume morphologies at 0.3 ms are very similar between the two cases. At 0.6 ms (close to the EOI threshold) the previously discussed physical differences start to be visible. The RNG

spray penetrates more because of a specific morphology which is characterized by less plume-to-plume interaction and less stripping, thus leading to a more compact liquid core with higher velocity magnitude for the primary parcels within. At 0.9 ms the same conclusions can be inferred with the discrepancies between the two cases which are further magnified.

Worse numerical predictions of spray morphology and entrainment can thus be considered as the main consequences of the adoption of the RNG $k - \varepsilon$ turbulence model. Within this context, it is difficult to suggest setup modifications which could help improve the achieved results. In fact, simulations were carried out with the most recent and advanced configurations in terms of mesh, atomization and secondary breakup management according to the investigations and validations proposed in this thesis. As a first step it could be suggested to work on the secondary breakup parameters of the RNG simulation. However it must be noticed that, for cases simulated with the standard $k - \varepsilon$ turbulence model, lack of entrainment and of liquid core evaporation are phenomena which usually influence the computed centerline velocity also before the EOI threshold. This is something which does not happen for the case with the RNG model whose effects on the velocity profile show abrupt differences before and after the end of injection. Within this context, future dedicated investigations may be required to improve the results achieved under these specific conditions.